

1

²A SEARCH FOR LONG-LIVED, CHARGED, SUPERSYMMETRIC PARTICLES
³USING IONIZATION WITH THE ATLAS DETECTOR

4

BRADLEY AXEN

5

September 2016 – Version 0.38

6



⁸ Bradley Axen: *A Search for Long-Lived, Charged, Supersymmetric Particles using*
⁹ *Ionization with the ATLAS Detector*, Subtitle, © September 2016

10

Usually a quotation.

11

Dedicated to.

₁₂ ABSTRACT

₁₃ How to write a good abstract:

₁₄ <https://plg.uwaterloo.ca/~migod/research/beck00PSLA.html>

₁₅ PUBLICATIONS

₁₆ Some ideas and figures have appeared previously in the following publications:

₁₇

₁₈ Put your publications from the thesis here. The packages `multibib` or `bibtopic`
₁₉ etc. can be used to handle multiple different bibliographies in your document.

²¹ ACKNOWLEDGEMENTS

²² Put your acknowledgements here.

²³

²⁴ And potentially a second round.

²⁵

26 CONTENTS

27	I	INTRODUCTION	1
28	1	INTRODUCTION	3
29	II	THEORETICAL CONTEXT	5
30	2	STANDARD MODEL	7
31	2.1	Particles	7
32	2.2	Interactions	8
33	2.3	Limitations	8
34	3	SUPERSYMMETRY	9
35	3.1	Motivation	9
36	3.2	Structure	9
37	3.3	Phenomenology	9
38	4	LONG-LIVED PARTICLES	11
39	4.1	Mechanisms	11
40	4.1.1	Examples in Supersymmetry	11
41	4.2	Phenomenology	11
42	4.2.1	Disimilarities to Prompt Decays	11
43	4.2.2	Characteristic Signatures	11
44	III	EXPERIMENTAL STRUCTURE AND RECONSTRUCTION	13
45	5	THE LARGE HADRON COLLIDER	15
46	5.1	Injection Chain	16
47	5.2	Design and Parameters	17
48	5.2.1	Layout	17
49	5.2.2	Magnets	18
50	5.3	Luminosity	19
51	6	THE ATLAS DETECTOR	21
52	6.1	Coordinate System	21
53	6.2	Magnetic Field	21
54	6.3	Inner Detector	21
55	6.3.1	Pixel Detector	21
56	6.3.2	Semiconductor Tracker	21
57	6.3.3	Transition Radiation Tracker	21
58	6.4	Calorimetry	21
59	6.4.1	Electromagnetic Calorimeters	21
60	6.4.2	Hadronic Calorimeters	21
61	6.4.3	Forward Calorimeters	21
62	6.5	Muon Spectrometer	21
63	6.6	Trigger	21
64	6.6.1	Trigger Scheme	21
65	6.6.2	Missing Transverse Energy Triggers	21

66	7	EVENT RECONSTRUCTION	23
67	7.1	Tracks and Vertices	23
68	7.1.1	Track Reconstruction	23
69	7.1.2	Vertex Reconstruction	23
70	7.2	Jets	23
71	7.2.1	Topological Clustering	23
72	7.2.2	Jet Energy Scale	23
73	7.2.3	Jet Energy Scale Uncertainties	23
74	7.2.4	Jet Energy Resolution	23
75	7.3	Electrons	23
76	7.3.1	Electron Identification	23
77	7.4	Muons	23
78	7.4.1	Muon Identification	23
79	7.5	Missing Transverse Energy	23
80	IV	CALORIMETER RESPONSE	25
81	8	RESPONSE MEASUREMENT WITH SINGLE HADRONS	27
82	8.1	Dataset and Simulation	28
83	8.1.1	Data Samples	28
84	8.1.2	Simulated Samples	28
85	8.1.3	Event Selection	28
86	8.2	Inclusive Hadron Response	29
87	8.2.1	E/p Distribution	29
88	8.2.2	Zero Fraction	30
89	8.2.3	Neutral Background Subtraction	31
90	8.2.4	Corrected Response	33
91	8.2.5	Additional Studies	35
92	8.3	Identified Particle Response	38
93	8.3.1	Decay Reconstruction	38
94	8.3.2	Identified Response	39
95	8.3.3	Additional Species in Simulation	41
96	8.4	Summary	42
97	9	JET ENERGY RESPONSE AND UNCERTAINTY	45
98	9.1	Motivation	45
99	9.2	Uncertainty Estimate	45
100	9.3	Summary	48
101	V	SEARCH FOR LONG-LIVED PARTICLES	51
102	10	LONG-LIVED PARTICLES IN ATLAS	53
103	10.1	Event Topology	53
104	10.1.1	Detector Interactions	54
105	10.1.2	Lifetime Dependence	55
106	10.2	Simulation	58
107	11	EVENT SELECTION	61
108	11.1	Trigger	62
109	11.2	Kinematics and Isolation	63
110	11.3	Particle Species Rejection	67

111	11.4 Ionization	70
112	11.4.1 Mass Estimation	71
113	11.5 Efficiency	72
114	12 BACKGROUND ESTIMATION	75
115	12.1 Background Sources	75
116	12.2 Prediction Method	76
117	12.3 Validation	77
118	12.3.1 Closure in Simulation	77
119	12.3.2 Validation Region in Data	78
120	13 SYSTEMATIC UNCERTAINTIES AND RESULTS	81
121	13.1 Systematic Uncertainties	81
122	13.1.1 Background Estimate	81
123	13.1.2 Signal Yield	82
124	13.2 Final Yields	88
125	13.3 Cross Sectional Limits	89
126	13.4 Mass Limits	91
127	13.5 Context for Long-Lived Searches	93
128	VI CONCLUSIONS	97
129	14 SUMMARY AND OUTLOOK	99
130	14.1 Summary	99
131	14.2 Outlook	99
132	VII APPENDIX	101
133	A INELASTIC CROSS SECTION	103
134	B EXPANDED R-HADRON YIELDS AND LIMITS	105
135	BIBLIOGRAPHY	111

136 LIST OF FIGURES

137	Figure 1	The particle content of the Standard Model (SM).	8
138	Figure 2	The four collision points and corresponding experiments of the Large Hadron Collider (LHC). The image includes the location of the nearby city of Geneva as well as the border of France and Switzerland.	16
139			
140			
141			
142	Figure 3	The accelerator complex that builds up to the full design energies at the LHC . The protons are passed in order to Linac 2, the PSB! , the PS! , the SPS! and then the LHC	16
143			
144			
145			
146	Figure 4	A schematic of the layout of the LHC , not to scale. The arched and straight sections are illustrated at the bottom of the schematic, and all four crossing sites are indicated with their respective experiments.	18
147			
148			
149			
150	Figure 5	A cross section of the the cryodipole magnets which bend the flight path of protons around the circumference of the LHC . The diagram includes both the superconducting coils which produce the magnetic field and the structural elements which keep the magnets precisely aligned.	19
151			
152			
153			
154			
155			
156	Figure 6	An illustration (a) of the E/p variable used throughout this paper. The red energy deposits come from the charged particle targeted for measurement, while the blue energy deposits are from nearby neutral particles and must be subtracted. The same diagram (b) for the neutral-background selection, described in Section 8.2.3.	30
157			
158			
159			
160			
161			
162	Figure 7	The E/p distribution and ratio of simulation to data for isolated tracks with (a) $ \eta < 0.6$ and $1.2 < p/\text{GeV} < 1.8$ and (b) $ \eta < 0.6$ and $2.2 < p/\text{GeV} < 2.8$	30
163			
164			
165	Figure 8	The fraction of tracks as a function (a, b) of momentum, (c, d) of interaction lengths with $E \leq 0$ for tracks with positive (on the left) and negative (on the right) charge.	32
166			
167			
168			
169	Figure 9	$\langle E/p \rangle_{\text{BG}}$ as a function of the track momentum for tracks with (a) $ \eta < 0.6$, (b) $0.6 < \eta < 1.1$, and as a function of the track pseudorapidity for tracks with (c) $1.2 < p/\text{GeV} < 1.8$, (d) $1.8 < p/\text{GeV} < 2.2$	33
170			
171			
172			
173	Figure 10	$\langle E/p \rangle_{\text{COR}}$ as a function of track momentum, for tracks with (a) $ \eta < 0.6$, (b) $0.6 < \eta < 1.1$, (c) $1.8 < \eta < 1.9$, and (d) $1.9 < \eta < 2.3$	34
174			
175			

176	Figure 11	$\langle E/p \rangle_{\text{COR}}$ calculated using LCW-calibrated topological clusters as a function of track momentum for tracks with (a) zero or more associated topological clusters or (b) one or more associated topological clusters.	35
177			
178			
179			
180	Figure 12	Comparison of the $\langle E/p \rangle_{\text{COR}}$ for tracks with (a) less than and (b) greater than 20 hits in the TRT.	36
181			
182	Figure 13	Comparison of the $\langle E/p \rangle_{\text{COR}}$ for (a) positive and (b) negative tracks as a function of track momentum for tracks with $ \eta < 0.6$	36
183			
184			
185	Figure 14	Comparison of the E/p distributions for (a) positive and (b) negative tracks with $0.8 < p/\text{GeV} < 1.2$ and $ \eta < 0.6$, in simulation with the FTFP_BERT and QGSP_BERT physics lists.	37
186			
187			
188			
189	Figure 15	Comparison of the response of the hadronic calorimeter as a function of track momentum (a) at the EM-scale and (b) after the LCW calibration.	37
190			
191			
192	Figure 16	Comparison of the response of the EM calorimeter as a function of track momentum (a) at the EM-scale and (b) with the LCW calibration.	38
193			
194			
195	Figure 17	The reconstructed mass peaks of (a) K_S^0 , (b) Λ , and (c) $\bar{\Lambda}$ candidates.	39
196			
197	Figure 18	The E/p distribution for isolated (a) π^+ , (b) π^- , (c) proton, and (d) anti-proton tracks.	40
198			
199	Figure 19	The fraction of tracks with $E \leq 0$ for identified (a) π^+ and π^- , and (b) proton and anti-proton tracks	40
200			
201	Figure 20	The difference in $\langle E/p \rangle$ between (a) π^+ and π^- (b) p and π^+ , and (c) \bar{p} and π^-	41
202			
203	Figure 21	$\langle E/p \rangle_{\text{COR}}$ as a function of track momentum for (a) π^+ tracks and (b) π^- tracks.	42
204			
205	Figure 22	The ratio of the calorimeter response to single particles of various species to the calorimeter response to π^+ with the physics list FTFP_BERT.	42
206			
207			
208	Figure 23	The spectra of true particles inside anti- k_t , $R = 0.4$ jets with (a) $90 < p_T/\text{GeV} < 100$, (b) $400 < p_T/\text{GeV} < 500$, and (c) $1800 < p_T/\text{GeV} < 2300$	46
209			
210			
211	Figure 24	The jet energy scale (JES) uncertainty contributions, as well as the total JES uncertainty, as a function of jet p_T for (a) $ \eta < 0.6$ and (b) $0.6 < \eta < 1.1$	48
212			
213			
214	Figure 25	The JES correlations as a function of jet p_T and $ \eta $ for jets in the central region of the detector.	49
215			

216	Figure 26	A schematic diagram of an R-Hadron event with a life-time around 0.01 ns. The diagram includes one charged R-Hadron (solid blue), one neutral R-Hadron (dashed blue), Lightest Supersymmetric Particles (LSPs) (dashed green) and charged hadrons (solid orange). The pixel detector, calorimeters, and muon system are illustrated but not to scale.	55
223	Figure 27	A schematic diagram of an R-Hadron event with a life-time around 4 ns. The diagram includes one charged R-Hadron (solid blue), one neutral R-Hadron (dashed blue), LSPs (dashed green) and a charged hadron (solid orange). The pixel detector, calorimeters, and muon system are illustrated but not to scale.	56
229	Figure 28	A schematic diagram of an R-Hadron event with a life-time around 5 ns. The diagram includes one charged R-Hadron (solid blue), one neutral R-Hadron (dashed blue), LSPs (dashed green) and charged hadrons (solid orange). The pixel detector, calorimeters, and muon system are illustrated but not to scale.	57
235	Figure 29	A schematic diagram of an R-Hadron event with a life-time around 20 ns. The diagram includes one charged R-Hadron (solid blue), one neutral R-Hadron (dashed blue), LSPs (dashed green) and charged hadrons (solid orange). The pixel detector, calorimeters, and muon system are illustrated but not to scale.	57
241	Figure 30	A schematic diagram of an R-Hadron event with a life-time around 20 ns. The diagram includes one charged R-Hadron (solid blue) and one neutral R-Hadron (dashed blue). The pixel detector, calorimeters, and muon system are illustrated but not to scale.	58
246	Figure 31	The distribution of (a) E_T^{miss} and (b) Calorimeter E_T^{miss} for simulated signal events before the trigger requirement.	62
249	Figure 32	The distribution of E_T^{miss} for data and simulated signal events, after the trigger requirement.	64
251	Figure 33	The trigger efficiency for the HLT_xe70 trigger requirement as a function of (a) E_T^{miss} and (b) Calorimeter E_T^{miss} for simulated signal events.	65
254	Figure 34	The dependence of dE/dx on N_{split} in data after basic track hit requirements have been applied.	66
256	Figure 35	The distribution of dE/dx with various selections applied in data and simulated signal events.	66
258	Figure 36	The distribution of track momentum for data and simulated signal events, after previous selection requirements have been applied.	67

261	Figure 37	The distribution of M_T for data and simulated signal events, after previous selection requirements have been applied.	68
262			
263			
264	Figure 38	The distribution of summed tracked momentum within a cone of $\Delta R < 0.25$ around the candidate track for data and simulated signal events, after previous selection requirements have been applied.	69
265			
266			
267			
268	Figure 39	The normalized, two-dimensional distribution of E/p and f_{EM} for simulated (a) $Z \rightarrow ee$, (b) $Z \rightarrow \tau\tau$, (c) 1200 GeV Stable R-Hadron events, and (d) 1200 GeV, 10 ns R-Hadron events.	70
269			
270			
271			
272	Figure 40	Two-dimensional distribution of dE/dx versus charge signed momentum (qp) for minimum-bias tracks. The fitted distributions of the most probable values for pions, kaons and protons are superimposed.	71
273			
274			
275			
276	Figure 41	The distribution of mass estimated using dE/dx for simulated stable R-Hadrons with masses between 1000 and 1600 GeV.	72
277			
278			
279	Figure 42	The acceptance \times efficiency as a function of R-Hadron (a) mass and (b) lifetime. (a) shows all of the combinations of mass and lifetime considered in this search, and (b) highlights the lifetime dependence for 1000 GeV and 1600 GeV R-Hadrons.	74
280			
281			
282			
283			
284	Figure 43	The distribution of (a) dE/dx and (b) momentum for tracks in data and simulated signal after requiring the event level selection and the track selection on p_T , hits, and N_{split} . Each sub-figure shows the normalized distributions for tracks classified as hadrons, electrons, and muons in data and R-Hadrons in the simulated signal.	76
285			
286			
287			
288			
289			
290			
291	Figure 44	The distribution of $M_{dE/dx}$ (a) before and (b) after the ionization requirement for tracks in simulated W boson decays and for the randomly generated background estimate.	78
292			
293			
294			
295	Figure 45	The distribution of $M_{dE/dx}$ (a) before and (b) after the ionization requirement for tracks in the validation region and for the randomly generated background estimate.	79
296			
297			
298			
299	Figure 46	The trigger efficiency for the HLT_xe70 trigger requirement as a function of Calorimeter E_T^{miss} for simulated data events with a W boson selection. Simulated signal events and simulated W boson events are also included.	84
300			
301			
302			
303			
304	Figure 47	The efficiency of the muon veto for R-hadrons of two different masses, as a function of $\frac{1}{\beta}$ for simulated R-Hadron tracks.	86
305			
306			

307	Figure 48	The average reconstructed MDT β distribution for $Z \rightarrow \mu\mu$ events in which one of the muons is reconstructed as a slow muon, for both data and simulation. A gaussian fit is superimposed.	87
308			
309			
310			
311	Figure 49	The observed mass distribution of events in data and the generated background distribution in (a) the stable and (b) the metastable signal region. A few example simulated signal distributions are superimposed.	88
312			
313			
314			
315	Figure 50	The observed and expected cross section limits as a function of mass for the stable simulated signal. The predicted cross section values for the corresponding signals are included.	91
316			
317			
318			
319	Figure 51	The observed and expected cross section limits as a function of mass for each generated lifetime. The predicted cross section values for the corresponding signals are included.	92
320			
321			
322			
323	Figure 52	The excluded range of masses as a function of gluino lifetime. The expected lower limit (LL), with its experimental $\pm 1\sigma$ band, is given with respect to the nominal theoretical cross-section. The observed 95% LL obtained at $\sqrt{s} = 8$ TeV [61] is also shown for comparison.	94
324			
325			
326			
327			
328	Figure 53	The constraints on the gluino mass as a function of lifetime for a split-supersymmetry model with the gluino R-Hadrons decaying into a gluon or light quarks and a neutralino with mass of 100 GeV. The solid lines indicate the observed limits, while the dashed lines indicate the expected limits. The area below the curves is excluded. The dots represent results for which the particle is assumed to be prompt or stable.	95
329			
330			
331			
332			
333			
334			
335			

336 LIST OF TABLES

337	Table 1	The dominant sources of corrections and systematic uncertainties in the JES estimation technique, including typical values for the correcting shift (Δ) and the associated uncertainty (σ).	47
338			
339			
340			
341	Table 2	The expected number of events at each level of the selection for metastable 1600 GeV, 10 ns R-Hadrons, along with the number of events observed in data, for 3.2 fb^{-1} . The simulated yields are shown with statistical uncertainties only. The total efficiency \times acceptance is also shown for the signal.	73
342			
343			
344			
345			
346			
347	Table 3	A summary of the sources of systematic uncertainty for the data-driven background in the signal region. If the uncertainty depends on the mass, the maximum values are reported.	81
348			
349			
350			
351	Table 4	A summary of the sources of systematic uncertainty for the simulated signal yield. The uncertainty depends on the mass and lifetime, and the maximum negative and positive values are reported in the table.	83
352			
353			
354			
355	Table 5	Example of the contributing systematic variations to the total systematic for the E_T^{miss} Scale, as measured in a 1200 GeV, Stable R-Hadron signal sample.	85
356			
357			
358	Table 6	The estimated number of background events and the number of observed events in data for the specified selection regions prior to the requirement on mass. The background estimates show statistical and systematic uncertainties.	88
359			
360			
361			
362			
363	Table 7	The left and right extremum of the mass window for each generated mass point with a 10 ns lifetime.	89
364			
365	Table 8	The left and right extremum of the mass window used for each generated stable mass point.	89
366			
367	Table 9	The expected number of signal events, the expected number of background events, and the observed number of events in data with their respective statistical errors within the respective mass window for each generated stable mass point	90
368			
369			
370			
371			
372	Table 10	The expected number of signal events, the expected number of background events, and the observed number of events in data with their respective statistical errors within the respective mass window for each generated mass point with a lifetime of 10 ns.	90
373			
374			
375			
376			

377	Table 11	The observed and expected 95% CL lower limit on mass for gluino R-Hadrons for each considered lifetime.	93
378			
379	Table 12	The left and right extremum of the mass window for each generated mass point with a 50 ns lifetime.	105
380			
381	Table 13	The left and right extremum of the mass window for each generated mass point with a 30 ns lifetime.	105
382			
383	Table 14	The left and right extremum of the mass window for each generated mass point with a 10 ns lifetime.	106
384			
385	Table 15	The left and right extremum of the mass window used for each generated mass point with a lifetime of 3 ns.	106
386			
387	Table 16	The left and right extremum of the mass window used for each mass point with a lifetime of 1 ns.	106
388			
389	Table 17	The left and right extremum of the mass window for each generated mass point with a lifetime of 0.4 ns.	107
390			
391	Table 18	The left and right extremum of the mass window used for each generated stable mass point.	107
392			
393	Table 19	The expected number of signal events, the expected number of background events, and the observed number of events in data with their respective statistical errors within the respective mass window for each generated mass point with a lifetime of 50 ns.	107
394			
395			
396			
397			
398	Table 20	The expected number of signal events, the expected number of background events, and the observed number of events in data with their respective statistical errors within the respective mass window for each generated mass point with a lifetime of 30 ns.	108
399			
400			
401			
402			
403	Table 21	The expected number of signal events, the expected number of background events, and the observed number of events in data with their respective statistical errors within the respective mass window for each generated mass point with a lifetime of 10 ns.	108
404			
405			
406			
407			
408	Table 22	The expected number of signal events, the expected number of background events, and the observed number of events in data with their respective statistical errors within the respective mass window for each generated mass point with a lifetime of 3 ns.	109
409			
410			
411			
412			
413	Table 23	The expected number of signal events, the expected number of background events, and the observed number of events in data with their respective statistical errors within the respective mass window for each generated mass point with a lifetime of 1 ns.	109
414			
415			
416			
417			
418	Table 24	The expected number of signal events, the expected number of background events, and the observed number of events in data with their respective statistical errors within the respective mass window for each generated mass point with a lifetime of p4 ns.	110
419			
420			
421			
422			

423	Table 25	The expected number of signal events, the expected number of background events, and the observed num- ber of events in data with their respective statistical er- rors within the respective mass window for each gen- erated stable mass point	110
424			
425			
426			
427			

428 LISTINGS

⁴²⁹ ACRONYMS

- ⁴³⁰ SM Standard Model
⁴³¹ SUSY Supersymmetry
⁴³² LSP Lightest Supersymmetric Particle
⁴³³ LHC Large Hadron Collider
⁴³⁴ ATLAS A Toroidal LHC ApparatuS
⁴³⁵ LEP the Large Electron Positron collider
⁴³⁶ ToT time over threshold
⁴³⁷ LCW local cluster weighted
⁴³⁸ MIP minimally ionizing particle
⁴³⁹ EPJC European Physical Journal C
⁴⁴⁰ JES jet energy scale
⁴⁴¹ LLP Long-Lived Particle
⁴⁴² CR Control Region
⁴⁴³ NLO next-to-leading order
⁴⁴⁴ NLL next-to-leading logarithmic
⁴⁴⁵ PDF parton distribution function
⁴⁴⁶ ISR initial state radiation
⁴⁴⁷ RMS root mean square
⁴⁴⁸ IBL Insertible B-Layer
⁴⁴⁹ CP Combined Performance
⁴⁵⁰ MDT Monitored Drift Tube

451

PART I

452

INTRODUCTION

453

You can put some informational part preamble text here.

1

454

455 INTRODUCTION

456

PART II

457

THEORETICAL CONTEXT

458

You can put some informational part preamble text here.

2

459

460 STANDARD MODEL

461 The SM of particle physics seeks to explain the symmetries and interactions of
462 all currently discovered fundamental particles. It has been tested by several genera-
463 tions of experiments and has been remarkably successful, no significant de-
464 viations have been found. The SM provides predictions in particle physics for
465 interactions up to the Planck scale (10^{15} - 10^{19} GeV).

466 The theory itself is a quantum field theory grown from an underlying $SU(3) \times$
467 $SU(2) \times U(1)$ that requires the particle content and quantum numbers consist-
468 ent with experimental observations (see Section 2.1). Each postulated symme-
469 try is accompanied by an interaction between particles through gauge invari-
470 ance. These interactions are referred to as the Strong, Weak, and Electromag-
471 netic forces, which are discussed in Section 2.2.

472 Although this model has been very predictive, the theory is incomplete; for
473 example, it is not able to describe gravity or astronomically observed dark matter.
474 These limitations are discussed in more detail in Section 2.3.

475 21 PARTICLES

476 The most familiar matter in the universe is made up of protons, neutrons, and
477 electrons. Protons and neutrons are composite particles, however, and are made
478 up in turn by particles called quarks. Quarks carry both electric charge and color
479 charge, and are bound in color-neutral combinations called baryons. The elec-
480 tron is an example of a lepton, and carries only electric charge. Another type
481 of particle, the neutrino, does not form atomic structures in the same way that
482 quarks and leptons do because it carries no color or electric charge. Collectively,
483 these types of particles are known as fermions, the group of particles with half-
484 integer spin.

485 There are three generations of fermions, although familiar matter is formed
486 predominantly by the first generation. The generations are identical except for
487 their masses, which increase in each generation by convention. In addition, each
488 of these particles is accompanied by an antiparticle, with opposite-sign quantum
489 numbers but the same mass.

490 The fermions comprise what is typically considered matter, but there are
491 additional particles that are mediators of interactions between those fermions.
492 These mediators are known as the gauge bosons, gauge in that their existence
493 is required by gauge invariance (discussed further in Section 2.2) and bosons in
494 that they have integer spin. The boson which mediates the electromagnetic force
495 is the photon, the first boson to be discovered; it has no electric charge, no mass,
496 and a spin of 1. There are three spin-1 mediators of the weak force, the two
497 W bosons and the Z boson. The W bosons have electric charge of ± 1 and a
498 mass of 80.385 ± 0.015 GeV, while the Z boson is neutral and has a mass of

499 91.1876 \pm 0.0021 GeV. The strong force is mediated by eight particles called
500 gluons, which are massless and electrically neutral but do carry color charge.

501 The final particle present in the SM is the Higgs boson, which was recently
502 observed for the first time by experiments at CERN in 2012. It is electrically
503 neutral, has a mass of 125.7 \pm 0.4 GeV, and is the only spin-0 particle yet to be
504 observed. The Higgs boson is the gauge boson associated with the mechanism
505 that gives a mass to the W and Z bosons.

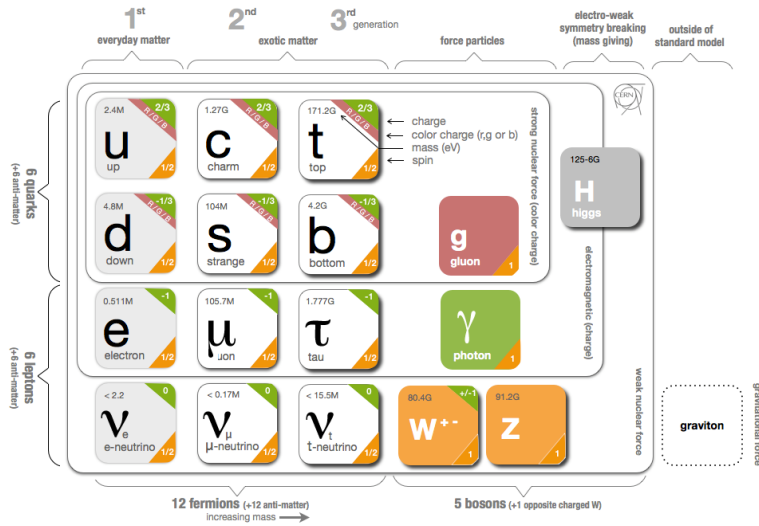


Figure 1: The particle content of the SM.

506 Together these particles form the entire content of the SM, and are summa-
507 rized in Figure 1. These are the particles that constitute the observable universe
508 and all the so-far-observed interactions within it.

509 2.2 INTERACTIONS

510 The interactions predicted and described by the SM are fundamentally tied to the
511 particles within it, both in that they describe the way those particles can influence
512 each other and also in that the existence of the interactions requires the existence
513 of some particles (the gauge bosons).

514 2.3 LIMITATIONS

3

s15

s16 SUPERSYMMETRY

s17 3.1 MOTIVATION

s18 3.2 STRUCTURE

s19 3.3 PHENOMENOLOGY

4

520

521 LONG-LIVED PARTICLES

522 4.1 MECHANISMS

523 4.1.1 EXAMPLES IN SUPERSYMMETRY

524 4.2 PHENOMENOLOGY

525 4.2.1 DISIMILARITIES TO PROMPT DECAYS

526 4.2.2 CHARACTERISTIC SIGNATURES

527

PART III

528

EXPERIMENTAL STRUCTURE AND RECONSTRUCTION

529

You can put some informational part preamble text here.

531 THE LARGE HADRON COLLIDER

532 The LHC, a two-ring superconducting hadron accelerator, provides high energy
533 proton-proton collisions for several large experiments at CERN! (CERN!) in Geneva,
534 Switzerland [1, 2]. It is the largest, highest-luminosity, and highest-energy pro-
535 ton collider ever built, and was constructed by a collaboration of more than
536 10,000 scientists from more than 100 countries that contribute to CERN!. The
537 original design of the LHC focused on providing collision energies of up to 14
538 TeV and generating enough collisions to reveal physics beyond the SM predicted
539 to exist at higher energy scales.

540 The LHC was installed in an existing 27 km tunnel at CERN! which was origi-
541 nally designed to house the Large Electron Positron collider (LEP). This allows
542 the collider to use existing accelerators at the same complex to provide the ini-
543 tial acceleration of protons up to 450 GeV before injecting into LHC to accel-
544 erate up to design energies. The injected hadrons can be accelerated up to as
545 much as 14 TeV while being focused into two beams travelling in opposite di-
546 rections. During this process the protons can circulate around the tunnel mil-
547 lions of times, while the beams are intermittently crossed at the four locations of
548 the experiments to provide collisions. These collision points correspond to the
549 four major LHC experiments: A Toroidal LHC ApparatuS (ATLAS), CMS! (CMS!),
550 LHCb! (LHCb!), and ALICE! (ALICE!), and Figure 2 shows the layout of the ex-
551 periments both on the surface and below. ATLAS and CMS! are both general pur-
552 pose, high-luminosity detectors which search for a wide range of new types of
553 physics [3, 4]. LHCb! studies the interactions of b-hadrons to explore the asym-
554 metry between matter and antimatter [5]. ALICE! focuses on the collisions of
555 lead ions, which the LHC also provides, in order to study the properties of quark-
556 gluon plasma [6].

557 During the first five years of operation, after the LHC turned on in 2010, the
558 LHC has provided four major data collecting periods. In 2010 the LHC increased
559 the energy from 900 GeV to 2.76 TeV and then subsequently to 7 TeV, with
560 a peak luminosity of $2 \times 10^{32} \text{ cm}^{-2}\text{s}^{-1}$, with a total delivered luminosity of 50
561 pb $^{-1}$ for the ATLAS detector. The next run, during 2011, continued the operation
562 at 7 TeV and provided an additional 5 fb $^{-1}$ with a peak luminosity of 4×10^{33}
563 cm $^{-2}\text{s}^{-1}$. The energy was then increased to 8 TeV for the data collection during
564 2012, which provided 23 fb $^{-1}$ with a peak luminosity of $7.7 \times 10^{33} \text{ cm}^{-2}\text{s}^{-1}$. Af-
565 ter the first long shutdown for 2013 and 2014, the LHC resumed operation and
566 increased the energy to 13 TeV in 2015, where it delivered 4.2 fb $^{-1}$ with a peak
567 luminosity of $5.5 \times 10^{33} \text{ cm}^{-2}\text{s}^{-1}$.

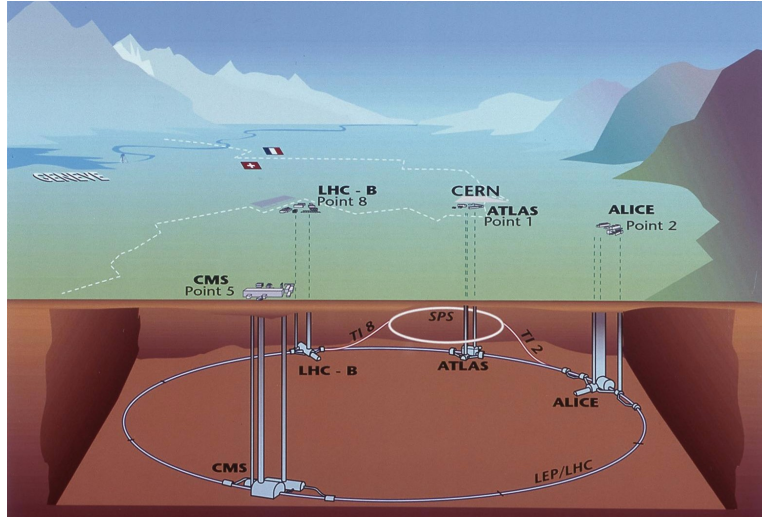


Figure 2: The four collision points and corresponding experiments of the LHC. The image includes the location of the nearby city of Geneva as well as the border of France and Switzerland.

568 5.1 INJECTION CHAIN

569 The LHC takes advantage of the presence of previously built accelerators at CERN!
 570 to work up to the target energy in consecutive stages. The series of accelerators
 571 that feed into the LHC are known collectively as the injection chain, and together
 572 with the LHC form the accelerator complex. The full complex is illustrated in
 573 Figure 3, which details the complex series required to reach collisions of 13 or
 574 14 TeV.

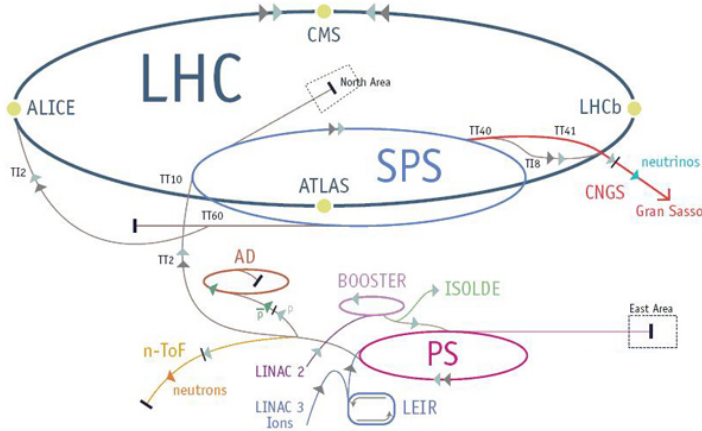


Figure 3: The accelerator complex that builds up to the full design energies at the LHC.
 The protons are passed in order to Linac 2, the PS!, the PS!, the SPS! and then
 the LHC.

575 Protons at the LHC begin as hydrogen atoms in the Linac 2, a linear accelerator
 576 which replaced Linac 1 as the primary proton accelerator at CERN in 1978. In
 577 Linac 2, the hydrogen atoms are stripped of their electrons by a strong magnetic

578 field, and the resulting protons are accelerated up to 50 MeV by cylindrical con-
 579 ductors charged by radiofrequency cavities. The protons are then transferred to
 580 the **PSB!** (**PSB!**), which uses a stack of four synchrotron rings to accelerate the pro-
 581 tons up to 1.4 GeV. Then the protons are injected into the **PS!** (**PS!**) which again
 582 uses synchrotron rings to bring the energy up to 25 GeV. The intermediate step
 583 between Linac 2 and the **PS!** is not directly necessary, as the **PS!** can accelerate pro-
 584 tons starting from as low as 50 MeV. The inclusion of the **PSB!** allows the **PS!** to
 585 accept a higher intensity of injection and so increases the deliverable luminosity
 586 in the **LHC**. The penultimate stage of acceleration is provided by the **SPS!** (**SPS!**),
 587 a large synchrotron with a 7 km circumference that was commisioned at CERN
 588 in 1976. During this step the protons increase in energy to 450 GeV, after which
 589 they can be directly injected into the **LHC**.

590 The final step is the **LHC** itself, which receives protons from the **SPS!** into two
 591 separate beam pipes which circulate in opposite directions. The filling process at
 592 this steps takes approximately 4 minutes, and the subsequent acceleration to the
 593 final energy (6.5 TeV during 2015 and up to 7 TeV by design) takes appriximately
 594 half an hour. At this point the protons circulate around the circumference tens
 595 of thousands of times a second and continue for up to two hours.

596 5.2 DESIGN AND PARAMETERS

597 5.2.1 LAYOUT

598 Many of the aspects of the **LHC** design are driven by the use of the existing **LEP**
 599 tunnel. This tunnel slopes gradually, with a 1.4% decline, with 90% of its length
 600 built into molasse rock which is particularly well suited to the application. The
 601 circumference is composed of eight 2987 meter arcs and eight 528 meter straight
 602 sections which connect them; this configuration is illustrated in Figure 4. The
 603 tunnel diameter is 3.7 m throughout its length.

604 The design energy is directly limited by the size of this tunnel, with its radius
 605 of curvature of 2804 m. A significant magnetic field is required to curve the
 606 protons around that radius of curvature; the relationship is given by:

$$p \approx 0.3BR$$

607 where p is the momentum of the particle in GeV, B is the magnetic field in Tesla,
 608 and R is the radius of curvature in meters. From the target design energy of
 609 14 TeV, or 7 TeV of momentum for protons in each beam, the required mag-
 610 netic field is 8.33 Tesla. This is too large a field strength to be practical with
 611 iron electromagnets, because of the enormous power required and the resulting
 612 requirements for cooling. Because of these constraints, the **LHC** uses supercon-
 613 ducting magnets which can maintain that field strength with significantly less
 614 power comsumption.

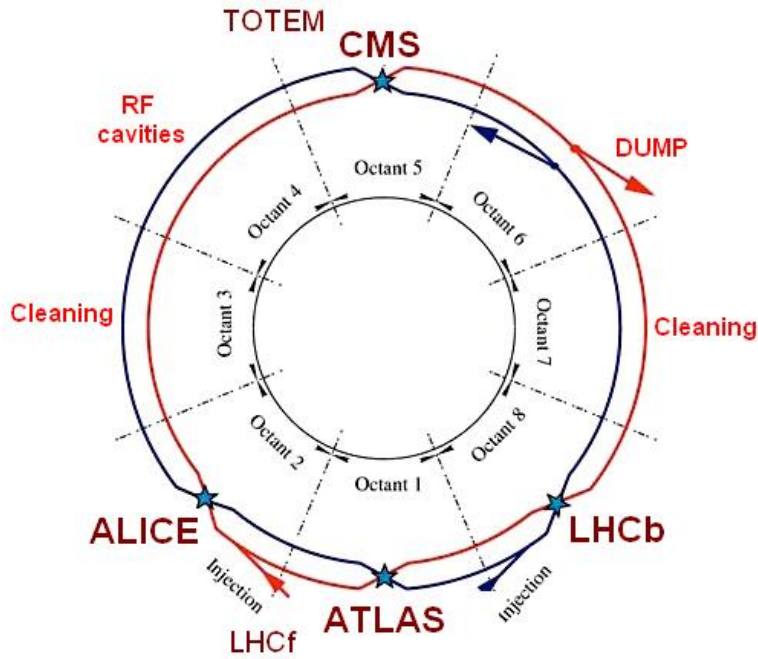


Figure 4: A schematic of the layout of the [LHC](#), not to scale. The arched and straight sections are illustrated at the bottom of the schematic, and all four crossing sites are indicated with their respective experiments.

615 5.2.2 MAGNETS

616 Specifically the magnets chosen were Niobium and Titanium (NbTi) which allow
 617 for field strengths as high as 10 Tesla when cooled down to 1.9 K. Reach 1.9 K
 618 for all of the magnetis requires superfluid helium and a large cryogenic system
 619 along the entire length of the tunnel. During normal operation, the [LHC](#) uses 120
 620 tonnes of helium within the magnetics, and the entire system is cooled by eight
 621 cryogenic helium refrigerators. The temperature increase that occurs during
 622 transit from the refrigerator along the beam necessitates that the refrigerators
 623 cool the helium down to 1.8 K.

624 In all there are approximately 8000 superconducting magnets distributed around
 625 the [LHC](#). The 1232 bending magnets, which keep the protons curving along the
 626 length of the beam, are twin bore cryodipoles, which allow both proton beams to
 627 be accomodated by one magnet and all of the associated cooling structure. Fig-
 628 ure 5 shows the cross section of the design for these dipoles. The magnets are
 629 very large, 16.5 m long with a diameter of 0.57 meters and a total weight of 28
 630 tonnes. They are slightly curved, with an angle of 5.1 mrad, in order to carefully
 631 match the beam path. The twin bore accomodates both magnets inside the two
 632 5 cm diameter holes which are surrounded by the superconducting coils. The
 633 coils require 12 kA of current in order to produce the required magnetic field.
 634 These coils are comprised of NbTi cable wound in two layers; the wire in the
 635 inner layer has a diameter of 1.065 mm while the wire in the outer layer has a
 636 diameter of 0.825 mm.

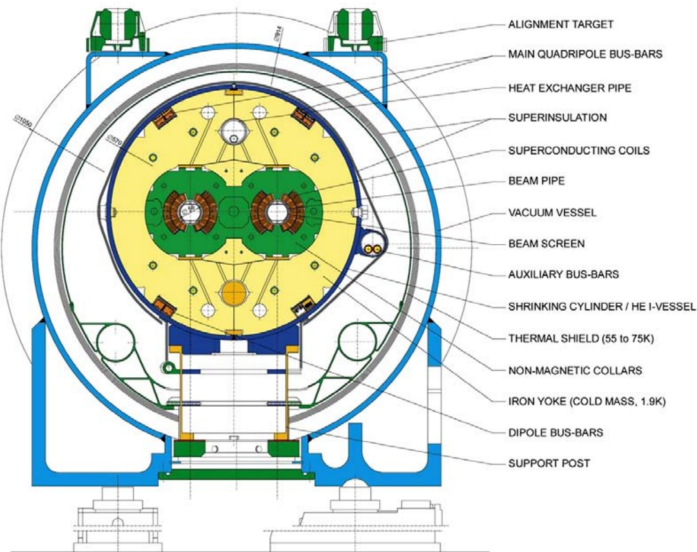


Figure 5: A cross section of the the cryodipole magnets which bend the flight path of protons around the circumference of the LHC. The diagram includes both the superconducting coils which produce the magnetic field and the structural elements which keep the magnets precisely aligned.

637 The large current in the wires, along with the magnetic field produced, result
 638 in forces on the magnets which would tend to push them apart with over 10,000
 639 Newtons per meter. Constraining the magnets requires a significant amount of
 640 structure including non-magnetic stainless steel collars. Both the presence of
 641 these electromagnetic forces and the varying thermal contraction coefficient of
 642 the pieces of the magnet produce significant forces on the cold mass structure.
 643 The cold mass is carefully engineered so that these stresses do not significantly
 644 alter the magnetic field shape, which must be maintained between magnets to a
 645 precision of approximately 10^{-4} for successful operation.

646 The remaining 6800 magnets are a variety of quadrupole, sextupole, octopole,
 647 and single bore dipole magnets. These are used to damp oscillations, correct
 648 beam trajectories, focus the beams during circulation, and to squeeze the beams
 649 before collisions.

650 5.3 LUMINOSITY

6

651

652 THE ATLAS DETECTOR

653 6.1 COORDINATE SYSTEM

654 6.2 MAGNETIC FIELD

655 6.3 INNER DETECTOR

656 6.3.1 PIXEL DETECTOR

657 6.3.2 SEMICONDUCTOR TRACKER

658 6.3.3 TRANSITION RADIATION TRACKER

659 6.4 CALORIMETRY

660 6.4.1 ELECTROMAGNETIC CALORIMETERS

661 6.4.2 HADRONIC CALORIMETERS

662 6.4.3 FORWARD CALORIMETERS

663 6.5 MUON SPECTROMETER

664 6.6 TRIGGER

665 6.6.1 TRIGGER SCHEME

666 6.6.2 MISSING TRANSVERSE ENERGY TRIGGERS

7

667

668 EVENT RECONSTRUCTION

669 The ATLAS experiment combines measurements in the subdetectors to form a
670 cohesive picture of each physics event.

671 7.1 TRACKS AND VERTICES

672 7.1.1 TRACK RECONSTRUCTION

673 7.1.1.1 NEURAL NETWORK

674 7.1.1.2 PIXEL DE/DX

675 7.1.2 VERTEX RECONSTRUCTION

676 7.2 JETS

677 7.2.1 TOPOLOGICAL CLUSTERING

678 7.2.2 JET ENERGY SCALE

679 7.2.3 JET ENERGY SCALE UNCERTAINTIES

680 7.2.4 JET ENERGY RESOLUTION

681 7.3 ELECTRONS

682 7.3.1 ELECTRON IDENTIFICATION

683 7.4 MUONS

684 7.4.1 MUON IDENTIFICATION

685 7.5 MISSING TRANSVERSE ENERGY

686

PART IV

687

CALORIMETER RESPONSE

688

You can put some informational part preamble text here.

8

689

690 RESPONSE MEASUREMENT WITH SINGLE HADRONS

691 As discussed in Section 7.2, colored particles produced in collisions hadronize
692 into jets of multiple hadrons. One approach to understanding jet energy mea-
693 surements in the ATLAS calorimeters is to evaluate the calorimeter response to
694 those individual hadrons; measurements of individual hadrons can be used to
695 build up an understanding of the jets that they form. The redundancy of the
696 momentum provided by the tracking system and the energy provided by the
697 calorimeter provides an opportunity to study calorimeter response using real
698 collisions, as described further in Section 8.2.

699 Calorimeter response includes a number of physical effects that can be ex-
700 tracted to provide insight into many aspects of jet modeling. First, many charged
701 hadrons interact with the material of the detector prior to reaching the calorime-
702 ters and thus do not deposit any energy. Comparing this effect in data and simu-
703 lation is a powerful tool in validating the interactions of particles with the mate-
704 rial of the detector and the model of the detector geometry in simulation, see Sec-
705 tion 8.2.2. The particles which do reach the calorimeter deposit their energy into
706 several adjacent cells, which are then clustered together. The energy of the clus-
707 ter is then the total energy deposited by that particle. Comparing the response of
708 hadrons in data to that of simulated hadrons provides a direct evaluation of the
709 showering of hadronic particles and the energy deposited by particles in matter
710 (Section 8.2.4).

711 The above studies all use an inclusive selection of charged particles, which are
712 comprised predominantly of pions, kaons, and (anti)protons. It is also possible to
713 measure the response to various identified particle types separately to evaluate
714 the simulated interactions of each particle, particularly at low energies where
715 differences between species are very relevant. Pions and (anti)protons can be
716 identified through decays of long-lived particles, in particular Λ , $\bar{\Lambda}$, and K_S^0 , and
717 then used to measure response as described above. This is discussed in detail in
718 Section 8.3.

719 The results in this chapter use data collected at 7 and 8 TeV collected in 2010
720 and 2012, respectively. Both are included as the calorimeter was repaired and
721 recalibrated between those two data-taking periods. Both sets of data are com-
722 pared to an updated simulation that includes new physics models provided by
723 Geant4 [7] and improvements in the detector description [8, 9]. The present
724 results are published in European Physical Journal C (EPJC) [10] and can be com-
725 pared to a similar measurement performed in 2009 and 2010 [11], which used
726 the previous version of the simulation framework [12].

727 8.1 DATASET AND SIMULATION

728 8.1.1 DATA SAMPLES

729 The two datasets used in this chapter are taken from dedicated low-pileup runs
 730 where the fraction of events with multiple interactions was negligible. These
 731 datasets are used rather than those containing full-pileup events to facilitate mea-
 732 surement of isolated hadrons. The 2012 dataset at $\sqrt{s} = 8$ TeV contains 8 mil-
 733 lion events and corresponds to an integrated luminosity of 0.1 nb^{-1} . The 2010
 734 dataset at $\sqrt{s} = 7$ TeV contains 3 million events and corresponds to an inte-
 735 grated luminosity of 3.2 nb^{-1} . The latter dataset was also used for the 2010 re-
 736 sults [11], but it has since been reanalyzed with an updated reconstruction in-
 737 cluding the final, best understanding of the detector description for the material
 738 and alignment from Run 1.

739 8.1.2 SIMULATED SAMPLES

740 The two datasets above are compared to simulated single-, double-, and non-
 741 diffractive events generated with Pythia8 [13] using the A2 configuration of
 742 hadronization [14] and the MSTW 2008 parton-distribution function set [15,
 743 16]. The admixture of the single-, double-, and non-diffractive events uses the
 744 default relative contributions from Pythia8. The conditions and energies for
 745 the two simulations are chosen so that they match those of the corresponding
 746 dataset.

747 To evaluate the interaction of hadrons with detector material, the simulation
 748 uses two different collections of hadronic physics models, called physics lists, in
 749 Geant4 9.4 [17]. The first, QGSP_BERT, combines the Bertini intra-nuclear
 750 cascade [18–20] below 9.9 GeV, a parametrized proton inelastic model from 9.5
 751 to 25 GeV [21], and a quark-gluon string model above 12 GeV [22–26]. The
 752 second, FTFP_BERT, combines the Bertini intra-nuclear cascade [18–20] below
 753 5 GeV and the Fritiof model [27–30] above 4 GeV. In either list, Geant4 en-
 754 forces a smooth transition between models where multiple models overlap.

755 8.1.3 EVENT SELECTION

756 The event selection for this study is minimal, as the only requirement is selecting
 757 good-quality events with an isolated track. Such events are triggered by requir-
 758 ing at least two hits in the minimum-bias trigger scintillators. After trigger, each
 759 event is required to have exactly one reconstructed vertex, and that vertex is re-
 760 quired to have four or more associated tracks.

761 The particles which are selected for the response measurements are first iden-
 762 tified as tracks in the inner detector. The tracks are required to have at least 500
 763 MeV of transverse momentum. To ensure a reliable momentum measurement,
 764 these tracks are required to have at least one hit in the pixel detector, six hits in
 765 the SCT, and small longitudinal and transverse impact parameters with respect
 766 to the primary vertex [11]. For the majority of the measurements in this chapter,

767 the track is additionally required to have 20 hits in the TRT, which significantly
 768 reduces the contribution from tracks which undergo nuclear interactions. This
 769 requirement and its effect is discussed in more detail in Section 8.2.5. In addition,
 770 tracks are rejected if there is any other reconstructed track which extrapolates
 771 to the calorimeter within a cone of $\Delta R = \sqrt{(\Delta\phi)^2 + (\Delta\eta)^2} < 0.4$. This require-
 772 ment guarantees that the contamination of energy from nearby charged particles
 773 is negligible [11].

774 8.2 INCLUSIVE HADRON RESPONSE

775 The calorimeter response is more precisely defined as the ratio of the measured
 776 calorimeter energy to the true energy carried by the particle, although this true
 777 energy is unknown. For charged particles, however, the inner detector provides
 778 a very precise measurement of momentum (with uncertainty less than 1%) that
 779 can be used as a proxy for true energy. The ratio of the energy deposited by
 780 the charged particle in the calorimeter, E , to its momentum measured in the
 781 inner detector p , forms the calorimeter response measure called E/p . Though
 782 the distribution of E/p contains a number of physical features, this study focuses
 783 on the trends in two aggregated quantities: $\langle E/p \rangle$, the average of E/p for the
 784 selected tracks, and the zero fraction, the fraction of tracks with no associated
 785 energy in the calorimeter for those tracks.

786 The calorimeter energy assigned to a track is defined using clusters. The clus-
 787 ters are formed using a 4–2–0 algorithm [31] that begins with seeds requiring
 788 at least 4 times the average calorimeter cell noise. The neighboring cells with
 789 at least twice that noise threshold are then added to the cluster, and all bound-
 790 ing cells are then added with no requirement. This algorithm minimizes noise
 791 contributions through its seeding process, and including the bounding cells im-
 792 proves the energy resolution [32]. The clusters are associated to a given track
 793 if they fall within a cone of $\Delta R = 0.2$ of the extrapolated position of the track,
 794 which includes about 90% of the energy on average [11]. This construction is
 795 illustrated in Figure 6.

796 8.2.1 E/P DISTRIBUTION

797 The E/p distributions measured in both data and simulation are shown in Fig-
 798 ure 7 for two example bins of track momentum and for tracks in the central
 799 region of the detector. These distributions show several important features of
 800 the E/p observable. The large content in the bin at $E = 0$ comes from tracks that
 801 have no associated cluster, which occurs due to interactions with detector mate-
 802 rial prior to reaching the calorimeter or the energy deposit being insufficiently
 803 large to generate a seed, and are discussed in Section 8.2.2. The small negative
 804 tail also comes from tracks that do not deposit any energy in the calorimeter but
 805 are randomly associated to a cluster with an energy below the noise threshold.
 806 The long positive tail above 1.0 comes from the contribution of neutral parti-
 807 cles. Nearby neutral particles deposit (sometimes large) additional energy in the
 808 calorimeter but do not produce tracks in the inner detector, so they cannot be

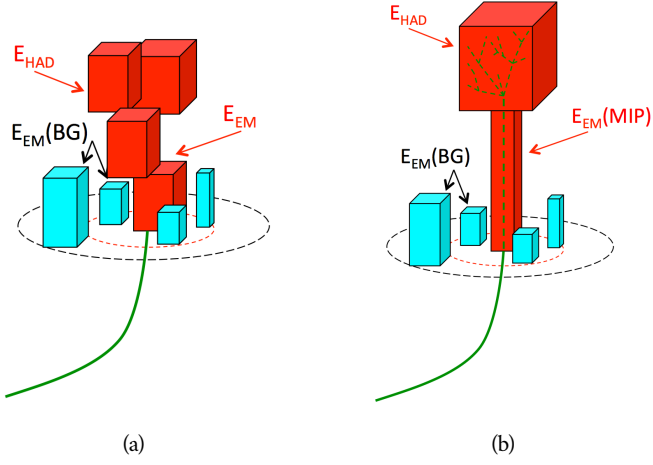


Figure 6: An illustration (a) of the E/p variable used throughout this paper. The red energy deposits come from the charged particle targeted for measurement, while the blue energy deposits are from nearby neutral particles and must be subtracted. The same diagram (b) for the neutral-background selection, described in Section 8.2.3.

809 rejected by the track isolation requirement. Additionally the peak and mean of
 810 the distribution falls below 1.0 because of the loss of energy not found within
 811 the cone as well as the non-compensation of the calorimeter.

812 The data and simulation share the same features, but the high and low tails
 813 are significantly different. The simulated events tend to overestimate the con-
 814 tribution of neutral particles to the long tail, an effect which can be isolated and
 815 removed as discussed in Section 8.2.3. Additionally, the simulated clusters have
 816 less noise on average, although this is a small effect on the overall response.

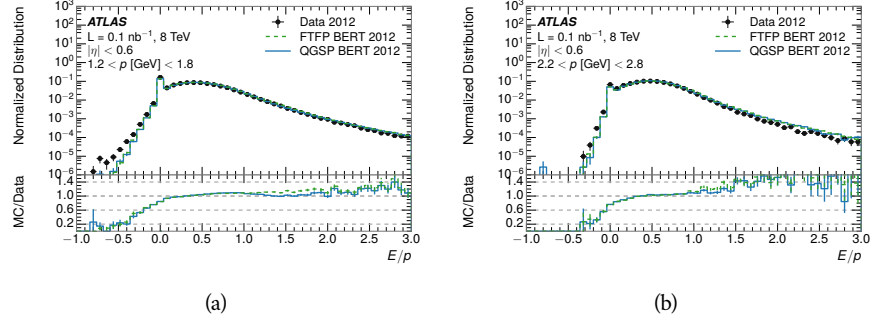


Figure 7: The E/p distribution and ratio of simulation to data for isolated tracks with
 (a) $|\eta| < 0.6$ and $1.2 < p/\text{GeV} < 1.8$ and (b) $|\eta| < 0.6$ and $2.2 < p/\text{GeV} < 2.8$.

817 8.2.2 ZERO FRACTION

818 The fraction of particles with no associated clusters, or similarly those with $E \leq$
 819 0, reflects the modeling of both the detector geometry and hadronic interactions.

820 The zero fraction is expected to rise as the amount of material a particle traverses
 821 increases, while it is expected to decrease as the particle energy increases. This
 822 dependence can be seen in Figure 8, where the zero fraction in data and simulation
 823 is shown as a function of momentum and the amount of material measured
 824 in interaction lengths. The trends are similar between 2010 and 2012 and for
 825 positively and negatively charged particles. The zero fraction decreases with
 826 energy as expected. The absolute discrepancy in zero fraction decreases with
 827 momentum from 5% to less than 1%, but this becomes more pronounced in the
 828 ratio as the zero fraction shrinks quickly with increasing momentum. There is
 829 a small constant difference between the data and simulation in both interaction
 830 models that becomes more pronounced. The amount of material in the detector
 831 increases with η , which is used to obtain results for interaction lengths ranging
 832 between 0.1 and 0.65 λ . As the data and simulation have significant disagree-
 833 ment in the zero fraction over a number of interaction lengths, the difference
 834 must be primarily from the modeling of hadronic interactions with detector ma-
 835 terial and not just the detector geometry. Although two different hadronic in-
 836 teraction models are shown in the figure, they have very similar discrepancies to
 837 data because both use the same description (the BERT model) at low momentum.

838 8.2.3 NEUTRAL BACKGROUND SUBTRACTION

839 The isolation requirement on hadrons is only effective in removing an energy
 840 contribution from nearby charged particles. Nearby neutral particles, predomi-
 841 nantly photons from π^0 decays, also add their energy to the calorimeter clusters,
 842 but mostly in the electromagnetic calorimeter. It is possible to measure this con-
 843 tribution, on average, using late-showering hadrons that minimally ionize in the
 844 electromagnetic calorimeter. Such particles are selected by requiring that they
 845 deposit less than 1.1 GeV in the EM calorimeter within a cone of $\Delta R < 0.1$
 846 around the track. To ensure that these particles are well measured, they are addi-
 847 tionally required to deposit between 40% and 90% of their energy in the hadronic
 848 calorimeter within the same cone.

849 These particles provide a clean sample to measure the nearby neutral back-
 850 ground because they do not deposit energy in the area immediately surrounding
 851 them in the EM calorimeter, as shown in Figure 6. So, the energy deposits in the
 852 region $0.1 < \Delta R < 0.2$ can be attributed to neutral particles alone. To estimate
 853 the contribution to the whole cone considered for the response measurement,
 854 that energy is scaled by a geometric factor of $4/3$. This quantity, $\langle E/p \rangle_{BG}$, mea-
 855 sured in aggregate over a number of particles, gives the contribution to $\langle E/p \rangle$
 856 from neutral particles in the EM calorimeter. Similar techniques were used in
 857 the individual layers of the hadronic calorimeters to show that the background
 858 from neutrals is negligible in those layers [11].

859 The distribution of this background estimate is shown in Figure 9 for data
 860 and simulation with the two different physics lists. The contribution from neu-
 861 tral particles falls from 0.1 at low momentum to around 0.03 for particles above
 862 7 GeV. Although the simulation captures the overall trend, it significantly over-
 863 estimates the neutral contribution for tracks with momentum between 2 and 8

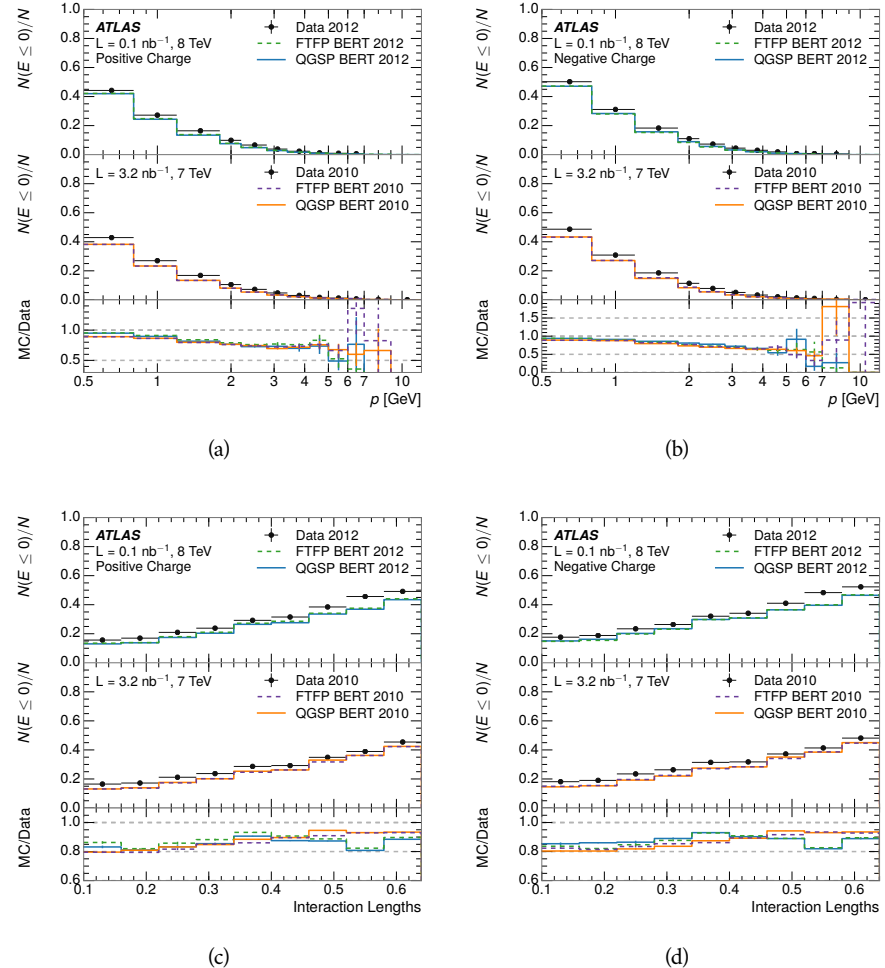


Figure 8: The fraction of tracks as a function (a, b) of momentum, (c, d) of interaction lengths with $E \leq 0$ for tracks with positive (on the left) and negative (on the right) charge.

864 GeV. This effect was also seen in the tails of the E/p distributions in Figure 7.
 865 This difference is likely due to modeling of coherent neutral particle radiation
 866 in Pythia8 that overestimates the production of π^0 near the production of the
 867 charged particles. The discrepancy does not depend on η and thus is unlikely to
 868 be a mismodeling of the detector. This difference can be subtracted to form a
 869 corrected average E/p , as in Section 8.2.4.

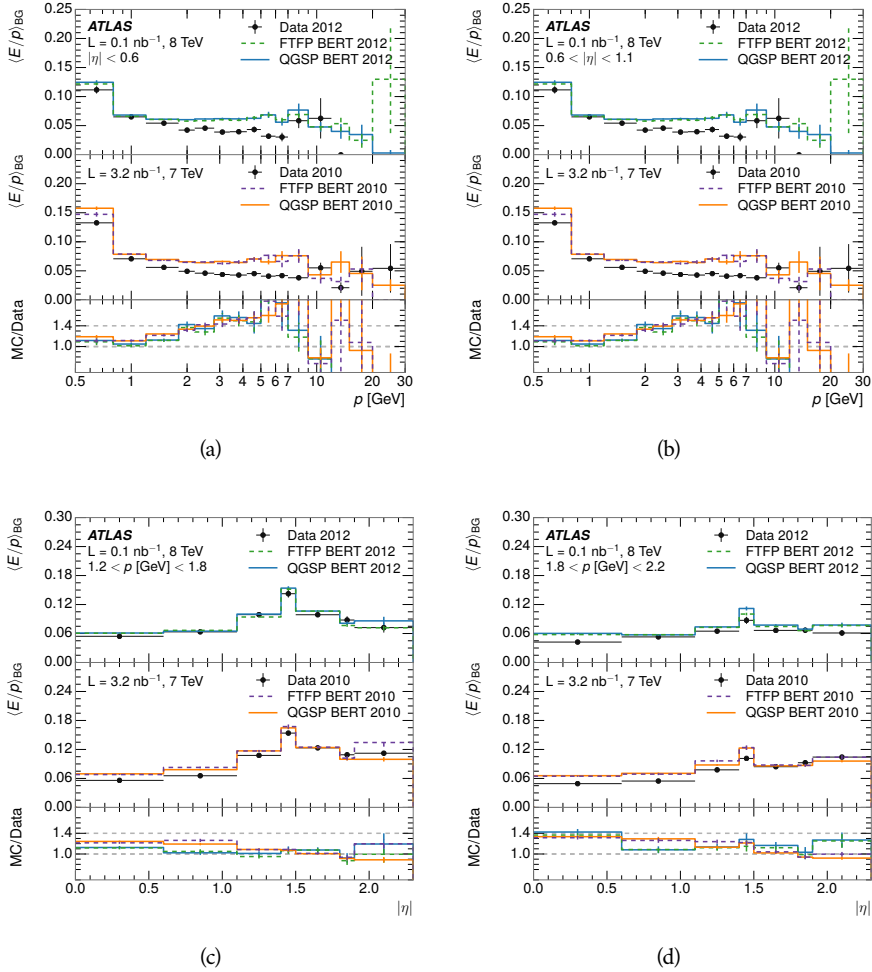


Figure 9: $\langle E/p \rangle_{\text{BG}}$ as a function of the track momentum for tracks with (a) $|\eta| < 0.6$, (b) $0.6 < |\eta| < 1.1$, and as a function of the track pseudorapidity for tracks with (c) $1.2 < p/\text{GeV} < 1.8$, (d) $1.8 < p/\text{GeV} < 2.2$.

870 8.2.4 CORRECTED RESPONSE

871 Figure 10 shows $\langle E/p \rangle_{\text{COR}}$ as a function of momentum for several bins of pseudo-
 872 rapidity. This corrected $\langle E/p \rangle_{\text{COR}} \equiv \langle E/p \rangle - \langle E/p \rangle_{\text{BG}}$ measures the average
 873 calorimeter response without the contamination of neutral particles. It is the
 874 most direct measurement of calorimeter response in that it is the energy mea-
 875 sured for fully isolated hadrons. The correction is performed separately in data
 876 and simulation, so that the mismodeling of the neutral background in simulation

is removed from the comparison of response. The simulation overestimates the response at low momentum by about 5%, an effect that can be mostly attributed to the underestimation of the zero fraction mentioned previously. For $|\eta| < 0.6$, the data-simulation agreement has a larger discrepancy by about 5% for 2010 than 2012, although this is not reproduced in at higher pseudorapidity.

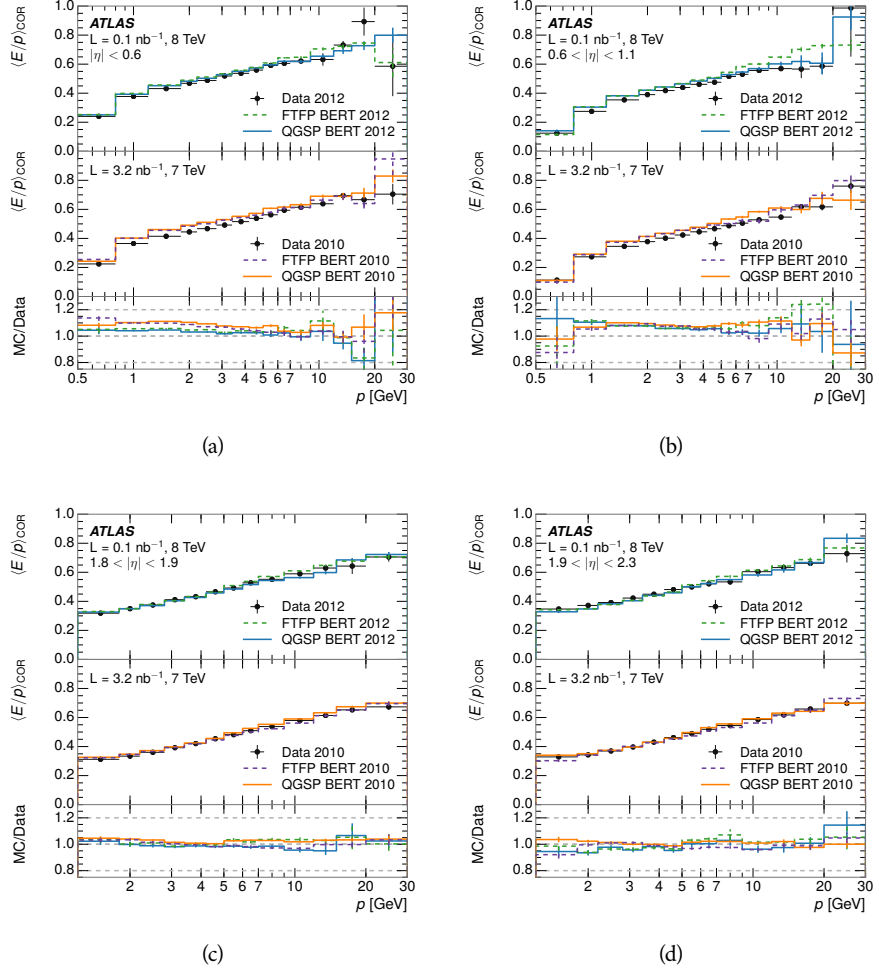


Figure 10: $\langle E/p \rangle_{\text{COR}}$ as a function of track momentum, for tracks with (a) $|\eta| < 0.6$, (b) $0.6 < |\eta| < 1.1$, (c) $1.8 < |\eta| < 1.9$, and (d) $1.9 < |\eta| < 2.3$.

The response measurement above used topological clustering at the EM scale, that is clusters were formed to measure energy but no corrections were applied to correct for expected effects like energy lost outside of the cluster or in uninstrumented material. It is also interesting to measure $\langle E/p \rangle_{\text{COR}}$ using local cluster weighted (LCW) energies, which accounts for those effects by calibrating the energy based on the properties of the cluster such as energy density and depth in the calorimeter. Figure 11 shows these distributions for tracks with zero or more clusters and separately for tracks with one or more clusters. The calibration moves the mean value of $\langle E/p \rangle_{\text{COR}}$ significantly closer to 1.0 as desired. The agreement between data and simulation improves noticeably when at least one cluster is required, as this removes the contribution from the mismodeling of

the zero fraction. The good agreement in that case again demonstrates that the difference in $\langle E/p \rangle_{\text{COR}}$ between data and simulation is caused predominantly by the difference in zero fraction.

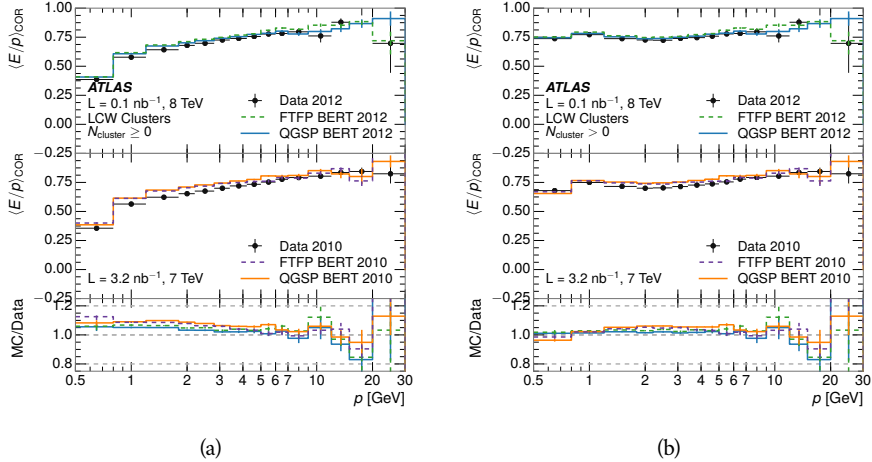


Figure 11: $\langle E/p \rangle_{\text{COR}}$ calculated using LCW-calibrated topological clusters as a function of track momentum for tracks with (a) zero or more associated topological clusters or (b) one or more associated topological clusters.

8.2.5 ADDITIONAL STUDIES

As has been seen in several measurements in previous sections, the simulation does not correctly model the chance of a low momentum hadron to reach the calorimeter. Because of the consistent discrepancy across pseudorapidity and interaction lengths, this can be best explained by incomplete understanding of hadronic interactions with the detector [10]. For example, a hadron that scatters off of a nucleus in the inner detector can be deflected through a significant angle and not reach the expected location in the calorimeter. In addition, these interactions can produce secondary particles that are difficult to model.

The requirement used throughout the previous sections on the number of hits in the TRT reduces these effects by preferentially selecting tracks that do not undergo nuclear interactions. It is interesting to check how well the simulation models tracks with low numbers of TRT hits, which selects tracks that are more likely to have undergone a hadronic interaction. Figure 12 compares the distributions with $N_{\text{TRT}} < 20$ to $N_{\text{TRT}} > 20$ for real and simulated particles. As expected, the tracks with fewer hits are poorly modeled in the simulation as $\langle E/p \rangle_{\text{COR}}$ differs by as much as 25% at low momentum.

Another interesting aspect of the simulation is the description of antiprotons at low momentum, where QGSP_BERT and FTFP_BERT have significant differences. This can be seen to have an effect in the inclusive response measurement when separated into positive and negative charge. The $\langle E/p \rangle_{\text{COR}}$ distributions for positive and negative particles are shown in Figure 13, where a small difference between QGSP_BERT and FTFP_BERT can be seen in the distribution for

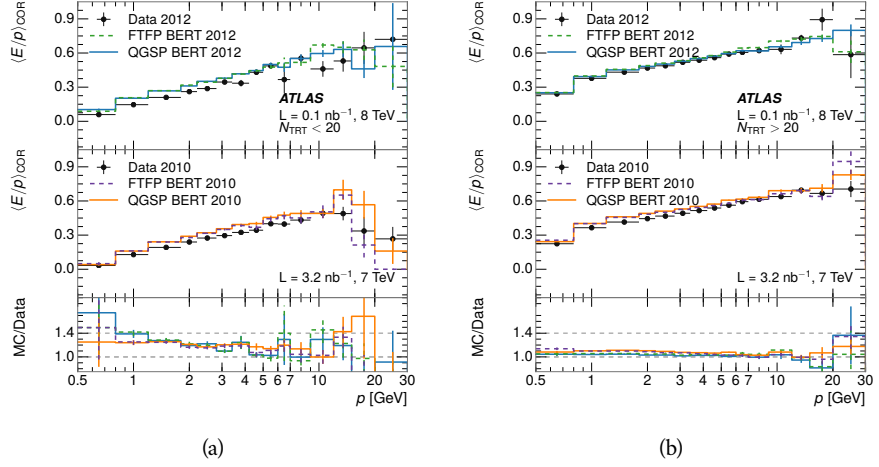


Figure 12: Comparison of the $\langle E/p \rangle_{\text{COR}}$ for tracks with (a) less than and (b) greater than 20 hits in the TRT.

negative tracks. This is demonstrated more clearly in Figure 14, which shows the E/p distribution in the two simulations separated by charge. There is a clear difference around $E/p > 1.0$, which can be explained by the additional energy deposited by the annihilation of the antiproton in the calorimeter that is modeled well only in FTFP_BERT. This is also explored with data using identified antiprotons in Section 8.3.

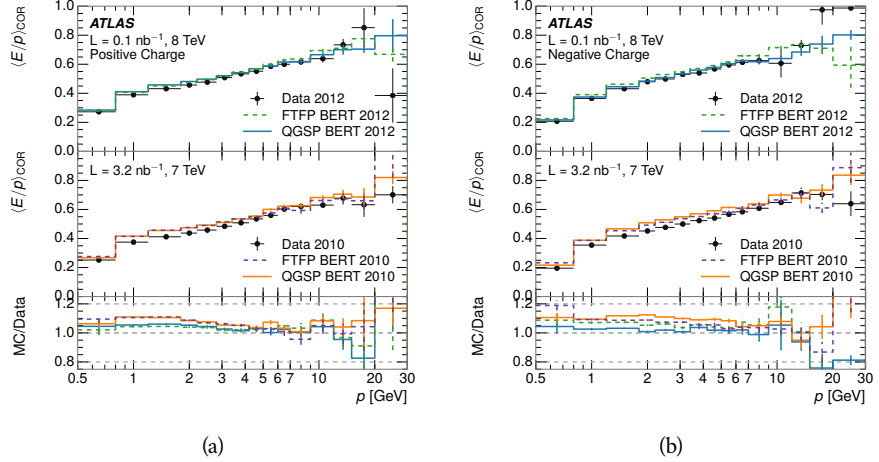


Figure 13: Comparison of the $\langle E/p \rangle_{\text{COR}}$ for (a) positive and (b) negative tracks as a function of track momentum for tracks with $|\eta| < 0.6$.

The $\langle E/p \rangle$ results in previous sections have considered the electromagnetic and hadronic calorimeters together as a single energy measurement, to emphasize the total energy deposited for a given particle. However, the deposits in each calorimeter are available separately and $\langle E/p \rangle$ can be constructed for each layer. As the layers are composed of different materials and are modeled separately in the detector geometry, confirmation that the simulation matches the data well

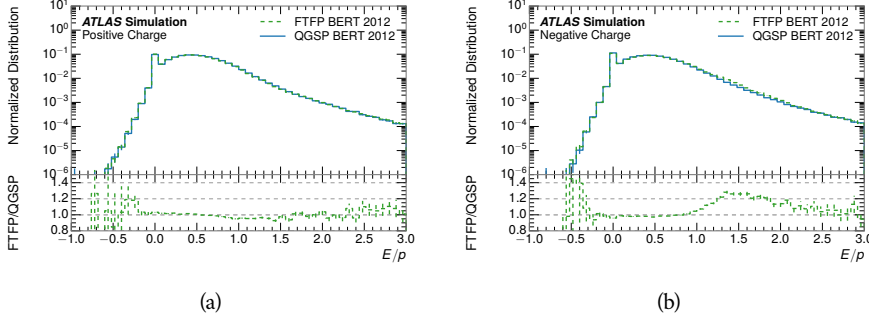


Figure 14: Comparison of the E/p distributions for (a) positive and (b) negative tracks with $0.8 < p/\text{GeV} < 1.2$ and $|\eta| < 0.6$, in simulation with the FTFP_BERT and QGSP_BERT physics lists.

in each layer adds confidence in both the description of hadronic interactions with the two different materials and also the geometric description of each.

The technique discussed in Section 8.2.3 for selecting minimally ionizing particle (MIP)s in the electromagnetic calorimeter is also useful in studying deposits in the hadronic calorimeter. Those MIPs deposit almost all of their energy exclusively in the hadronic calorimeter. Figure 15 shows $\langle E/p \rangle_{\text{RAW}}^{\text{Had}}$, where RAW indicates that no correction has been applied for neutral backgrounds and Had indicates that only clusters for the hadronic calorimeter are included. The RAW and COR versions of $\langle E/p \rangle$ in this case are the same, as the neutral background is negligible in that calorimeter layer. The distributions are shown both for the original EM scale calibration and after LCW calibration. The data and simulation agree very well in this comparison, except in the lowest momentum bin which has 5% discrepancy that has already been seen in similar measurements.

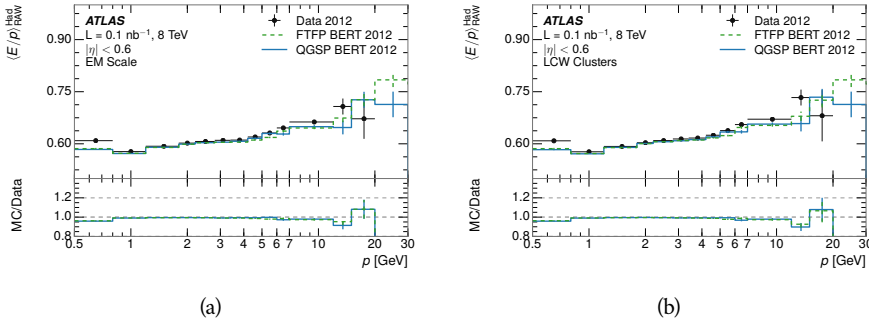


Figure 15: Comparison of the response of the hadronic calorimeter as a function of track momentum (a) at the EM-scale and (b) after the LCW calibration.

A similar comparison can be made in the electromagnetic calorimeter by selecting particles which have no associated energy in the hadronic calorimeter. These results are measured in terms of $\langle E/p \rangle_{\text{COR}}^{\text{EM}}$, where EM designates that only clusters in the electromagnetic calorimeter are included and COR designates that the neutral background is subtracted as the neutral background is present in this case. Figure 16 shows the analogous comparisons to Figure 15 in

950 the electromagnetic calorimeter. In this case the disagreement between data and
 951 simulation is more pronounced, with discrepancies as high as 5% over a larger
 952 range of momenta. This level of discrepancy indicates that the description of
 953 the electromagnetic calorimeter is actually the dominant source of discrepancy
 954 in the combined distributions in Section 8.2.4.

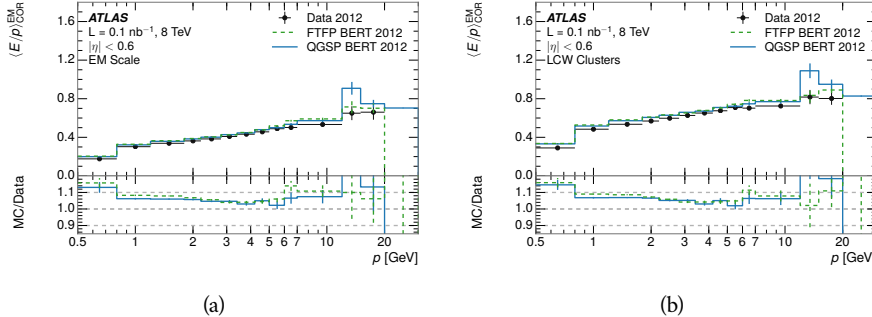


Figure 16: Comparison of the response of the EM calorimeter as a function of track momentum (a) at the EM-scale and (b) with the LCW calibration.

955 **NOTE: There are more studies that I skipped for brevity that could be in-**
 956 **cluded if interesting. E/p at different cluster threshold settings, E/p with**
 957 **pileup, E/p with cells. I also left out a lot of eta bins that appear in the**
 958 **paper so that this section didn't turn into 20 pages of plots.**

959 8.3 IDENTIFIED PARTICLE RESPONSE

960 The inclusive response measurement for hadrons can be augmented by measuring
 961 the response for specific particle species. The simulation models each parti-
 962 cle type separately, and understanding the properties of each is important in con-
 963 straining the uncertainty on jets. In order to select and measure specific hadrons,
 964 this section relies on the displaced decays of long-lived particles. Such decays
 965 can be identified by reconstructing secondary vertices with a requirement on
 966 mass. In particular, Λ , $\bar{\Lambda}$, and K_S^0 can be used to select a pure sample of protons,
 967 antiprotons, and pions, respectively.

968 8.3.1 DECAY RECONSTRUCTION

969 The measurement of response for identified particles uses the same selection as
 970 for inclusive particles (Section 8.1.3) with a few additions. Each event used is
 971 required to have at least one secondary vertex, and the tracks are required to
 972 match to that vertex rather than the primary vertex. Pions are selected from
 973 decays of $K_S^0 \rightarrow \pi^+ \pi^-$, which is the dominant decay for K_S^0 to charged particles.
 974 Protons are selected from decays of $\Lambda \rightarrow \pi^- p$ and antiprotons from $\bar{\Lambda} \rightarrow \pi^+ \bar{p}$,
 975 which are similarly the dominant decays of Λ and $\bar{\Lambda}$ to charged particles. The
 976 species of parent hadron in these decays is determined by reconstructing the
 977 mass of the tracks associated to the secondary vertex. The sign of the higher

momentum decay particle can distinguish between Λ and $\bar{\Lambda}$, which of course have the same mass, as the proton or antiproton is kinematically favored to have higher momentum. Examples of the reconstructed masses used to select these decays are shown in Figure 17.

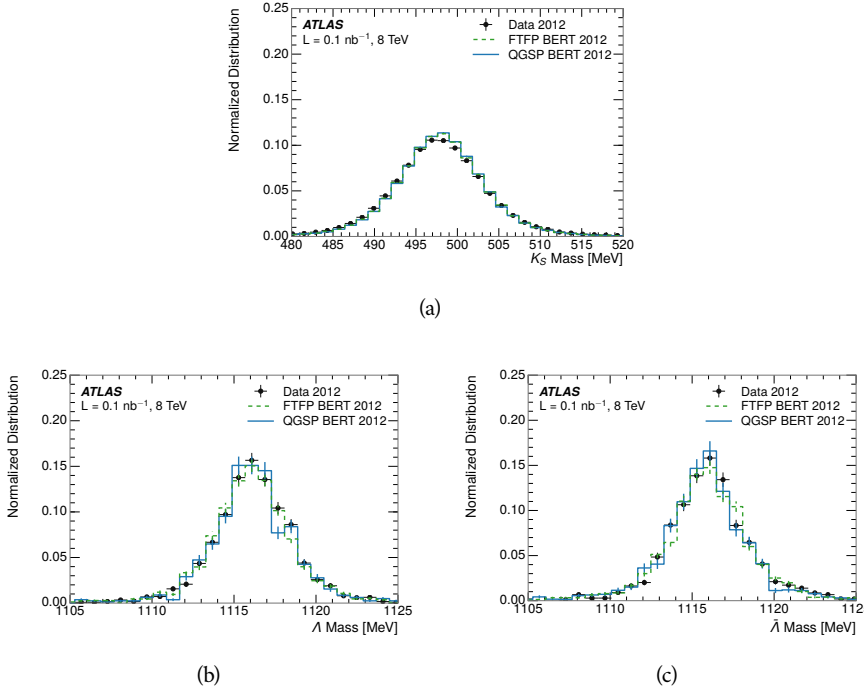


Figure 17: The reconstructed mass peaks of (a) K_S^0 , (b) Λ , and (c) $\bar{\Lambda}$ candidates.

The dominant backgrounds for the identified particle decays are nuclear interactions and combinatoric sources. These are suppressed by the kinematic requirements on the tracks as well as an additional veto which removes candidates that are consistent with both a Λ or $\bar{\Lambda}$ and a K_S^0 hypothesis, which is possible because of the different assumptions on particle mass in each case [11]. After these requirements, the backgrounds are found to be negligible compared to the statistical errors on these measurements.

8.3.2 IDENTIFIED RESPONSE

With these techniques the E/p distributions are extracted in data and simulation for each particle species and shown in Figure 18. These distributions are shown for a particular bin of E_a ($2.2 < E_a/\text{GeV} < 2.8$), rather than p . E_a is the energy available to be deposited in the calorimeter: for pions $E_a = \sqrt{p^2 + m^2}$, for protons $E_a = \sqrt{p^2 + m^2} - m$, and for antiprotons $E_a = \sqrt{p^2 + m^2} + m$. The features of the E/p distributions are similar to the inclusive case. There is a small negative tail from noise and a large fraction of tracks with zero energy from particles which do not reach the calorimeter. The long positive tail is noticeably more pronounced for antiprotons because of the additional energy generated by the annihilation in addition to the neutral background.

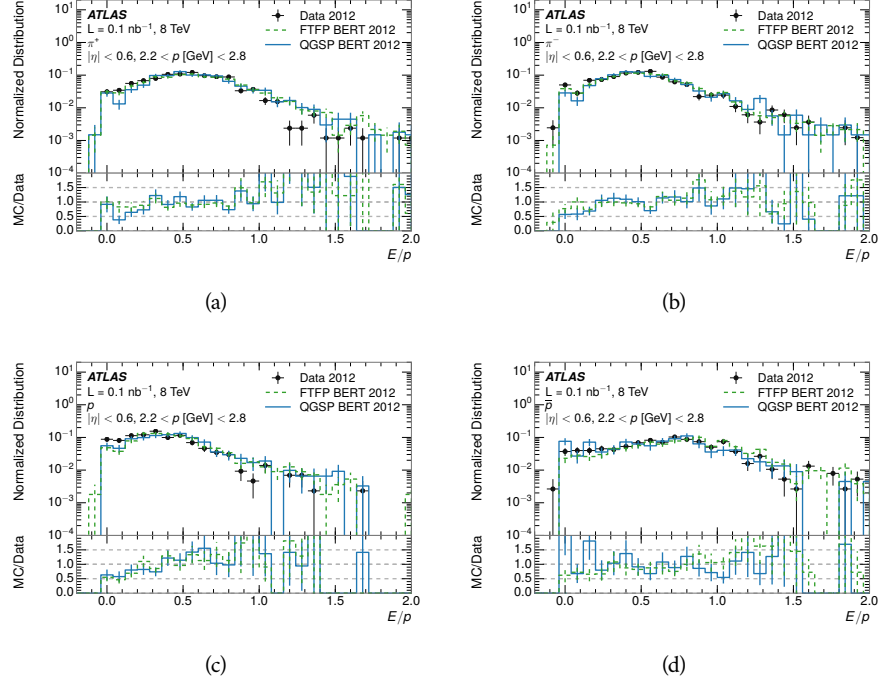


Figure 18: The E/p distribution for isolated (a) π^+ , (b) π^- , (c) proton, and (d) anti-proton tracks.

1000 The zero fraction is further explored in Figure 19 for pions and protons in data
 1001 and simulation. The simulation consistently underestimates the zero fraction
 1002 independent of particle species, which implies that this discrepancy is not caused
 1003 by the model of a particular species but rather a feature common to all.

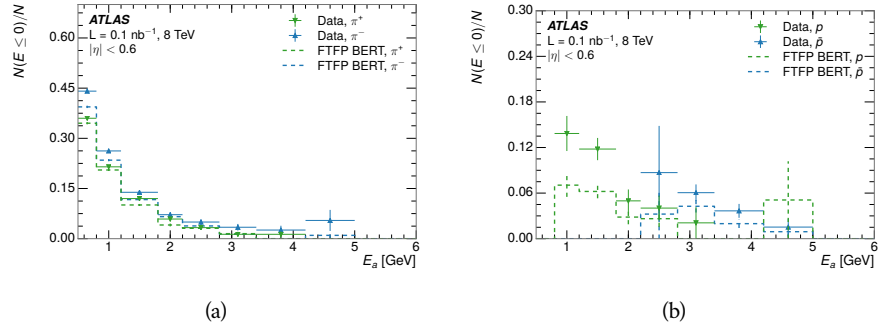


Figure 19: The fraction of tracks with $E \leq 0$ for identified (a) π^+ and π^- , and (b) proton and anti-proton tracks

1004 It is also interesting to compare the response between the different particle
 1005 species. One approach to do this is to measure the difference in $\langle E/p \rangle$ between
 1006 two types, which has the advantage of removing the neutral background. These
 1007 differences are shown in various combinations in Figure 20. The response for
 1008 π^+ is greater on average than the response to π^- because of a charge-exchange
 1009 effect which causes the production of additional neutral pions in the showers of

1010 π^+ [33]. The response for π^+ is also greater on average than the response to p ,
 1011 because a large fraction of the energy of π^+ hadrons is converted to an electro-
 1012 magnetic shower [34, 35]. However, the \bar{p} response is significantly higher than
 1013 the response to π^- because of the annihilation of the antiproton. FTFP_BERT
 1014 does a better job of modeling this effect than QGSP_BERT because of their differ-
 1015 ent descriptions of \bar{p} interactions with material.

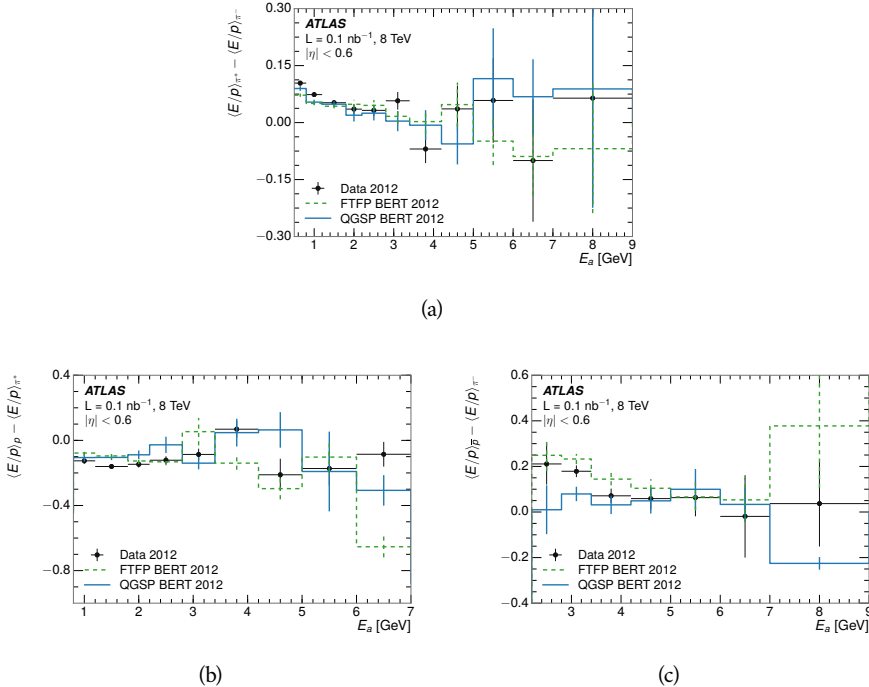


Figure 20: The difference in $\langle E/p \rangle$ between (a) π^+ and π^- (b) p and π^+ , and (c) \bar{p} and π^- .

1016 It is also possible to remove the neutral background from these response dis-
 1017 tributions using the same technique as in Section 8.2.3. The technique is largely
 1018 independent of the particle species and so can be directly applied to $\langle E/p \rangle$ for
 1019 pions. The $\langle E/p \rangle_{\text{COR}}$ distributions for pions are shown in Figure 21, which are
 1020 very similar to the inclusive results. The inclusive hadrons are comprised mostly
 1021 of pions, so this similarity is not surprising. It is also possible to see the small
 1022 differences between π^+ and π^- response here, where $\langle E/p \rangle_{\text{COR}}$ is higher on av-
 1023 erage for π^+ . The agreement between data and simulation is significantly worse
 1024 for the π^- distributions than for the π^+ , with a discrepancy greater than 10%
 1025 below 2-3 GeV.

1026 8.3.3 ADDITIONAL SPECIES IN SIMULATION

1027 The techniques above provide a method to measure the response separately for
 1028 only pions and protons. However the hadrons which forms jets include a num-
 1029 ber of additional species such as kaons and neutrons. The charged kaons are
 1030 an important component of the inclusive charged hadron distribution, which is
 1031 comprised of roughly 60-70% pions, 15-20% kaons, and 5-15% protons. These

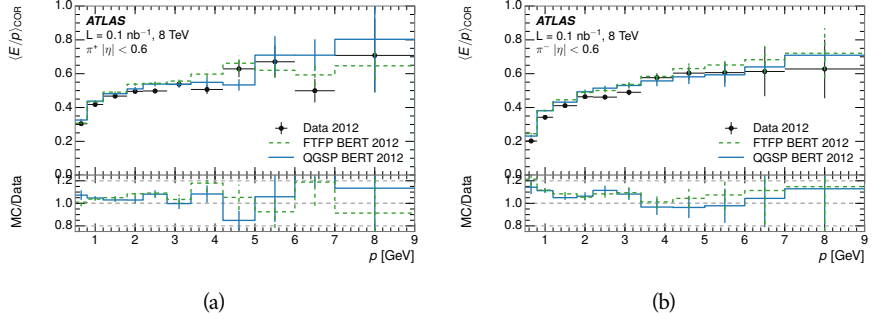


Figure 21: $\langle E/p \rangle_{\text{COR}}$ as a function of track momentum for (a) π^+ tracks and (b) π^- tracks.

are difficult to measure in data at the ATLAS detector, although a template subtraction technique has been proposed which may be effective with larger sample sizes [10]. The simulation of these particles includes noticeable differences in response at low energies, which are shown in Figure 22 for FTFP_BERT. The significant differences in response between low energy protons and antiprotons are accounted for above in the definitions of E_a .

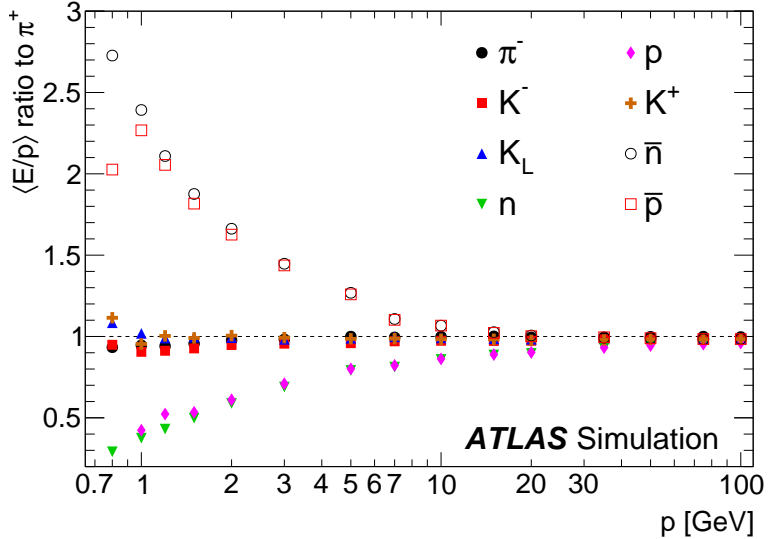


Figure 22: The ratio of the calorimeter response to single particles of various species to the calorimeter response to π^+ with the physics list FTFP_BERT.

8.4 SUMMARY

These various measurements of calorimeter response shown above for data and simulation illuminate the accuracy of the simulation of hadronic interactions at the ATLAS detector. The results were done using 2010 and 2012 data at 7 and 8 TeV, but reflect the most current understanding of the detector alignment and geometry. A number of measurements focusing on a comparison between pro-

1044 tons and antiprotons suggest that FTFP_BERT models those interaction more
1045 accurately than QGSP_BERT. These measurements, among others, were the moti-
1046 vation to switch the default Geant4 simulation from FTFP_BERT to QGSP_BERT
1047 for all ATLAS samples.

1048 Even with these updates, there are a number of small, approximately 5%, dis-
1049 crepancies in response between the data and simulation at low energies. At
1050 higher energies the simulation of hadronic interactions is very consistent with
1051 data. Chapter 9 discusses how to use these observed differences to constrain the
1052 jet energy scale and its associated uncertainties.

1053

1054 JET ENERGY RESPONSE AND UNCERTAINTY

1055 9.1 MOTIVATION

1056 As jets form a major component of many physics analyses at ATLAS, it is crucial
 1057 to carefully calibrate the measurement of jet energies and to derive an uncer-
 1058 tainty on that measurement. These uncertainties have often been the dominant
 1059 systematic uncertainty in high-energy analyses at the LHC. Dijet and multijet
 1060 balance techniques provide a method to constrain the JES and its uncertainty in
 1061 data, and provide the default values used for ATLAS jet measurements at most
 1062 energies [36]. These techniques are limited by their reliance on measuring jets
 1063 in data, so they are statistically limited in estimating the jet energy scale at the
 1064 highest jet energies. This chapter presents another method for estimating the jet
 1065 energy scale and its uncertainty which builds up a jet from its components and
 1066 thus can be naturally extended to high jet momentum. Throughout this chapter
 1067 the jets studied are simulated using Pythia8 with the CT10 parton distribution
 1068 set [37] and the AU2 tune [14], and corrections are taken from the studies includ-
 1069 ing data and simulation in Chapter 8.

1070 As described in Section 7.2, jets are formed from topological clusters of energy
 1071 in the calorimeters using the anti- k_t algorithm. These clusters originate from a
 1072 diverse spectrum of particles, in terms of both species and momentum, leading to
 1073 significantly varied jet properties and response between jets of similar produced
 1074 momentum. Figure 23 shows the simulated distribution of particles within jets
 1075 at a few examples energies. The E/p measurements provide a thorough under-
 1076 standing of the dominant particle content of jets, the charged hadrons.

1077 9.2 UNCERTAINTY ESTIMATE

1078 Simulated jets are not necessarily expected to correctly model the energy de-
 1079 posits in the calorimeters, because of the various discrepancies discussed in Chap-
 1080 ter 8. To evaluate a jet energy response, the simulated jet energies are compared
 1081 to a corrected jet built up at the particle level. Each cluster in a jet is associated
 1082 to the truth particle which deposited it, and the energy in that cluster is then
 1083 corrected for a number of effects based on measurements in data. The primary
 1084 corrections come from the single hadron response measurements in addition to
 1085 response measured using the combined test beam which covers higher momen-
 1086 tum particles [38]. These corrections include both a shift (Δ), in order to make
 1087 the simulation match the average response in data, and an uncertainty (σ) asso-
 1088 ciated with the ability to constrain the difference between data and simulation.
 1089 Some of the dominant sources of uncertainty are itemized in Table 1 with typi-
 1090 cal values, and the full list considered is described in detail in the associated pa-

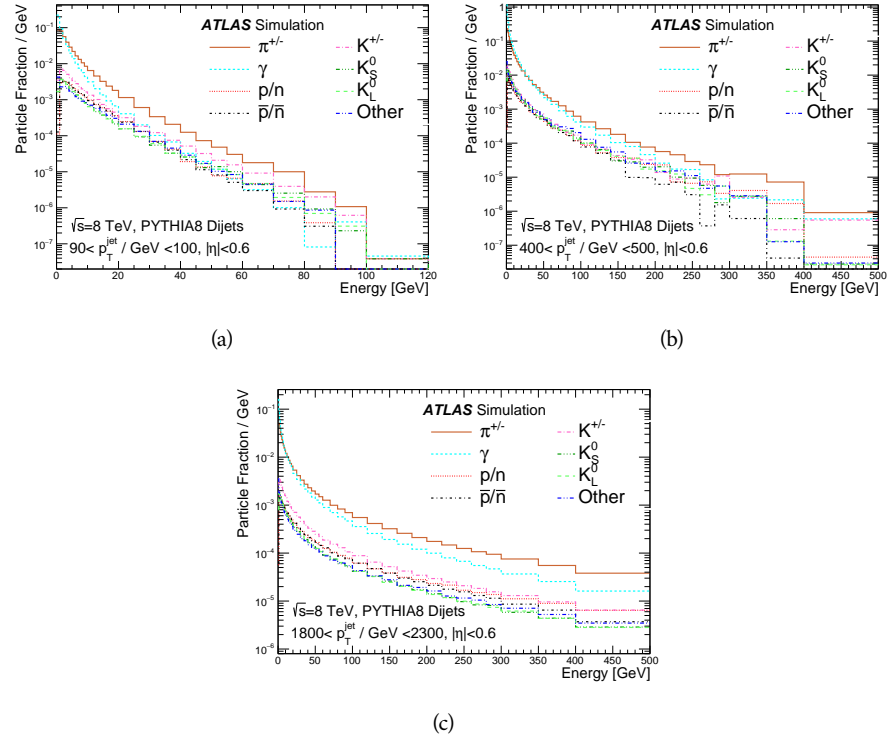


Figure 23: The spectra of true particles inside anti- k_t , $R = 0.4$ jets with (a) $90 < p_T/\text{GeV} < 100$, (b) $400 < p_T/\text{GeV} < 500$, and (c) $1800 < p_T/\text{GeV} < 2300$.

1091 per [10]. These uncertainties cover differences between the data and simulation
 1092 in the modeling of calorimeter response to a given particle. No uncertainties are
 1093 added for the difference between particle composition of jets in data and simu-
 1094 lation.

1095 From these terms, the jet energy scale and uncertainty is built up from indi-
 1096 vidual energy deposits in simulation. Each uncertainty term is treated indepen-
 1097 dently, and are taken to be gaussian distributed. The resulting scale and uncer-
 1098 tainty is shown in Figure 24, where the mean response is measured relative to
 1099 the calibrated energy reported by simulation. The dominant uncertainties come
 1100 from the statistical uncertainties on the E/p measurements at lower energies and
 1101 the additional uncertainty for out of range measurements at higher energies. The
 1102 total uncertainty from this method at intermediate jet energies is comparable to
 1103 other simulation-based methods [39] and is about twice as large as in-situ meth-
 1104 ods using data [36]. This method is the only one which provides an estimation
 1105 above 1.8 TeV, however, and so is still a crucial technique in analyses that search
 1106 for very energetic jets.

1107 These techniques can also be used to measure the correlation between bins of
 1108 average reconstructed jet momentum across a range of p_T and $|\eta|$, where cor-
 1109 relations are expected because of a similarity in particle composition at similar
 1110 energies. Figure 25 shows these correlations, where the uncertainties on jets in
 1111 neighboring bins are typically between 30% and 60% correlated. The uncertainty
 1112 on all jets becomes significantly correlated at high energies and larger pseudora-

Abbrev.	Description	Δ (%)	σ (%)
In situ E/p	The comparison of $\langle E/p \rangle_{\text{COR}}$ as described in Chapter 8 with statistical uncertainties from 500 MeV to 20 GeV.	0-3	1-5
CTB	The main $\langle E/p \rangle$ comparison uncertainties, binned in p and $ \eta $, as derived from the combined test beam results, from 20 to 350 GeV [38].	0-3	1-5
E/p Zero Fraction	The difference in the zero-fraction between data and MC simulation from 500 MeV to 20 GeV.	5-25	1-5
E/p Threshold	The uncertainty in the EM calorimeter response from the potential mismodeling of threshold effects in topological clustering.	0	0-10
Neutral	The uncertainty in the calorimeter response to neutral hadrons based on studies of physics model variations.	0	5-10
K_L	An additional uncertainty in the response to neutral K_L in the calorimeter based on studies of physics model variations.	0	20
E/p Misalignment	The uncertainty in the p measurement from misalignment of the ID.	0	1
Hadrons, $p > 350$ GeV	A flat uncertainty for all particles above the energy range or outside the longitudinal range probed with the combined test beam.	0	10

Table 1: The dominant sources of corrections and systematic uncertainties in the [JES](#) estimation technique, including typical values for the correcting shift (Δ) and the associated uncertainty (σ).

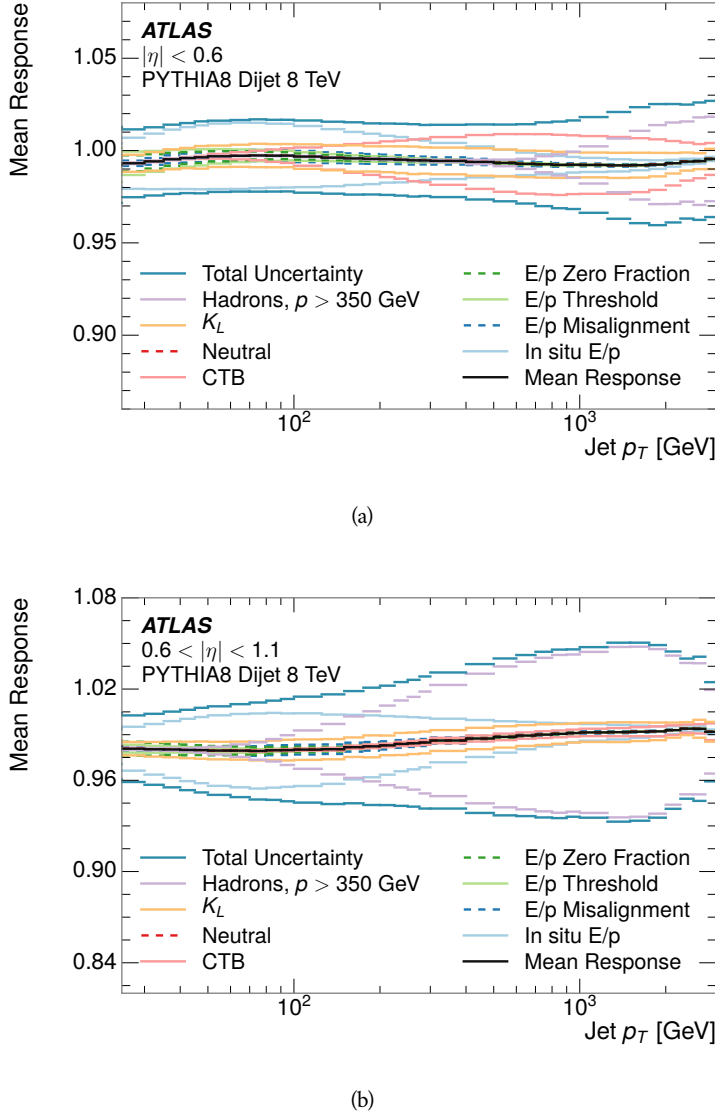


Figure 24: The [JES](#) uncertainty contributions, as well as the total [JES](#) uncertainty, as a function of jet p_T for (a) $|\eta| < 0.6$ and (b) $0.6 < |\eta| < 1.1$.

1113 pidities, when the uncertainty becomes dominated by the single term reflecting
 1114 out of range particles.

1115 9.3 SUMMARY

1116 The technique described above provides a jet energy scale and uncertainty by
 1117 building up jet corrections from the energy deposits of constituent particles. The
 1118 E/p measurements are crucial in providing corrections for the majority of parti-
 1119 cles in the jets. The uncertainty derived this way is between 2 and 5% and is about
 1120 twice as large at corresponding momentum than jet balance methods. However
 1121 this is the only uncertainty available for very energetic jets using 2012 data and
 1122 simulation, and repeating this method with Run 2 data and simulation will be

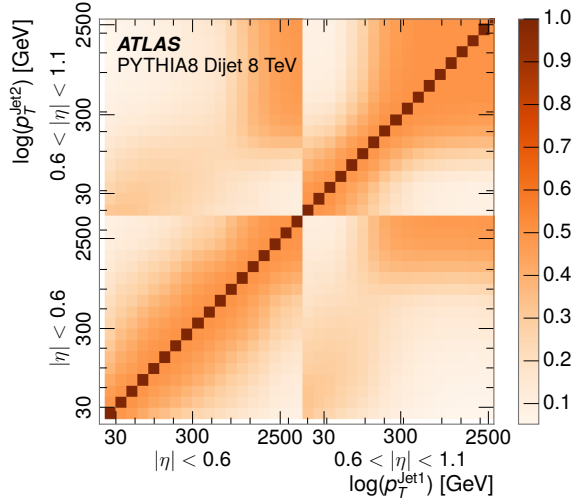


Figure 25: The JES correlations as a function of jet p_T and $|\eta|$ for jets in the central region of the detector.

1123 important in providing an uncertainty for the most energetic jets in 13 TeV col-
1124 lisions.

1125

PART V

1126

SEARCH FOR LONG-LIVED PARTICLES

1127

You can put some informational part preamble text here.

1128

1129 LONG-LIVED PARTICLES IN ATLAS

1130 As discussed in Section 2.3, various limitations in the SM suggest a need for new
 1131 particles at the TeV scale. A wide range of extensions to the Standard Model
 1132 predict that these new particles can have lifetimes greater than approximately
 1133 one-hundredth of a nanosecond. These include theories with universal extra-
 1134 dimensions [40, 41], with new fermions [42], and with leptoquarks [43]. Many
 1135 Supersymmetry (SUSY) theories also produce these Long-Lived Particles (LLPs),
 1136 in both R-Parity violating [44–46] and R-Parity conserving [47–50] formula-
 1137 tions. Split supersymmetry [51, 52], for example, predicts long-lived gluinos
 1138 with $O(\text{TeV})$ masses. This search focuses specifically on the SUSY case, but many
 1139 of the results are generic to any model with LLPs.

1140 Long-lived gluinos or squarks carry color-charge and will thus hadronize into
 1141 color neutral bound states called R-Hadrons. These are composit particles like
 1142 the usual hadrons but with one supersymmetric constituent, for example $\tilde{g}q\bar{q}$
 1143 and $\tilde{q}\bar{q}$. Through this hadronization process, the neutral gluino can acquire a
 1144 charge. Gluino pair production, $pp \rightarrow \tilde{g}\tilde{g}$ has the largest cross sectional increase
 1145 with the increase in energy to 13 TeV, and so this search focuses on gluino R-
 1146 Hadrons. Planned future updates will extend the case to explicitly include squark
 1147 and chargino models, but the method covers any long-lived, charged, massive
 1148 particle.

1149 10.1 EVENT TOPOLOGY

1150 The majority of SUSY models predict that gluinos will be produced in pairs at
 1151 the LHC, through processes like $pp \rightarrow q\bar{q} \rightarrow \tilde{g}\tilde{g}$ and $pp \rightarrow gg \rightarrow \tilde{g}\tilde{g}$, where the
 1152 gluon mode dominates for the collision energy and gluino masses considered
 1153 for this search. During their production, the long-lived gluinos hadronize into
 1154 color singlet bound states including $\tilde{g}q\bar{q}$, $\tilde{g}qqq$, and even $\tilde{g}g$ [53]. The probability
 1155 to form the gluon-only bound states is a free parameter usually taken to be 0.1,
 1156 while the meson states are favored among the R-Hadrons [54]. The charged and
 1157 neutral states are approximately equally likely for mesons, so the R-Hadrons will
 1158 be charged roughly 50% of the time.

1159 These channels produce R-Hadrons with large p_T , comparable to their mass,
 1160 so that they typically propagate with $0.2 < \beta < 0.9$ [54]. The fragmentation that
 1161 produces that hadrons is very hard, so the jet structure around the R-Hadron
 1162 is minimal, with less than 5 GeV of summed particle momentum expected in a
 1163 cone of $\Delta R < 0.25$ around the R-Hadron [54]. After hadronization, depending
 1164 on the gluino lifetime, the R-Hadrons then decay into hadrons and a LSP [53].

1165 In summary, the expected event for pair-produced long-lived gluinos is very
 1166 simple: two isolated, high-momentum R-Hadrons that propagate through the
 1167 detector before decaying into jets. The observable features of such events depend

1168 strongly on the interaction of the R-Hadron with the material of the detector and
 1169 also its lifetime. Section 10.1.1 describes the interactions of R-Hadrons which
 1170 reach the various detector elements in ATLAS and Section 10.1.2 provides a sum-
 1171 mary of the observable event descriptions for R-Hadrons of various lifetimes.

1172 10.11 DETECTOR INTERACTIONS

1173 After approximately 0.2 ns, the R-Hadron reaches the pixel detector. If charged,
 1174 it deposits energy into the material through repeated single collisions that result
 1175 in ionization of the silicon substrate [55]. Because of its comparatively low β ,
 1176 the ionization energy can be significantly greater than expected for SM particles
 1177 because the most-probable energy loss grows significantly as β decreases [55].
 1178 This large ionization can be measured through the time over threshold (ToT) read
 1179 out from the pixel detector as described in Section 7.1.1.2. Large ionization in
 1180 the inner detector is one of the major characteristic features of LLPs.

1181 Throughout the next few nanoseconds, the R-Hadron propagates through the
 1182 remainder of the inner detector. A charged R-Hadron will provide hits in each
 1183 of these systems as would any other charged particle, and can be reconstructed
 1184 as a track. The track reconstruction provides a measurement of its trajectory
 1185 and thus its momentum as described in Section 7.1. The large momentum is
 1186 another characteristic feature of massive particles produced at the LHC. **Note: At**
 1187 **this point I am failing to mention that the TRT provides a possible dE/dx**
 1188 **measurement, because no one uses it as far as I know.**

1189 As of roughly 20 ns, the R-Hadron enters the calorimeter where it interacts
 1190 hadronically with the material. Because of its large mass and momentum, the
 1191 R-Hadron does not typically stop in the calorimeter, but rather deposits a small
 1192 fraction of its energy through repeated interactions with nucleons. The proba-
 1193 bility of interaction between the gluino itself and a nucleon is low because the
 1194 cross section drops off with the inverse square of its mass, so the interactions are
 1195 primarily governed by the light constituents [56]. Each of these interactions can
 1196 potentially change that quark content and thus change the sign of the R-Hadron,
 1197 so that the charge at exit is typically uncorrelated with the charge at entry [54].
 1198 The total energy deposited in the calorimeters during the propagation is small
 1199 compared to the kinetic energy of the R-Hadron, around 20-40 GeV, so that
 1200 E/p is typically less than 0.1 [54].

1201 Then, 30 ns after the collision, it reaches the muon system, where it again
 1202 ionizes in the material if charged and can be reconstructed as a muon track. Be-
 1203 cause of the charge-flipping interactions in the calorimeter, this track may have
 1204 the opposite sign of the track reconstructed in the inner detector, or there may
 1205 be a track present when there was none in the inner detector and vice-versa. The
 1206 propagation time at the typically lower β results in a significant delay compared
 1207 to muons, and that delay can be assessed in terms of a time-of-flight measure-
 1208 ment. Because of the probability of charge-flip and late arrival, there is a signif-
 1209 icant chance that an R-Hadron which was produced with a charge will not be
 1210 identified as a muon. The long time-of-flight is another characteristic feature of
 1211 R-Hadrons which are reconstructed as muons.

1212 10.1.2 LIFETIME DEPENDENCE

1213 The above description assumed a lifetime long enough for the R-Hadron to exit
 1214 the detector, which through this search is referred to as “stable”, even though
 1215 the particle may decay after exiting the detector. There are several unique sig-
 1216 natures at shorter lifetimes where the R-Hadron decays in various parts of the
 1217 inner detector; these lifetimes are referred to as “metastable”.

1218 The shortest case where the R-Hadron is considered metastable is for life-
 1219 times around 0.01 ns, where the particle decays before reaching any of the de-
 1220 tector elements. Although the R-Hadrons are produced opposite each other in
 1221 the transverse plane, each R-Hadron decays to a jet and an [LSP](#). The [LSPs](#) are not
 1222 measured, so the produced jets can be significantly imbalanced in the transverse
 1223 plane which results in large missing energy. That missing energy can be used
 1224 to trigger candidate events, and provides the most efficient trigger option for
 1225 shorter lifetimes. Additionally, the precision of the tracking system allows the
 1226 displaced vertex of the R-Hadron decay to be reconstructed from the charged
 1227 particles in the jet. The distance of that vertex from the interaction point can
 1228 be used to distinguish R-Hadron decays from other processes. Figure 26 shows
 1229 a schematic diagram of an example R-Hadron event with such a lifetime. The
 1230 diagram is not to scale, but instead illustrates the detector interactions in the
 1231 pixel detector, calorimeters, and muon system. It includes a representation of
 1232 the charged R-Hadron and the neutral R-Hadron, as well as the [LSPs](#) and jets
 1233 (shown as charged hadrons) produced in the decay. Neutral hadrons may also
 1234 be produced in the decay but are not depicted. Previous searches on [ATLAS](#) have
 1235 used the displaced vertex to target [LLP](#) decays [57].

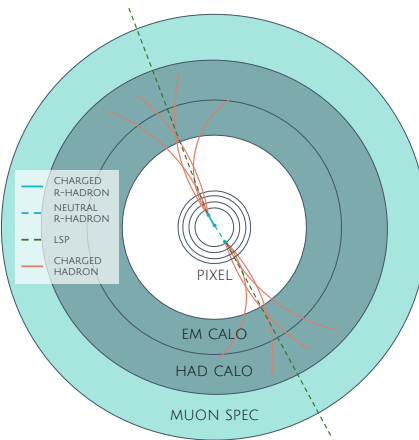


Figure 26: A schematic diagram of an R-Hadron event with a lifetime around 0.01 ns.
 The diagram includes one charged R-Hadron (solid blue), one neutral R-Hadron (dashed blue), [LSPs](#) (dashed green) and charged hadrons (solid orange).
 The pixel detector, calorimeters, and muon system are illustrated but not to scale.

1236 The next distinguishable case occurs at lifetimes greater than 0.1 ns, where
 1237 the R-Hadron forms a partial track in the inner detector. If the decay products
 1238 are sufficiently soft, they may not be reconstructed, and this forms a unique sig-

1239 nature of a disappearing track. An example of such an event is illustrated in
 1240 Figure 27, which shows the short track in the inner detector and the undetected
 1241 soft charged hadron and LSP that are produced. A dedicated search on ATLAS used
 1242 the disappearing track signature to search for LLP in Run 1 [58]. **zNote: might**
 1243 **not be worth mentioning the disappearing track here since it is actually a**
 1244 **chargino search, the soft pion is pretty unique to charginos.**

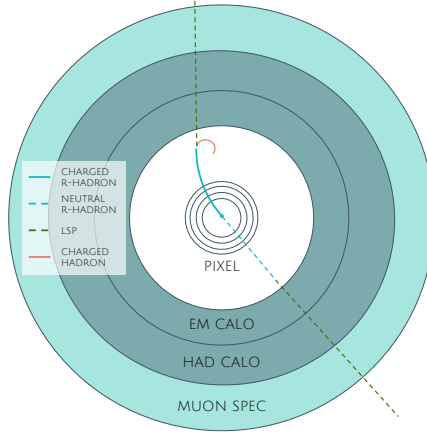


Figure 27: A schematic diagram of an R-Hadron event with a lifetime around 4 ns. The diagram includes one charged R-Hadron (solid blue), one neutral R-Hadron (dashed blue), LSPs (dashed green) and a charged hadron (solid orange). The pixel detector, calorimeters, and muon system are illustrated but not to scale.

1245 If the decay products are not soft, the R-Hadron daughters form jets, resulting
 1246 in an event-level signature of up to two high-momentum tracks, jets, and signif-
 1247 icant missing energy. The missing energy has the same origin as in the case of
 1248 0.01 ns lifetimes, from the decay to unmeasured particles, and again can be large.
 1249 The high-momentum tracks will also have the characteristically high-ionization
 1250 of massive, long-lived particles in the inner detector. Figure 28 illustrates an ex-
 1251 ample event with one charged R-Hadron which decays after approximately 10 ns,
 1252 and shows how the jets from the decay can still be reconstructed in the calorime-
 1253 ter. Several previous searches on ATLAS from Run 1 have used this signature to
 1254 search for R-Hadrons [59, 60], including a dedicated search for metastable parti-
 1255 cles [61].

1256 If the lifetime is longer than several nanoseconds, in the range of 15-30 ns,
 1257 the R-Hadron decay can occur in or after the calorimeters, but prior to reaching
 1258 the muon system. This case is similar to the above, although the jets may not be
 1259 reconstructed, and is covered by many of the same search strategies. The events
 1260 still often have large missing energy, although it is generated through different
 1261 mechanisms. The R-Hadrons do not deposit much energy in the calorimeters, so
 1262 a neutral R-Hadron will not enter into the missing energy calculation. A charged
 1263 R-Hadron opposite a neutral R-Hadron will thus generate significant missing en-
 1264 ergy, and close to 50% of pair-produced R-Hadron events fall into this category.
 1265 If both R-Hadrons are neutral then the missing energy will be low because nei-
 1266 ther is detected. Two charged R-Hadrons will also result in low missing energy
 1267 because both are reconstructed as tracks and will balance each other in the trans-

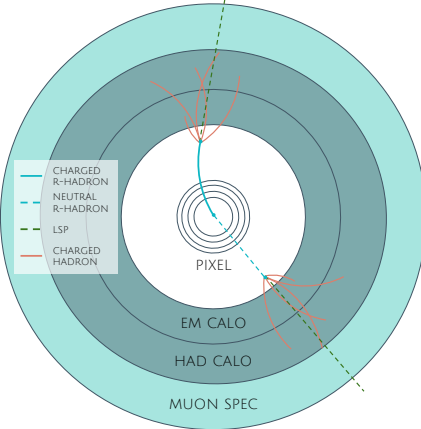


Figure 28: A schematic diagram of an R-Hadron event with a lifetime around 5 ns. The diagram includes one charged R-Hadron (solid blue), one neutral R-Hadron (dashed blue), LSPs (dashed green) and charged hadrons (solid orange). The pixel detector, calorimeters, and muon system are illustrated but not to scale.

1268 verse plane. A small fraction of the time, one of the charged R-Hadron tracks may
 1269 fail quality requirements and thus be excluded from the missing energy calcula-
 1270 tion and again result in significant missing energy. Figure 29 illustrates another
 1271 example event with one charged R-Hadron which decays after approximately 20
 1272 ns, and shows how the jets from the decay might not be reconstructed.

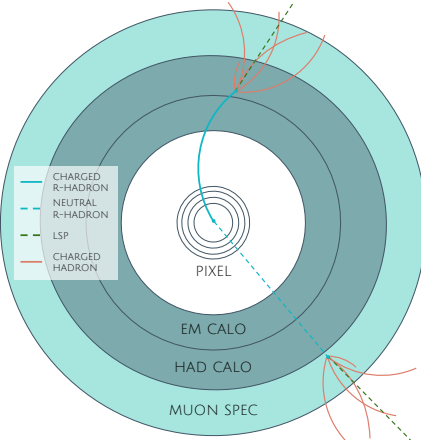


Figure 29: A schematic diagram of an R-Hadron event with a lifetime around 20 ns. The diagram includes one charged R-Hadron (solid blue), one neutral R-Hadron (dashed blue), LSPs (dashed green) and charged hadrons (solid orange). The pixel detector, calorimeters, and muon system are illustrated but not to scale.

1273 The longest lifetimes, the stable case, has all of the features of the 30-50 ns case
 1274 but with the addition of muon tracks for any R-Hadrons that exit the calorimeter
 1275 with a charge. That muon track can provide additional information from time-
 1276 of-flight measurements to help identify LSPs. An example of the event topology
 1277 for one charged and one neutral stable R-Hadron is shown in Figure 30. Some
 1278 searches on ATLAS have included this information to improve the search reach
 1279 for stable particles [60, 62].

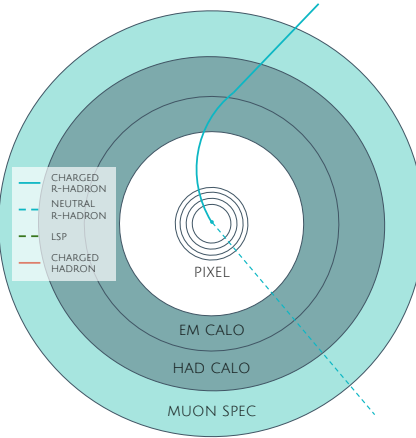


Figure 30: A schematic diagram of an R-Hadron event with a lifetime around 20 ns. The diagram includes one charged R-Hadron (solid blue) and one neutral R-Hadron (dashed blue). The pixel detector, calorimeters, and muon system are illustrated but not to scale.

1280 10.2 SIMULATION

1281 All of the event topologies discussed above are explored by simulations of R-
 1282 Hadron events in the [ATLAS](#) detector. A large number of such samples are gen-
 1283 erated to determine signal efficiencies, to measure expected yields, and to esti-
 1284 mate uncertainties. The primary interaction, pair production of gluinos with
 1285 masses between 400 and 3000 GeV, is simulated using [Pythia 6.4.27](#) [63]
 1286 with the AUET2B [64] set of tuned parameters for the underlying event and
 1287 the CTEQ6L1 [37] parton distribution function ([PDF](#)) set. The simulated inter-
 1288 actions include a modeling of pileup by adding secondary, minimum bias in-
 1289 teractions from both the same (in-time pileup) and nearby (out-of-time pileup)
 1290 bunch crossings. This event generation is then augmented with a dedicated
 1291 hadronization routine to hadronize the long-lived gluinos into final states with
 1292 R-Hadrons [65], with the probability to form a gluon-gluino bound set at 10% [66].

1293 The cross sections used for these processes are calculated at next-to-leading
 1294 order ([NLO](#)) in the strong coupling constant with a resummation of soft-gluon
 1295 emmission at next-to-leading logarithmic ([NLL](#)) [67–71]. The nominal predic-
 1296 tions and the uncertainties for each mass point are taken from an envelope of
 1297 cross-section predictions using different [PDF](#) sets and factorization and renor-
 1298 malization scales [72].

1299 The R-Hadrons then undergo a full detector simulation [], where the interac-
 1300 tions of the R-Hadrons with the material of the detector are described by dedi-
 1301 cated [Geant4](#) [7] routines. These routines model the interactions described in
 1302 Section 10.1.1, including the ionizing interactions in the silicon modules of the
 1303 inner detector and the R-Hadron-nucleon interactions in the calorimeters [73,
 1304 74]. The specific routine chosen to describe the interactions of the R-Hadrons
 1305 with nucleons, the “generic model”, uses a pragmatic approach where the scatter-
 1306 ing cross section is taken to be a constant 12 mb per light quark. In this model

1307 the gluino itself does not interact at all except through its role as a reservoir of
1308 kinetic energy.

1309 The lifetimes of these R-Hadrons are then simulated at several working points,
1310 $\tau = 0.1, 1.0, 3.0, 10, 30, 50$ and detector stable, where the particle is required to
1311 decay after propagating for a time compatible with its lifetime. Only one decay
1312 mode is simulated for these samples, $\tilde{g} \rightarrow q\bar{q}\tilde{\chi}_1^0$ with the neutralino mass set to
1313 100 GeV, which is chosen because it has the highest sensitivity among all of the
1314 modes studied in previous searches [61]. Heavier neutralinos have similar results
1315 but generate less missing energy which reduces the efficiency of triggering.

1316 All of the simulated events are then reconstructed using the same software
1317 used for collision data. The fully reconstructed events are then reweighted to
1318 match the distribution of initial state radiation in an alternative sample of events,
1319 generated with MG5_aMC@NLO [75], which has a more accurate description of ra-
1320 diate effects than Pythia6. This reweighting provides a more accurate descrip-
1321 tion of the momentum of the gluino-gluino system and is important in modeling
1322 the efficiency of triggering and offline event selection.

1323

1324 EVENT SELECTION

1325 The [LLPs](#) targeted by this search differ in their interactions with the detector from
 1326 [SM](#) particles primarily because of their large mass. When produced at the ener-
 1327 gies available at the [LHC](#), that large mass results in a low β (typically $0.2 < \beta <$
 1328 0.9). Such slow-moving particles heavily ionize in detector material. Each layer
 1329 of the pixel detector provides a measurement of that ionization, through [ToT](#), as
 1330 discussed in Section 6.3.1. The ionization in the pixel detector, quantified in
 1331 terms of dE/dx , provides the major focus for this search technique, along with
 1332 the momentum measured in the entire inner detector. It is effective both for its
 1333 discriminating power and its use in reconstructing a particle's mass, and it can
 1334 be used for a wide range of masses and lifetimes as discussed in Section 10.1.2.
 1335 However dE/dx needs to be augmented with a few additional selection require-
 1336 ments to provide a mechanism for triggering and to further reduce backgrounds.

1337 Ionization itself is not currently accessible for triggering, so this search in-
 1338 stead relies on E_T^{miss} to trigger signal events. Although triggering on E_T^{miss} can
 1339 be inefficient, E_T^{miss} is often large for many production mechanisms of [LLPs](#), as
 1340 discussed in Section 10.1.

1341 The use of ionization to reject [SM](#) backgrounds relies on well-measured, high-
 1342 momentum tracks, so some basic requirements on quality and kinematics are
 1343 placed on the tracks considered in this search. These quality requirements have
 1344 been significantly enhanced in Run 2 by a newly introduced tracking variable
 1345 that is very effective in removing highly-ionizing backgrounds caused by over-
 1346 lapping tracks. A few additional requirements are placed on the tracks consid-
 1347 ered for [LLP](#) candidates that increase background rejection by targeting specific
 1348 types of [SM](#) particles. These techniques provide a significant analysis improve-
 1349 ment over previous iterations of ionization-based searches on ATLAS by provid-
 1350 ing additional background rejection with minimal loss in signal efficiency.

1351 The ionization measurement with the Pixel detector can be calibrated to pro-
 1352 vide an estimator of $\beta\gamma$. That estimate, together with the momentum measure-
 1353 ment provided by tracking, can be used to reconstruct a mass for each track
 1354 which traverses the pixel detector. That mass variable will be peaked at the [LLP](#)
 1355 mass for any signal, and provides an additional tool to search for an excess. In
 1356 addition to an explicit requirement on ionization, this search constructs a mass-
 1357 window for each targeted signal mass in order to evaluate any excess of events
 1358 and to set limits.

1359 The strategy discussed here is optimized for lifetimes of $O(1) - O(10)$ ns.
 1360 Pixel ionization is especially useful in this regime as particles only need to prop-
 1361 agate through the first seven layers of the inner detector, about 37 cm from the
 1362 beam axis. The search is still competitive with other searches for [LLPs](#) at longer
 1363 lifetimes, because the primary discriminating variables are still applicable even
 1364 for particles that do not decay within the detector [62]. Although the majority of

1365 the requirements will be the same for all lifetimes, two signal regions are defined
 1366 to optimize separately for intermediate and long lifetime particles.

1367 11.1 TRIGGER

1368 Triggering remains a significant difficulty in defining an event selection with
 1369 high signal efficiency in a search for LLPs. There are no triggers available in
 1370 the current ATLAS system that can fire directly from a high momentum track
 1371 with large ionization (Section 6.6). Although in some configurations a charged
 1372 LLP can fire muon triggers, this requirement introduces significant model depen-
 1373 dence on both the allowed lifetimes and the interactions in the calorimeter [54],
 1374 as discussed in Section 10.1.1.

1375 For a search targeting particles which may decay prior to reaching the muon
 1376 system, the most efficient available trigger is based on missing energy [54]. As
 1377 discussed in Section 10.1, signal events can produce significant E_T^{miss} by a few
 1378 mechanisms. At the trigger level however, the missing energy is only calculated
 1379 using the calorimeters (Section 6.6) where the R-Hadrons deposit little energy.
 1380 So, at short lifetimes, E_T^{miss} measured in the calorimeter is generated by an im-
 1381 balance between the jets and undetected LSPs produced in R-Hadron decays. At
 1382 longer lifetimes, without the decay products, missing energy is only produced in
 1383 the calorimeters when the R-Hadrons recoil against an initial state radiation (ISR)
 1384 jet.

1385 These features are highlighted in Figure 31, which shows the E_T^{miss} distribu-
 1386 tions for simulated short lifetime (3 ns) and stable R-Hadron events. The figure
 1387 includes both the offline E_T^{miss} , the missing energy calculated with all available
 1388 information, and Calorimeter E_T^{miss} , the missing energy calculated using only
 1389 information available at the calorimeter which approximates the missing energy
 1390 available at the trigger. The short lifetime sample has significantly greater E_T^{miss}
 1391 and Calorimeter E_T^{miss} than the stable sample as expected. For the stable sam-
 1392 ple, a small fraction of events with very large E_T^{miss} (about 5%) migrate into the
 1393 bin with very small Calorimeter E_T^{miss} because the E_T^{miss} produced by a charged
 1394 R-Hadron track opposite a neutral R-Hadron track does not contribute any miss-
 1395 ing energy in the calorimeters.

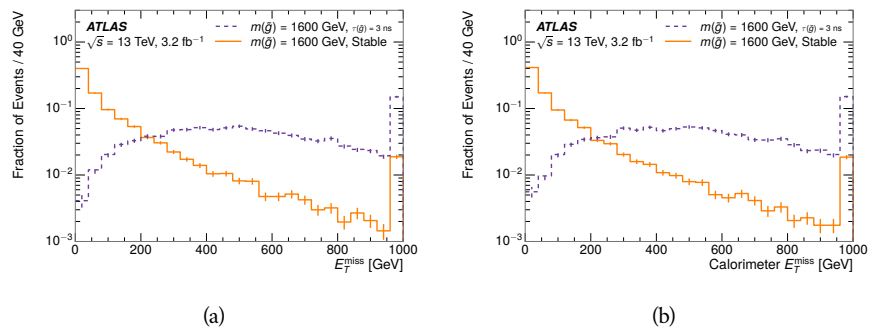


Figure 31: The distribution of (a) E_T^{miss} and (b) Calorimeter E_T^{miss} for simulated signal events before the trigger requirement.

1396 So, either case to some extent relies on kinematic degrees of freedom to pro-
 1397 duce missing energy, as the pair-produced LLPs tend to balance each other in
 1398 the transverse plain. That balance results in a relatively low efficiency for long-
 1399 lifetime particles, roughly 40%, and efficiencies between 65% and 95% for shorter
 1400 lifetimes depending on both the mass and the lifetime. For long lifetimes in par-
 1401 ticular, the presence of ISR is important in providing an imbalance in the trans-
 1402 verse plane, and is an important aspect of modeling the selection efficiency for
 1403 R-Hadron events.

1404 The missing energy trigger with the lowest threshold available is chosen for
 1405 this selection in order to maximize the trigger efficiency. During 2015 data col-
 1406 lection this was the HLT_xe70 trigger, which used a 50 GeV threshold on miss-
 1407 ing energy at LVL1 and a 70 GeV threshold on missing energy at the HLT. These
 1408 formation of the trigger decision for missing energy was discussed in more detail
 1409 in Section 6.6.

1410 11.2 KINEMATICS AND ISOLATION

1411 After the trigger requirement, each event is required to have a primary vertex
 1412 reconstructed from at least two well-measured tracks in the inner detector, each
 1413 with $p_T > 400$ MeV. If more than one such vertex exists, the primary vertex
 1414 is taken to be the one with the largest summed track momentum for all tracks
 1415 associated to that vertex. The offline reconstructed E_T^{miss} is required to be above
 1416 130 GeV to additionally reject SM backgrounds. The transverse missing energy
 1417 is calculated using fully reconstructed and calibrated offline objects, as described
 1418 in Section 7.5. In particular the E_T^{miss} definition in this selection uses jets recon-
 1419 structed with the anti- k_t algorithm with radius $R = 0.4$ from clusters of energy
 1420 in the calorimeter (Section 7.2) and with $p_T > 20$ GeV, as well as reconstructed
 1421 muons, electrons, and tracks not identified as another object type.

1422 The E_T^{miss} distributions are shown for data and a few simulated signals in Fig-
 1423 ure 32, after the trigger requirement. The cut placed at 130 GeV is 95% effi-
 1424 cient for metastable and 90% efficient for stable particles, after the trigger re-
 1425 quirement, because of the missing energy generating mechanisms discussed pre-
 1426 viously. The distribution of data in this figure and subsequent figures in this sec-
 1427 tion can be interpreted as the distribution of backgrounds, as any signal contam-
 1428 ination would be negligible if present at these early stages of the selection (prior
 1429 to the final requirement on ionization). The background falls rapidly with miss-
 1430 ing energy, motivating the direct requirement on E_T^{miss} for the signal region. Al-
 1431 though a tighter requirement than the specified value of 130 GeV would seem to
 1432 increase the search potential from these early distributions, other requirements
 1433 are more optimal when taken as a whole. The specific values for each require-
 1434 ment in signal region were optimized considering the increase in discovery reach
 1435 for tightening the requirement on each discriminating variable. **NOTE: If space**
1436 and time permit, I will add a whole section about signal region optimiza-
1437 tion..

1438 It is typically the practice for searches for new physics on ATLAS to place an
 1439 offline requirement on the triggering variable that is sufficiently tight to guar-

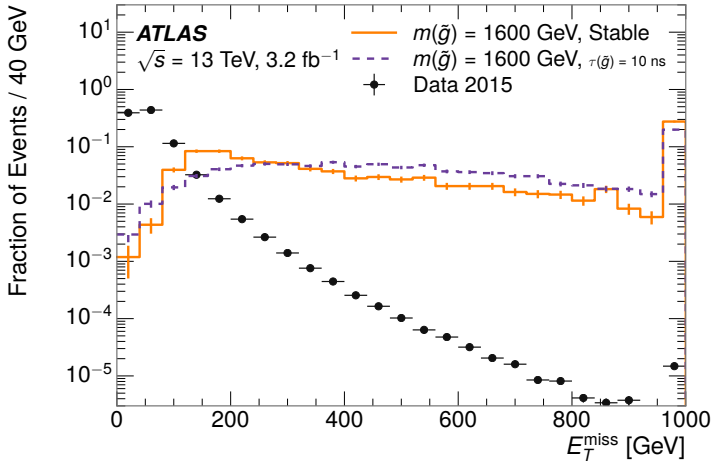


Figure 32: The distribution of E_T^{miss} for data and simulated signal events, after the trigger requirement.

1440 antee that the event would pass the trigger. Such a tight requirement makes the
 1441 uncertainty on the trigger efficiency of the simulation negligible, as modeling the
 1442 regime where the trigger is only partially efficient can be difficult. In this analy-
 1443 sis, however, because of the atypical interactions of R-Hadrons with the tracker
 1444 and the calorimeter, the offline requirement on E_T^{miss} is not sufficient to guar-
 1445 antee a 100% trigger efficiency even at large values, as can be seen in Figure 33.
 1446 This figure shows the efficiency for passing the HLT_xe70 trigger as a function
 1447 of the requirement on E_T^{miss} , which plateaus to roughly 85% even at large values.
 1448 This plateau does not reach 100% because events which have large offline miss-
 1449 ing energy from a neutral R-Hadron produced opposite of a charged R-Hadron
 1450 can have low missing energy in the calorimeters. The Calorimeter E_T^{miss} , on the
 1451 other hand, does not have this effect and reaches 100% efficiency at large values
 1452 because it is the quantity that directly corresponds to the trigger threshold. In
 1453 both cases the efficiency of triggering is greater for the short lifetime sample be-
 1454 cause the late decays to hadrons and LSPs produce an imbalance in the calorime-
 1455 ters even though they may not be reconstructed offline as tracks or jets. For this
 1456 reason, the requirement on E_T^{miss} is determined by optimizing the background
 1457 rejection even though it corresponds to a value of trigger efficiency significantly
 1458 below 1.0.

1459 Potential signal events are then required to have at least one candidate LLP
 1460 track. Although the LLPs are produced in pairs, many models do not consistently
 1461 yield two charged particles. For example, in the R-Hadron model highlighted
 1462 here, only 20% of events have two charged R-Hadrons while 47% of events have
 1463 just one. A signal region requiring two charged candidates could be a powerful
 1464 improvement in background rejection for a larger dataset, but it is not consid-
 1465 ered in this version of the analysis as it was found to be unnecessary to reject the
 1466 majority of backgrounds.

1467 For a track to be selected as a candidate, it must have $p_T > 50 \text{ GeV}$ and pass
 1468 basic quality requirements. The track must be associated to the primary vertex.

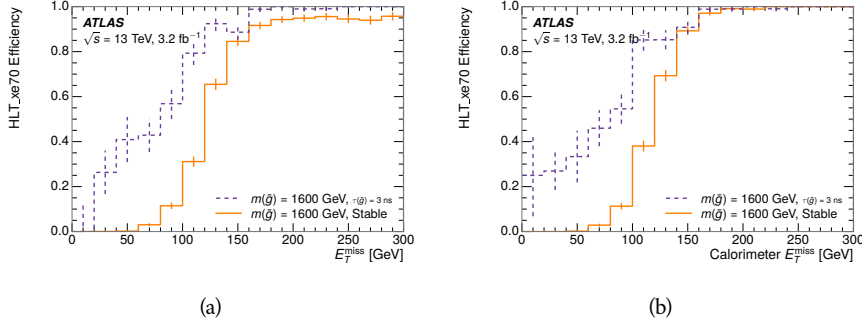


Figure 33: The trigger efficiency for the HLT_xe70 trigger requirement as a function of (a) E_T^{miss} and (b) Calorimeter E_T^{miss} for simulated signal events.

1469 It must also have at least seven clusters in the silicon layers in the inner detector
 1470 to ensure an accurate measurement of momentum. Those clusters must include
 1471 one in the innermost layer if the extrapolated track is expected to pass through
 1472 that layer. And to ensure a reliable measurement of ionization, the track is re-
 1473 quired to have at least two clusters in the pixel detector that provide a measure-
 1474 ment of dE/dx .

1475 At this point in the selection, there is a significant high-ionization background
 1476 from multiple tracks that significantly overlap in the inner detector. Previous
 1477 version of this analysis have rejected these overlaps by an explicit overlap rejec-
 1478 tion between pairs of fully reconstructed tracks, typically by requiring no addi-
 1479 tional tracks within a cone around the candidate. This technique, however, fails
 1480 to remove the background from tracks that overlap so precisely that the tracks
 1481 cannot be separately resolved, which can be produced in very collimated photon
 1482 conversions or decays of pions.

1483 A new method, added in Run 2, identifies cluster shapes that are likely formed
 1484 by multiple particles based on a neural network classification algorithm. The
 1485 number of clusters that are classified this way in the pixel detector for a given
 1486 track is called N_{split} . As the shape of clusters requires significantly less spatial
 1487 separation to identify overlaps than it does to reconstruct two fully resolved
 1488 tracks, this variable is more effective at rejecting backgrounds from overlaps.
 1489 Figure 34 shows the dependence of ionization on N_{split} ; as N_{split} increases the
 1490 most probable value of dE/dx grows significantly up to twice the expected value
 1491 when $N_{\text{split}} = 4$.

1492 This requirement is very successful in reducing the long positive tail of the
 1493 dE/dx distributions, as can be seen in Figure 35. Comparing the distribution
 1494 for “baseline tracks”, tracks with only the above requirements on clusters ap-
 1495 plied and before the requirement on N_{split} , to the distribution with $N_{\text{split}} = 0$,
 1496 it is clear that the fraction of tracks with large dE/dx is reduced be several or-
 1497 ders of magnitude. The tracks without split hits are very close to the dE/dx
 1498 distribution of identified muons, which are extremely well isolated on average.
 1499 Figure 35 also includes the distribution of dE/dx in an example signal simula-
 1500 tion to demonstrate how effective dE/dx is as a discriminating variable with this
 1501 isolation applied. The background falls rapidly for $dE/dx > 1.8 \text{ MeVg}^{-1}\text{cm}^2$

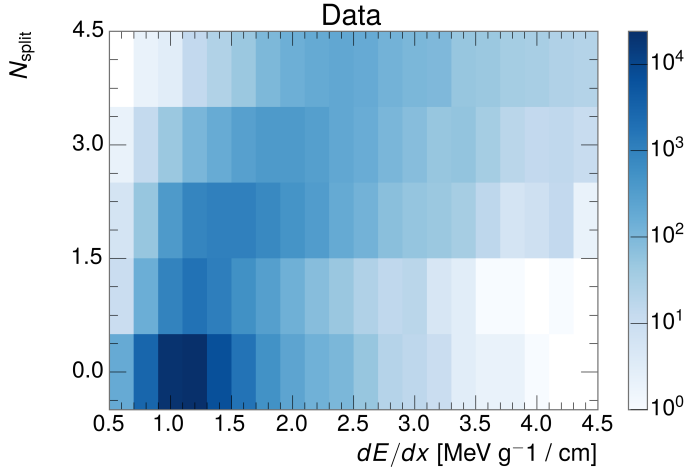


Figure 34: The dependence of dE/dx on N_{split} in data after basic track hit requirements have been applied.

1502 while the majority of the signal, approximately 90% depending on the mass, falls
 1503 above that threshold. Over 90% of LLP tracks in simulated signal events pass the
 1504 N_{split} -based isolation requirement.

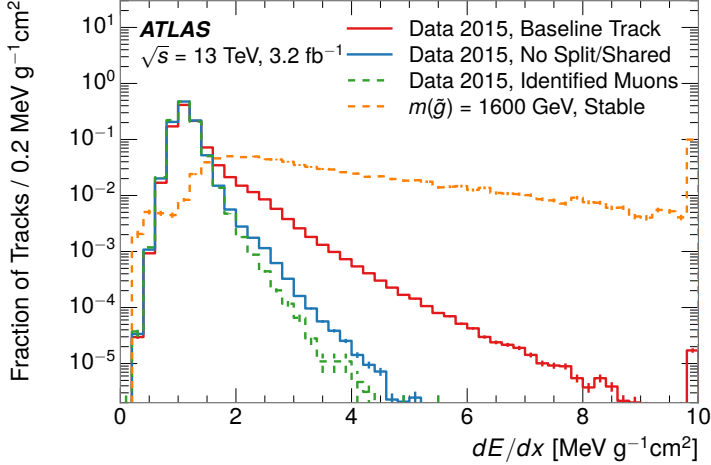


Figure 35: The distribution of dE/dx with various selections applied in data and simulated signal events.

1505 A few additional kinematic requirements are imposed to help reduce SM back-
 1506 grounds. The momentum of the candidate track must be at least 150 GeV, and
 1507 the uncertainty on that measurement must be less than 50%. The distribution of
 1508 momentum is shown in Figure 36 for tracks in data and simulated signal events
 1509 after the previously discussed requirements on clusters, transverse momentum,
 1510 and isolation have been imposed. The signal particles are much harder on aver-

age than their backgrounds because of the high energy interactions required to produce them. The transverse mass, M_T , defined as

$$M_T = \sqrt{2p_T E_T^{\text{miss}}(1 - \cos(\Delta\phi(E_T^{\text{miss}}, \text{track})))} \quad (1)$$

estimates the mass of a decay of to a single charged particle and an undetected particle and is required to be greater than 130 GeV to reject contributions from the decay of W bosons. Figure 37 shows the distribution of M_T for data and simulated signal events. The signal is distributed over a wide range of M_T , with about 90% above the threshold value of 130 GeV. The data shows a dual-peaked structure, where the first peak comes from W boson decays and the second peak is a kinematic shaping from the requirements on E_T^{miss} and the track p_T in dijet events.

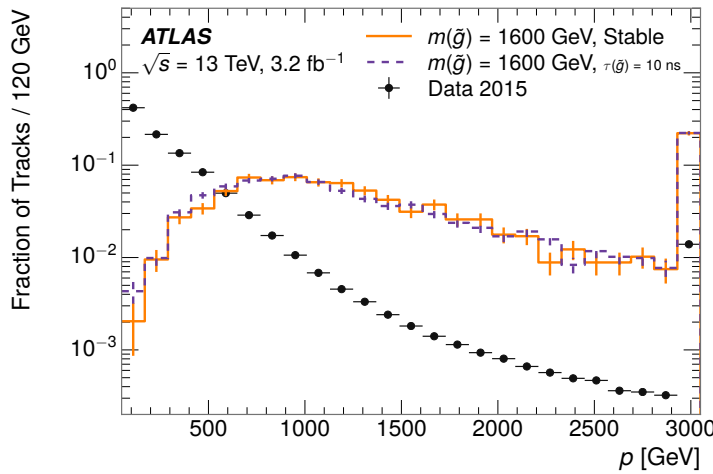


Figure 36: The distribution of track momentum for data and simulated signal events, after previous selection requirements have been applied.

11.3 PARTICLE SPECIES REJECTION

The amount of ionization deposited by particles with low mass and high momentum has a large positive tail [55], so backgrounds can be formed by a wide variety of SM processes when various charged particles have a few randomly large deposits of energy in the pixel detector. Those backgrounds can be additionally reduced by targeting other interactions with the detector where they are expected to have different behavior than R-Hadrons. The interactions with the detector depend on the types of particles produced rather than the processes which produce them, so this search forms a series of rejections to remove backgrounds from individual particle species. These rejections focus on using additional features of the event, other than the kinematics of the candidate track, as they can provide a powerful source of background rejection with very high signal efficiency. However, the lifetime of an R-Hadron can significantly change its

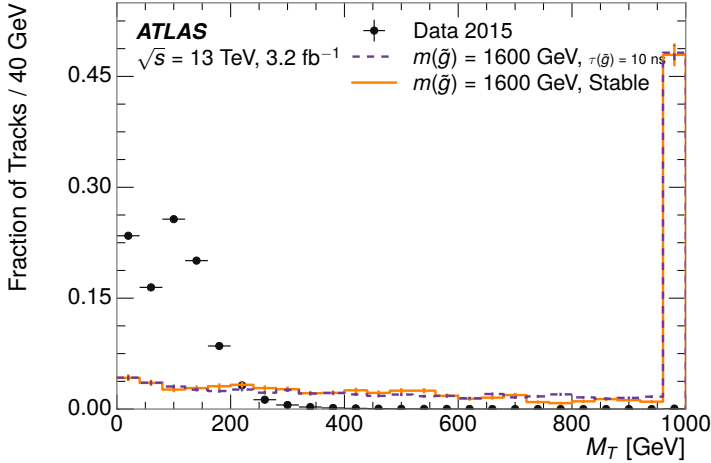


Figure 37: The distribution of M_T for data and simulated signal events, after previous selection requirements have been applied.

1534 detector characteristics, as discussed in Section 10.1.2. To accommodate these
 1535 differences, the SM rejections defined in this section are split to form two signal
 1536 regions, one for long-lifetimes particles, the stable region ($50 \leq \tau[\text{ns}] < \infty \text{ ns}$),
 1537 and one for intermediate lifetime particles, the metastable region ($0.4 < \tau[\text{ns}] <$
 1538 50).

1539 Jets can be very effectively rejected by considering the larger-scale isolation of
 1540 the candidate track. In this case the isolation focuses on the production of nearby
 1541 particles as a jet-veto, rather than the isolation from overlapping tracks based on
 1542 N_{split} that was used to reduce high-ionization backgrounds. As explained in Sec-
 1543 tion 10.1, the fragmentation process which produces an R-Hadron is very hard
 1544 and thus is not expected to produce additional particles with a summed momen-
 1545 tum of more than 5 GeV. The jet-veto uses the summed momentum of tracks
 1546 with a cone of $\Delta R < 0.25$, referred to as p_T^{Cone} , which is shown in Figure 38 for
 1547 data and simulated signal events. In the data this value has a peak at zero from
 1548 isolated tracks such as leptons, and a long tail from jets which contains as much
 1549 as 80% of the background above 20 GeV at this stage of the selection. In signal
 1550 events p_T^{Cone} is strongly peaked at zero and significantly less than 1% of signal
 1551 events have p_T^{Cone} above 20 GeV. This makes a requirement of $p_T^{\text{Cone}} < 20 \text{ GeV}$
 1552 a very effective method to reject background without losing signal efficiency.
 1553 For the stable signal region, this cut is further tightened to $p_T^{\text{Cone}} < 5 \text{ GeV}$ as
 1554 it is the most effective variable remaining to extend the search reach for long
 1555 lifetimes.

1556 Even for fully isolated particles, there are additional methods to reject each
 1557 type of particle using information in the muon system and calorimeters. Muons
 1558 can be identified very reliably using the tracks in the muon system, as described
 1559 in Section 7.4. For intermediate lifetimes the LLPs do not survive long enough
 1560 to reach the muon system, and so muons are vetoed by rejecting tracks that as-
 1561 sociate to a muon with medium muon identification requirements (Section 7.4).
 1562 For longer lifetimes, this rejection is not applied because LLPs which reach the

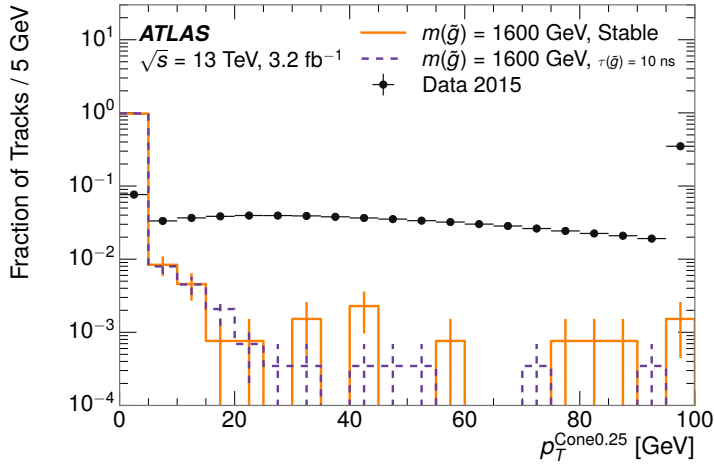


Figure 38: The distribution of summed tracked momentum within a cone of $\Delta R < 0.25$ around the candidate track for data and simulated signal events, after previous selection requirements have been applied.

muon system can be identified as muons as often as 30% of the time in simulated samples.

Calorimeter-based particle rejection relies on the expected small deposits of energy from LLPs. When the lifetime is long enough to reach the calorimeter, a LLP deposits little of its energy as it traverses the material, as discussed in Section 10.1. Even when the particle does decay before the calorimeter, the majority of its energy is carried away by the LSP and not deposited in the calorimeter. In both cases the energy is expected to be distributed across the layers of the calorimeters and not peaked in just one layer. This can be quantified in terms of E/p , the ratio of calorimeter energy of a nearby jet to the track momentum, and f_{EM} , the fraction of energy in that jet within the electromagnetic calorimeter. When no jets fall within a cone of 0.05 of the particle, E/p and f_{EM} are both defined as zero. E/p is expected to be above 1.0 for typical SM particles because of calibration and the contributions from other nearby particles, as discussed in Chapter ???. At these momenta there is no significant zero fraction due to interactions with the detector or insufficient energy deposits (see Section 8.2.2). f_{EM} is peaked close to 1.0 for electrons, and distributed between 10% and 90% for hadrons.

These trends can be seen in the two dimensional distribution for signal in Figure 39 for stable and metastable (10 ns) events. The majority of R-Hadrons in both samples fall into the bin for $E/p = 0$ and $f_{\text{EM}} = 0$ because the majority of the time there is no associated jet. In the stable sample, when there often is an associated jet, E/p is typically still below 0.1, and the f_{EM} is predominantly under 0.8. In the metastable sample, on the other hand, E/p is larger but still typically below 0.1 because of actual jets produced during the decay. The f_{EM} is much lower on average in this case, below 0.1, because the 10 ns lifetime particles rarely decay before passing through the electromagnetic calorimeter. Figure 39 also includes simulated Z decays to electrons or tau leptons. From the decays

1591 to electrons it is clear that the majority of electrons have f_{EM} above 0.9. The
 1592 tau decays include a variety of products. Muons can be seen in the bin where
 1593 $E/p = 0$ and $f_{\text{EM}} = 0$ because they do not have an associated jet. Electrons fall
 1594 into the range where $E/p > 1$ and $f_{\text{EM}} > 0.9$. Hadronic tau decays are the most
 1595 common, and fall in the range of $0.1 < f_{\text{EM}} < 0.9$ and $E/p > 1.0$.

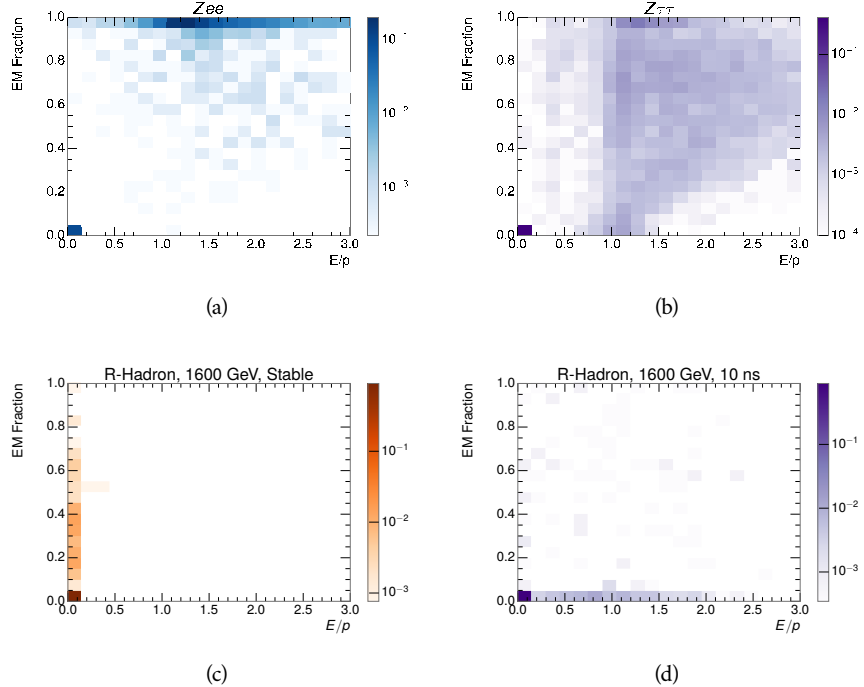


Figure 39: The normalized, two-dimensional distribution of E/p and f_{EM} for simulated
 (a) $Z \rightarrow ee$, (b) $Z \rightarrow \tau\tau$, (c) 1200 GeV Stable R-Hadron events, and (d) 1200
 GeV, 10 ns R-Hadron events.

1596 These differences motivate an electron rejection by requiring an f_{EM} below
 1597 0.9. Similarly, isolated hadrons are rejected by requiring $E/p < 1.0$. These re-
 1598 quirements combine to remove the majority of isolated electrons and hadrons
 1599 but retain over 95% of the simulated signal across a range of masses and lifetimes.

1600 11.4 IONIZATION

1601 The final requirement on the candidate track is the primary discriminating vari-
 1602 able, the ionization in the pixel detector. That ionization is measured in terms
 1603 of dE/dx , which was shown for data and simulated signal events in Figure 35.
 1604 dE/dx is dramatically greater for the high mass signal particles than the back-
 1605 grounds, which start to fall immediately after the minimally ionizing peak at 1.1
 1606 $\text{MeV g}^{-1} \text{cm}^2$. The dE/dx for candidate tracks must be greater than a pseudorapidity-
 1607 dependent threshold, specifically $1.80 - 0.11|\eta| + 0.17\eta^2 - 0.05\eta^3 \text{ MeV g}^{-1} \text{ cm}^{-2}$,
 1608 in order to correct for an approximately 5% dependence of the MIP peak on η .
 1609 The requirement was chosen as part of the signal region optimization, and man-

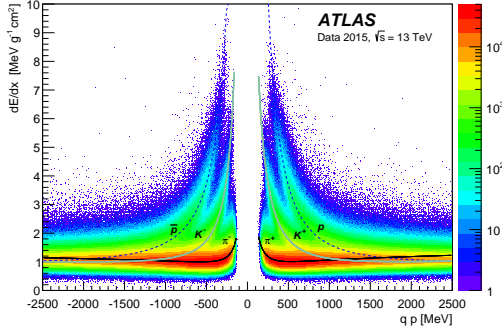


Figure 40: Two-dimensional distribution of dE/dx versus charge signed momentum (qp) for minimum-bias tracks. The fitted distributions of the most probable values for pions, kaons and protons are superimposed.

ages to reduce the backgrounds by a factor of 100 while remaining 70-90% efficient for simulated signal events depending on the mass.

11.4.1 MASS ESTIMATION

The mean value of ionization in silicon is governed by the Bethe equation and the most probable value follows a Landau-Vavilov distribution [55]. Those forms inspire a parametric description of dE/dx in terms of $\beta\gamma$,

$$(dE/dx)_{MPV}(\beta\gamma) = \frac{p_1}{\beta^{p_3}} \ln(1 + [p_2 \beta\gamma]^{p_5}) - p_4 \quad (2)$$

which performs well in the range $0.3 < \beta\gamma < 1.5$. This range includes the expected range of $\beta\gamma$ for the particles targeted for this search, with $\beta\gamma \approx 2.0$ for lower mass particles ($O(100 \text{ GeV})$) and up to $\beta\gamma \approx 0.5$ for higher mass particles ($O(1000 \text{ GeV})$). The parameters, p_i , are fit using a 2015 data sample of low-momentum pions, kaons, and protons as described in Ref. [76]. Figure 40 shows the two-dimensional distribution of dE/dx and momentum along with the above fitted values for $(dE/dx)_{MPV}$.

The above equation (2) is then numerically inverted to estimate $\beta\gamma$ and the mass for each candidate track. In simulated signal events, the mean of this mass value reproduces the generated mass up to around 1800 GeV to within 3%, and 3% shift is applied to correct for this difference. The mass distributions prior to this correction are shown for a few stable mass points in Figure 41. The large widths of these distributions come from the high variability in energy deposits in the pixel detector as well as the uncertainty on momentum measurements at high momentum, but the means converge to the expected values.

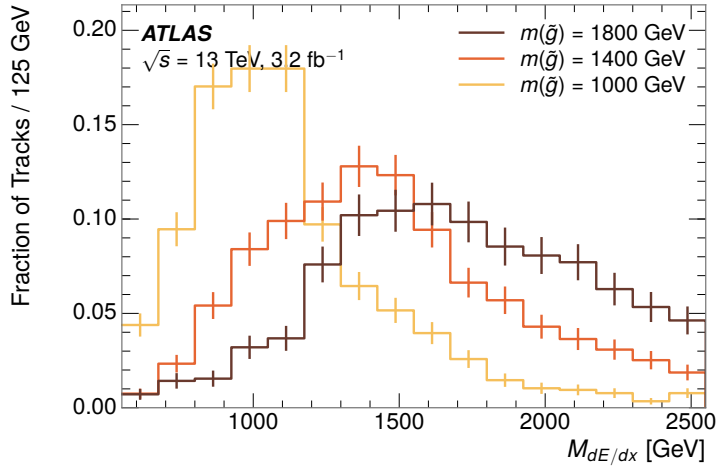


Figure 41: The distribution of mass estimated using dE/dx for simulated stable R-Hadrons with masses between 1000 and 1600 GeV.

1631 This analysis evaluates expected yields and the resulting cross sectional limits
 1632 using windows in this mass variable. The windows are formed by fitting mass
 1633 distributions in simulated signal events like those in Figure 41 to Gaussian distri-
 1634 butions and taking all events that fall within $\pm 1.4\sigma$ of the mean. As can be seen
 1635 in Figure 41, typical values for this width are $\sigma \approx 300 - 500$ GeV depending on
 1636 the generated mass.

1637 11.5 EFFICIENCY

1638 The numbers of events passing each requirement through ionization are shown
 1639 in Table 2 for the full 2015 dataset and a simulated 1600 GeV, 10 ns lifetime R-
 1640 Hadron sample. The table highlights the overall acceptance \times efficiency for sig-
 1641 nal events, which for this example is 19%. Between SM rejection and ionization,
 1642 this signal region reduces the background of tracks which pass the kinematic
 1643 requirements down by an additional factor of almost 2000.

1644 There is a strong dependence of this efficiency on lifetime and mass, with effi-
 1645 ciencies dropping to under 1% at low lifetimes. Figure 42 shows the dependence
 1646 on both mass and lifetime for all signal samples considered in this search. The
 1647 dependence on mass is relatively slight and comes predominantly from the in-
 1648 creasing fraction of R-Hadrons which pass the ionization cut with increasing
 1649 mass. The trigger and E_T^{miss} requirements are most efficient for particles that
 1650 decay before reaching the calorimeters. However, the chance of a particle to be
 1651 reconstructed as a high-quality track decreases significantly at low lifetimes as
 1652 the particle does not propagate sufficiently through the inner detector. These
 1653 effects lead to a maximum in the selection efficiency for lifetimes around 10-30
 1654 ns.

1655 The inefficiency of this signal region at short lifetimes comes almost exclu-
 1656 sively from an acceptance effect, in that the particles do not reach the necessary

Selection	Exp. Signal Events	Observed Events in 3.2 fb^{-1}
Generated	26.0 ± 0.3	
E_T^{miss} Trigger	24.8 ± 0.3 (95%)	
$E_T^{\text{miss}} > 130 \text{ GeV}$	23.9 ± 0.3 (92%)	
Track Quality and $p_T > 50$	10.7 ± 0.2 (41%)	368324
Isolation Requirement	9.0 ± 0.2 (35%)	108079
Track $p > 150 \text{ GeV}$	6.6 ± 0.2 (25%)	47463
$M_T > 130 \text{ GeV}$	5.8 ± 0.2 (22%)	18746
Electron and Hadron Veto	5.5 ± 0.2 (21%)	3612
Muon Veto	5.5 ± 0.2 (21%)	1668
Ionization Requirement	5.0 ± 0.1 (19%)	11

Table 2: The expected number of events at each level of the selection for metastable $1600 \text{ GeV}, 10 \text{ ns}$ R-Hadrons, along with the number of events observed in data, for 3.2 fb^{-1} . The simulated yields are shown with statistical uncertainties only. The total efficiency \times acceptance is also shown for the signal.

1657 layers of the SCT. This can be seen more clearly by defining a fiducial region
 1658 which includes events with at least one R-Hadron that is produced with non-
 1659 zero charge, $p_T > 50 \text{ GeV}$, $p > 150 \text{ GeV}$, $|\eta| < 2.5$, and a decay distance greater
 1660 than 37 cm in the transverse plane. At short (1 ns) lifetimes, the acceptance into
 1661 this region is as low as 4%. Once this acceptance is accounted for, the selection
 1662 efficiency ranges from 25% at lifetimes of 1 ns up to 45% at lifetimes of 10 ns.

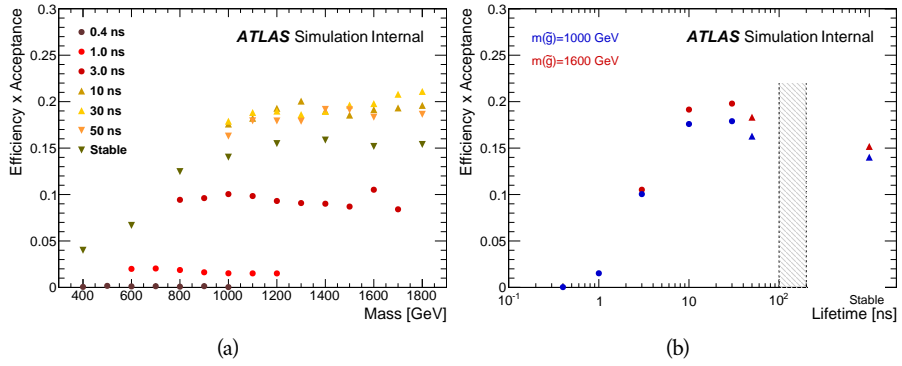


Figure 42: The acceptance \times efficiency as a function of R-Hadron (a) mass and (b) lifetime. (a) shows all of the combinations of mass and lifetime considered in this search, and (b) highlights the lifetime dependence for 1000 GeV and 1600 GeV R-Hadrons.

1663

1664 BACKGROUND ESTIMATION

1665 The event selection discussed in the previous section focuses on detector sig-
 1666 natures, emphasizing a single high-momentum, highly-ionizing track. That track
 1667 is then required to be in some way inconsistent with the expected properties
 1668 of SM particles, with various requirements designed to reject jets, hadrons,
 1669 electrons, and muons (Section 11.3). Therefore the background for this search comes
 1670 entirely from reducible backgrounds that are outliers of various distributions in-
 1671 cluding dE/dx , f_{EM} , and p_T^{Cone} . The simulation can be tuned in various ways to
 1672 do an excellent job of modeling the average properties of each particle type [77],
 1673 but it is not necessarily expected to accurately reproduce outliers. For this rea-
 1674 sons, the background estimation used for this search is estimated entirely using
 1675 data.

1676 12.1 BACKGROUND SOURCES

1677 SM charged particles with lifetimes long enough to form tracks in the inner de-
 1678 tector can be grouped into three major categories based on their detector inter-
 1679 actions: hadrons, electrons, and muons. Every particle that enters into the back-
 1680 ground for this search belongs to one of these types. Relatively pure samples of
 1681 tracks from each of these types can be formed in data by inverting the various
 1682 rejection techniques in Section 11.3. Specifically, muons are selected requiring
 1683 medium muon identification, electrons requiring $E/p > 1.0$ and $f_{EM} > 0.95$,
 1684 and hadrons requiring $E/p > 1.0$ and $f_{EM} < 0.95$.

1685 Figure 43 shows the distributions of momentum and dE/dx for these cate-
 1686 gories in data, after requiring the event level selection as well as the track re-
 1687 quirements on p_T , hits, and N_{split} , as discussed in Section 11.2. Simulated signal
 1688 events are included for reference. These distribution are only illustrative of the
 1689 differences between types, as the rejection requirements could alter their shape.
 1690 This is especially significant for momentum which enters directly into E/p and
 1691 can indirectly affect muon identification. However the various types show clear
 1692 differences in both distributions. The distributions of momentum are not nec-
 1693 cessarily expected to match between the various types because the production
 1694 mechanisms for each type result in different kinematic distributions. dE/dx is
 1695 also different between types because of incomplete isolation; although the re-
 1696 quirement on N_{split} helps to reduce the contribution of nearby particles it does
 1697 not completely remove the effect of overlaps. Muons are better isolated because
 1698 they do not have the additional particle from hadronization present for hadrons
 1699 and they are significantly less likely do interact with the detector and produce
 1700 secondary particles compared to hadrons and electrons. Thus muons have the
 1701 smallest fraction of dE/dx above the threshold of $1.8 \text{ MeVg}^{-1}\text{cm}^2$; hadrons and
 1702 electrons have a larger fraction above this threshold.

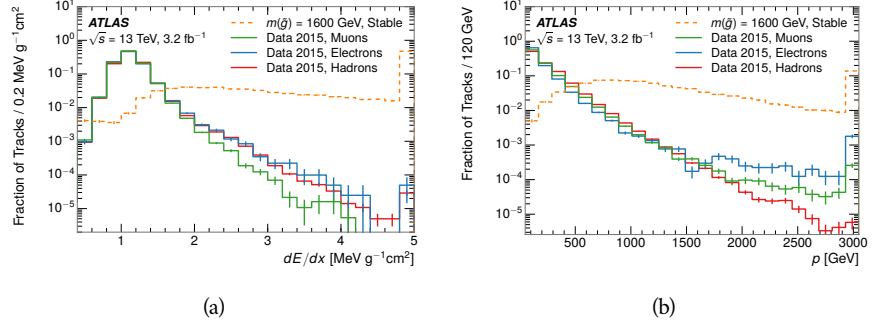


Figure 43: The distribution of (a) dE/dx and (b) momentum for tracks in data and simulated signal after requiring the event level selection and the track selection on p_T , hits, and N_{split} . Each sub-figure shows the normalized distributions for tracks classified as hadrons, electrons, and muons in data and R-Hadrons in the simulated signal.

1703 It is difficult to determine what fraction of each particle type enters into the fi-
1704 nal signal region. The background method will not have significant dependence
1705 on the relative contributions of each species, but it is useful to understand the
1706 differences between each when considering the various tests of the method.

1707 12.2 PREDICTION METHOD

The data-driven background estimation relies on the independence between ionization and other kinematic variables in the event. For standard model particles with momenta above 50 GeV, dE/dx is not correlated with momentum; though there is a slight relativistic rise as momentum increases, the effect is small compared to the width of the distribution of ionization energy deposits.. So, the proposed method to estimate the mass distribution of the signal region is to use momentum from a track with low dE/dx (below the threshold value) and to combine it with a random dE/dx value from a dE/dx template. The resulting track is just as likely as the original, so a number of such random generations provide the expected distributions of momentum and ionization. These are then combined using the parametrization described in Section 11.4.1 to form a distribution of mass for the signal region.

Algorithmically this method is implemented by forming two distinct Control Regions ([CRs](#)). The first [CR](#), CR1, is formed by applying the entire event selection from Chapter 11 up to the dE/dx and mass requirements. The dE/dx requirement is instead inverted for this region. Because of the independence of dE/dx , the tracks in this control region have the same kinematic distribution as the tracks in the signal region, and are used to measure a two-dimensional template of p and η . The second [CR](#), CR2, is formed from the event selection through the dE/dx requirement, but with an inverted E_T^{miss} requirement. The tracks in this control region are expected to have similar dE/dx distributions to the signal region before the ionization requirement, and so this region is used to measure a two-dimensional template of dE/dx and η .

1731 The contribution of any signal to the control regions is minimized by the in-
 1732 verted selection requirements. Only less than 10% of simulated signal events
 1733 have either dE/dx or E_T^{miss} below the threshold values in the original signal re-
 1734 gion, while the backgrounds are significantly enhanced by inverting those re-
 1735 quirements. The signal contamination is less than 1% in both control regions
 1736 for all of the simulated masses and lifetimes considered in this analysis.

1737 With those measured templates, the shape of the mass estimation is generated
 1738 by first selecting a random (p , η) combination from CR1. This momentum
 1739 value is combined with a dE/dx value taken from the appropriate distribution
 1740 of dE/dx for the selected η from CR2. The use of η in both random samplings
 1741 controls for any correlation between p , dE/dx , and η . Those values are then
 1742 used to calculate a mass in the same way that is done for regular tracks in data,
 1743 see Section 11.4.1. As this procedure includes all dE/dx values, the cut at 1.8
 1744 MeVg $^{-1}$ cm 2 is then enforced to fully model the signal region. The generated
 1745 mass distribution is then normalized by scaling the background estimate to the
 1746 data in the region $M < 160$ GeV, where signals of this type have already been
 1747 excluded [61]. This normalization uses the distributions of mass generated with-
 1748 out the ionization requirement.

1749 The statistical uncertainties on these background distributions are calculated
 1750 by independently fluctuating each bin of the input templates according to their
 1751 Poisson uncertainties. These fluctuations are repeated a large number of times,
 1752 and the uncertainty on the resulting distribution is taken as the root mean square
 1753 (RMS) deviation of the fluctuations from the average. As the procedure uses one
 1754 million random combinations to generate the distributions, The statistical un-
 1755 certainty from the actual random generations is negligible compared to the un-
 1756 certainty from measuring the templates.

1757 12.3 VALIDATION

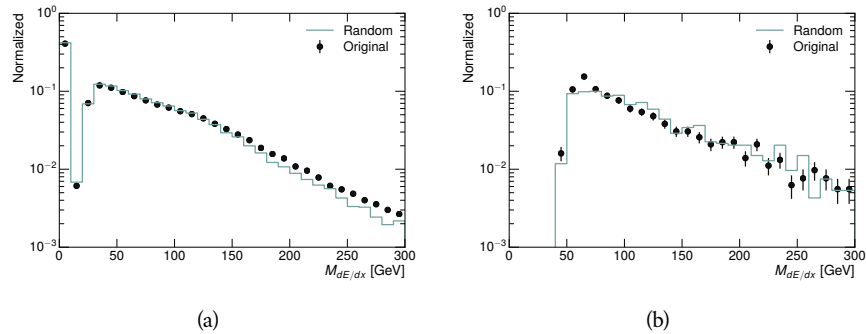
1758 The validity of the background estimation technique can be evaluated in both
 1759 data and simulation. The underlying assumption that random combinations of
 1760 dE/dx and momentum can predict a mass distribution in an orthogonal region
 1761 can be tested using simulated samples where concerns like multiple particle types
 1762 can be controlled. Using the same technique in another set of signal-depleted
 1763 regions in data then extends this confidence to the more complicated case where
 1764 several particle species are inherently included.

1765 12.3.1 CLOSURE IN SIMULATION

1766 The first test of the procedure is done using a simulated sample of $W \rightarrow \mu\nu$
 1767 decays. These types of events provide the ingredients required to test the back-
 1768 ground estimate, E_T^{miss} and isolated tracks, with high statistics. In this example
 1769 there is no signal, so simulated events in the orthogonal CRs are used to estimate
 1770 the shape of the mass distribution of the simulated events in the signal region. To
 1771 reflect the different topology for W boson decays, the CRs use slightly modified
 1772 definitions. In all CRs, the requirement of $p > 150$ GeV and the SM rejection

1773 requirements are removed. Additionally, for the signal region the requirement
 1774 on E_T^{miss} is relaxed to 30 GeV and the corresponding inverted requirement on
 1775 CR2 is also set at 30 GeV.

1776 With these modified selections, the simulated and randomly generated distri-
 1777 butions of $M_{dE/dx}$ are shown in Figure 44. This figure includes the mass distri-
 1778 butions before and after the requirement on dE/dx , which significantly shapes
 1779 the distributions. In both cases the background estimation technique repro-
 1780 duces the shape of $M_{dE/dx}$ in the signal region. There is a small difference in the pos-
 1781 itive tail of the mass distribution prior to the ionization cut, where the random
 1782 events underestimate the fraction of tracks with mass above 150 GeV by about
 1783 20%. After the ionization requirement, however, this discrepancy is not present
 1784 and the two distributions agree to within statistical uncertainties.



1785 Figure 44: The distribution of $M_{dE/dx}$ (a) before and (b) after the ionization requirement
 1786 for tracks in simulated W boson decays and for the randomly generated back-
 1787 ground estimate.

1788 This ability to reproduce the shape of the mass distribution in simulated events
 1789 shows that the technique works as expected. No significant biases are acquired
 1790 in using low dE/dx events to select kinematic templates or in using low E_T^{miss}
 1791 events to select ionization templates, as either would result in a mismodeling of
 1792 the shape of the mass distribution. The simulated events contain only one par-
 1793 ticle type, however, so this test only establishes that the technique works well
 1794 when the the CRs are populated by exactly the same species.

1795 12.3.2 VALIDATION REGION IN DATA

1796 The second test of the background estimate is performed using data in an or-
 1797 thogonal validation region. The validation region, and the corresponding CRs,
 1798 are formed using the same selection requirements as in the nominal method but
 1799 with a modified requirement on momentum, $50 < p[\text{GeV}] < 150$. This allows
 1800 the technique to be checked in a region with very similar properties but where
 1801 the signal is depleted, as the majority of the signal has momentum above 150
 1802 GeV while the backgrounds are enhanced below that threshold. Any biases on
 1803 the particle composition of the CRs for the signal region will be reflected in the
 1804 CRs used to estimate the mass distribution in the validation region.

Figure 45 shows the measured and randomly generated mass distributions for data before and after the ionization requirement. The background estimate does an excellent job of modeling the actual background before the ionization requirement, with good agreement to within the statistical uncertainties out to the limit of the mass distribution. There are very few events in the validation region after the ionization requirement, but the few observed events are consistent with the background prediction. The good agreement in this validation region provides a confirmation that the technique works even in the full-complexity case with multiple particle types entering the distributions. Any bias from changes in particle composition between regions is small compared to statistical uncertainties.

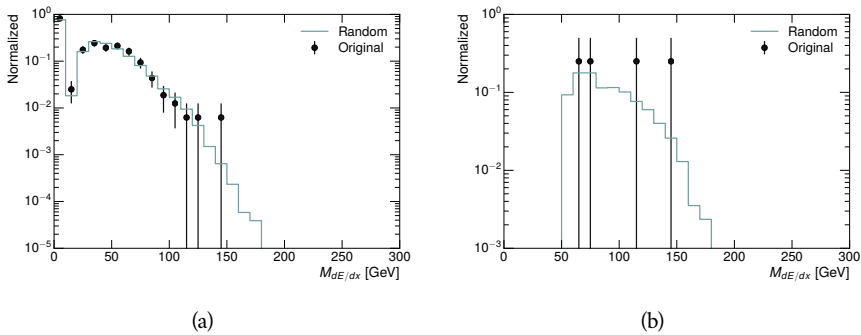


Figure 45: The distribution of $M_{dE/dx}$ (a) before and (b) after the ionization requirement for tracks in the validation region and for the randomly generated background estimate.

1812

1813 SYSTEMATIC UNCERTAINTIES AND RESULTS

1814 13.1 SYSTEMATIC UNCERTAINTIES

1815 A number of systematic uncertainties affect the interpretation of the results of
 1816 the search. These uncertainties can broken down into two major categories,
 1817 those which affect the estimate of the background using data and those which
 1818 affect the measurement of the signal yield estimated with simulated events. The
 1819 total measured systematic uncertainties are 7% for the background estimation
 1820 and approximately 32% for the signal yield depending on lifetime. These system-
 1821atic uncertainties are expected to be small compared to the statistical fluctuations
 1822 of the measured yields so that measured cross-sectional limits will be dominated
 1823 by statistical uncertainties. The following sections describe each source of sys-
 1824 tematic uncertainty for each of the two types.

1825 13.1.1 BACKGROUND ESTIMATE

1826 The systematic uncertainties on the background estimate come primarily from
 1827 considering alternative methods for generating the background distributions.
 1828 These uncertainties are small compared to the statistical uncertainties on the
 1829 background estimate which come from the limited statistics in measuring the
 1830 template distributions, as described in Section 12.2. They are summarized in
 1831 Table 3.

Source of Uncertainty:	Value [%]
Analytic Description of dE/dx	4.0
Muon Fraction (Stable Region only)	3.0
IBL Ionization Correction	3.8
Normalization	3.0
Total (Metastable Region):	6.3
Total (Stable Region):	7.0

Table 3: A summary of the sources of systematic uncertainty for the data-driven back-
 ground in the signal region. If the uncertainty depends on the mass, the maxi-
 mum values are reported.

1832 13.1.1.1 ANALYTIC DESCRIPTION OF DE/DX

1833 The background estimate uses a binned template distribution to estimate the
 1834 dE/dx of tracks in the signal region, as described in Section 12.2. It is also possi-

ble to fit that measured distribution to a functional form to help smooth the distribution in the tails of dE/dx where the template is driven by a small number of tracks. Both Landau convolved with a Gaussian and Crystal Ball functions are considered as the functional form and used to re-estimate the background distribution. The deviations compared to the nominal method are found to be 4%, and this is taken as a systematic uncertainty to cover the inability carefully predict the contribution from the long tail of dE/dx where there are few measurements available in data.

1843 13.1.1.2 MUON FRACTION

1844 The stable region of the analysis explicitly includes tracks identified as muons,
 1845 which have a known difference in their dE/dx distributions compared to non-
 1846 muon tracks (Section 12.1). To account for a difference in muon fraction be-
 1847 tween the background region and the signal region for this selection, the dE/dx
 1848 templates for muons and non-muons are measured separately and then the rel-
 1849 ative fraction of each is varied in the random generation. The muon fraction
 1850 is varied by its statistical uncertainty and the resulting difference of 3% in back-
 1851 ground yield is taken as the systematic uncertainty.

1852 13.1.1.3 IBL CORRECTIONS

1853 The Insertible B-Layer (IBL), described in Section 6.3.1, received a significant
 1854 dose of radiation during the data collection in 2015. The irradiation can cause
 1855 a drift in the frontend electronics and thus alter the dE/dx measurement which
 1856 includes the ToT output by the IBL. These effects are corrected for in the nominal
 1857 analysis by scaling the dE/dx measurements by a constant factor derived for
 1858 each run to match the average dE/dx value to a reference run where the IBL
 1859 was known to be stable to this effect. However, this corrective factor does not
 1860 account for inter-run variations. To account for this potential drift of dE/dx ,
 1861 the correction procedure is repeated by varying the corrections up and down by
 1862 the maximal run-to-run variation from the full data-taking period, which results
 1863 in an uncertainty of 3.8%.

1864 13.1.1.4 NORMALIZATION

1865 As described in Section 12.2, the generated distribution of masses is normalized
 1866 in a shoulder region ($M < 160$ GeV) where signals have been excluded by pre-
 1867 vious analyses. That normalization factor is varied by its statistical uncertainty
 1868 and the resulting fluctuation in the mass distribution of 3% is taken as a system-
 1869 atic uncertainty on the background estimate.

1870 13.1.2 SIGNAL YIELD

1871 The systematic uncertainties on the signal yield can be divided into three cate-
 1872 gories; those on the simulation process, those on the modeling of the detector
 1873 efficiency or calibration, and those affecting the overall signal yield. They are
 1874 summarized in Table 3. The largest uncertainty comes from the uncertainty on

1875 the production cross section for gluinos, which is the dominant systematic un-
 1876 certainty in this analysis.

Source of Uncertainty	-[%]	+[%]
ISR Modeling (Metastable Region)	1.5	1.5
ISR Modeling (Stable Region)	14	14
Pile-up Reweighting	1.1	1.1
Trigger Efficiency Reweighting	0.9	0.9
E_T^{miss} Scale	1.1	2.2
Ionization Parametrization	7.1	0
Momentum Parametrization	0.3	0.0
Electron Rejection	0.0	0.0
Hadron Rejection	0.0	0.0
μ Identification	4.3	4.3
Luminosity	5	5
Signal size uncertainty	28	28
Total (Metastable Region)	30	29
Total (Stable Region)	33	32

Table 4: A summary of the sources of systematic uncertainty for the simulated signal yield. The uncertainty depends on the mass and lifetime, and the maximum negative and positive values are reported in the table.

1877 13.1.2.1 ISR MODELING

1878 As discussed in Section 10.2, MadGraph is expected to reproduce the distribution
 1879 of ISR in signal events more accurately than the nominal Pythia samples. The
 1880 analysis reweights the distribution of ISR in the simulated signal events to match
 1881 the distribution found in generated MadGraph samples. This has an effect on the
 1882 selection efficiency in the signal samples, where ISR contributes to the generation
 1883 of E_T^{miss} . To account for the potential inaccuracy on the simulation of ISR at high
 1884 energies, half of the difference between the signal efficiency with the reweighted
 1885 distribution and the original distribution is taken as a systematic uncertainty.

1886 13.1.2.2 PILEUP REWEIGHTING

1887 The simulated events were generated prior to data collection with an estimate of
 1888 the average number of interactions per bunch crossing. This estimate does not
 1889 match the value of pileup during actual data collection, but a large fraction of the
 1890 simulated events would be discarded in order to match the distribution in data.
 1891 Therefore the simulated signal events are not reweighted for pileup by default
 1892 in the analysis. The effect of the pileup on signal efficiency is not expected to
 1893 depend on the mass or lifetime of the generated signal events, which allows all

of the generated signal events to be used together to assess the pileup dependence.
 To account for the potential effect of the difference in the number of interactions per bunch crossing between data and simulation, the difference in yield between the nominal signal events and the reweighted events averaged over all masses and lifetimes is taken as a systematic uncertainty on the yield for each mass and lifetime (1.1%).

13.1.2.3 TRIGGER EFFICIENCY REWEIGHTING

As described in Section 11.2, the selection for this analysis does not require a sufficiently large value of E_T^{miss} to be above the plateau of trigger efficiency. Therefore, some signal events which would otherwise pass the event selection can be excluded because of the trigger requirement. These effects can be difficult to estimate in simulation, and thus are constrained by comparing data and simulated events in an alternative W boson region which uses decays to muons to find a relatively pure sample of events with missing energy. The trigger efficiency for data and simulated W events are shown in Figure 46. The comparison between data and MC in this region constrains the simulation of the trigger efficiency. The simulated signal events are reweighted by the ratio of data to simulation in the W boson decays, while the difference between the data and simulation in those decays is taken as a systematic uncertainty. This results in an uncertainty of only 0.9% as the majority of events are well above the plateau and the disagreement between data and simulation is small even below that plateau.

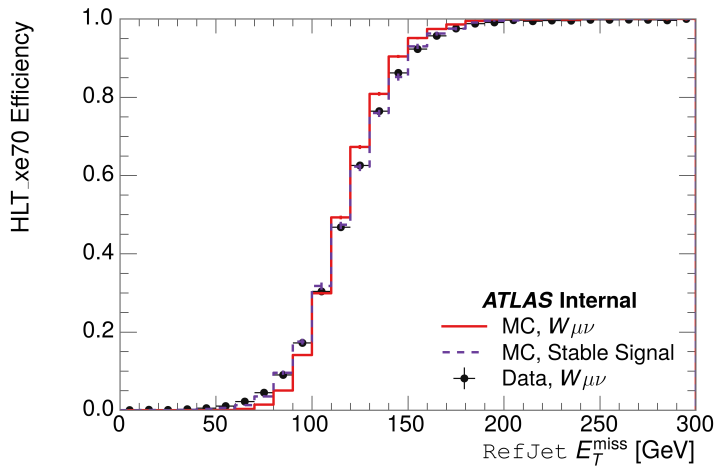


Figure 46: The trigger efficiency for the HLT_xe70 trigger requirement as a function of Calorimeter E_T^{miss} for simulated data events with a W boson selection. Simulated signal events and simulated W boson events are also included.

13.1.2.4 MISSING TRANSVERSE MOMENTUM SCALE

The ATLAS Combined Performance (CP) group provides a default recommendation for systematic variations of jets and missing energy (**note: I'm not quite sure what to cite for this - I don't see any papers from the jet/met group**

Systematic Variation	-[%]	+[%]
JET_GroupedNP_1	-0.7	1.3
JET_GroupedNP_2	-0.7	1.2
JET_GroupedNP_3	-0.5	1.3

Table 5: Example of the contributing systematic variations to the total systematic for the E_T^{miss} Scale, as measured in a 1200 GeV, Stable R-Hadron signal sample.

1919 **after this was implemented).** These variations enter into this analysis only in
 1920 the requirement on E_T^{miss} . The effect of the measured scale of E_T^{miss} is evaluated
 1921 by varying the E_T^{miss} scale according to the one sigma variations provided by all
 1922 **CP** recommendations on objects affecting event kinematics in simulated signal
 1923 events. Missing energy is reconstructed from fully reconstructed objects so any
 1924 systematic uncertainties affecting jets, muons, electrons, or the E_T^{miss} soft terms
 1925 are included. The only non-negligible contributions found using this method are
 1926 itemized in Table 5 for an example signal sample (1200 GeV, Stable R-Hadron),
 1927 where the systematic is measured as the relative difference in the final signal ef-
 1928 ficiency after applying the associated variation through the CP tools. The only
 1929 variations that are significant are the grouped jet systematic variations, which
 1930 combine recommended jet systematic uncertainties into linearly independent
 1931 variations.

1932 As the peak of the reconstructed E_T^{miss} distribution in the signal is significantly
 1933 above the current threshold for events which pass the trigger requirement, the
 1934 effect of scale variation is expected to be small, which is consistent with the mea-
 1935 sured systematic of approximately 2%. Events which do not pass the trigger re-
 1936 quirement usually fail because there are no ISR jets in the event to balance the
 1937 R -hadrons' transverse momentum, so the reconstructed E_T^{miss} is low and there-
 1938 fore also expected to be not very sensitive to scale changes.

1939 13.1.2.5 MOMENTUM PARAMETRIZATION

1940 The uncertainty on the signal efficiency from track momentum is calculated us-
 1941 ing the **CP** group recommendations for tracks. In particular, only one recom-
 1942 mended systematic variation affects track momentum, the sagitta bias for q/P .
 1943 This uncertainty is propagated to the final selection efficiency by varying the
 1944 track momentum by the recommended one sigma variation, and the associated
 1945 uncertainty is found to be negligible (0.3%).

1946 13.1.2.6 IONIZATION REQUIREMENT

1947 The dE/dx distributions in data and simulated events have different most prob-
 1948 able values, which is due in part to radiation effects in the detector that are not
 1949 fully accounted for in the simulation. The difference does not affect the mass
 1950 measurement used in this analysis, as independent calibrations are done in sim-
 1951 ulation and in data. However, it does affect the efficiency of the high dE/dx
 1952 selection requirement. To calculate the size of the effect on the signal efficiency,

1953 the dE/dx distribution in signal simulation is scaled by a scale factor obtained
 1954 from comparing the dE/dx distribution of inclusive tracks in data and in sim-
 1955 ulation. The difference in efficiency for this sample with a scaled dE/dx dis-
 1956 tribution, relative to the nominal case, is taken as a systematic uncertainty on
 1957 signal efficiency. The uncertainty is as large as 7% for low masses and falls to a
 1958 negligible effect for large masses.

1959 13.1.2.7 ELECTRON AND JET REJECTION

1960 The systematic uncertainty on the electron rejection is measured by varying the
 1961 EM fraction requirement significantly, from 0.95 to 0.9. This is found to have
 1962 a less than 0.04% effect on signal acceptance, on average, and so is completely
 1963 negligible. Similarly, the uncertainty on jet rejection is measured by tightening
 1964 the E/p requirement from 0.5 to 0.4. This is found to have no effect on signal
 1965 acceptance, so again the systematic is again negligible.

1966 13.1.2.8 MUON VETO

1967 The metastable signal region requires that the candidate tracks are not identi-
 1968 fied as medium muons because the majority of R-Hadrons in the lifetime range
 1969 included in that region do not reach the muon spectrometers before they de-
 1970 cay. However, the exponential tail of the R-Hadron lifetime distribution results
 1971 in some R-Hadrons traversing the muon spectrometer. These can still fail the
 1972 muon medium identification because they can fail on the requirement on the
 1973 number of precision hits required to pass the loose selection because they ar-
 1974 rive late to the muon spectrometer. This can be seen in Figure 47, which shows
 1975 the efficiency of the muon veto as a function of $1/\beta$, for two simulated stable
 1976 R-Hadron samples.

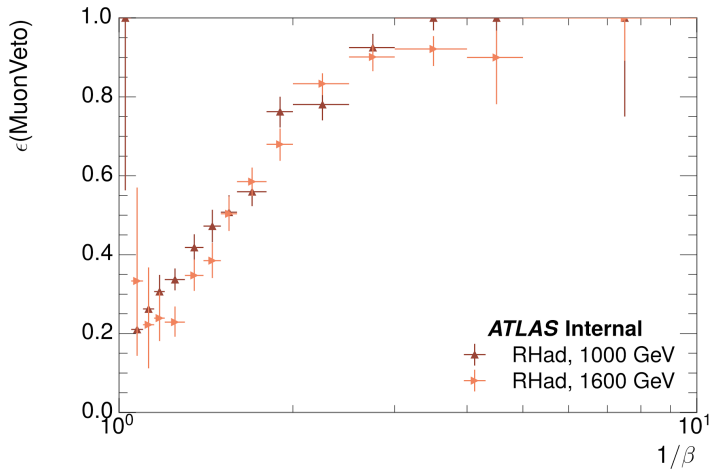


Figure 47: The efficiency of the muon veto for R -hadrons of two different masses, as a function of $\frac{1}{\beta}$ for simulated R-Hadron tracks.

1977 Thus, the efficiency of the muon veto depends on the timing resolution of the
 1978 spectrometer, so an uncertainty is applied to the signal efficiency to cover dif-

1979 differences in timing resolution between data and simulation. First, a sample of
 1980 $Z \rightarrow \mu\mu$ events is selected in data in which one of the muons has a late arrival
 1981 time measured in the Monitored Drift Tube ([MDT](#)). Then the reconstructed β
 1982 distribution is compared to the distribution in simulated $Z \rightarrow \mu\mu$ events; the
 1983 difference between these two distributions reflects the difference in timing res-
 1984 olution between data and simulation. To emulate this difference in simulated
 1985 signal events, the magnitude of the difference is used to scale and shift the true
 1986 β distribution of R-Hadrons in simulation. Signal events are then reweighted
 1987 based on this varied β distribution, and the difference in the efficiency of the
 1988 muon veto selection is compared with the nominal and reweighted true β distri-
 1989 butions. The difference in muon veto efficiency is taken as a systematic uncer-
 1990 tainty of the muon veto.

1991 The comparison of reconstructed β between data and simulation is performed
 1992 separately in the barrel, transition, and endcap regions of the spectrometer, and
 1993 the reweighting of the true β distribution in signal is done per region. The com-
 1994 parison of average reconstructed [MDT](#) β between data and simulation for the
 1995 barrel region is shown in Figure 48 for $Z \rightarrow \mu\mu$ events. As expected, The uncer-
 1996 tainty is found to be negligible for R-hadrons with short lifetimes, and is only
 1997 significant for lifetimes above 30 ns.

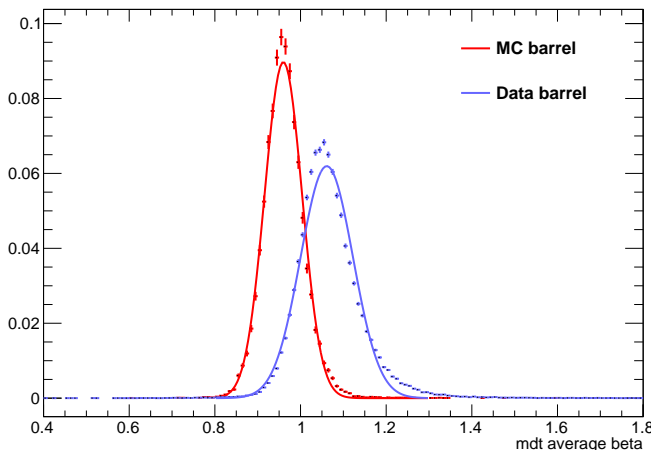


Figure 48: The average reconstructed MDT β distribution for $Z \rightarrow \mu\mu$ events in which
 one of the muons is reconstructed as a slow muon, for both data and simula-
 tion. A gaussian fit is superimposed.

1998 13.1.2.9 LUMINOSITY

1999 The luminosity uncertainty is provided by a luminosity measurement on [ATLAS](#)
 2000 and was measured to be 5% at the time of the publication of this analysis.

2001 13.1.2.10 SIGNAL SIZE

2002 As discussed in Section 10.2, the signal cross sections are calculated at [NLO](#) in the
 2003 strong coupling constant with a resummation of soft-gluon emission at [NLL](#). The

Selection Region	Expected Background	Data
Stable	$17.2 \pm 2.6 \pm 1.2$	16
Metastable	$11.1 \pm 1.7 \pm 0.7$	11

Table 6: The estimated number of background events and the number of observed events in data for the specified selection regions prior to the requirement on mass. The background estimates show statistical and systematic uncertainties.

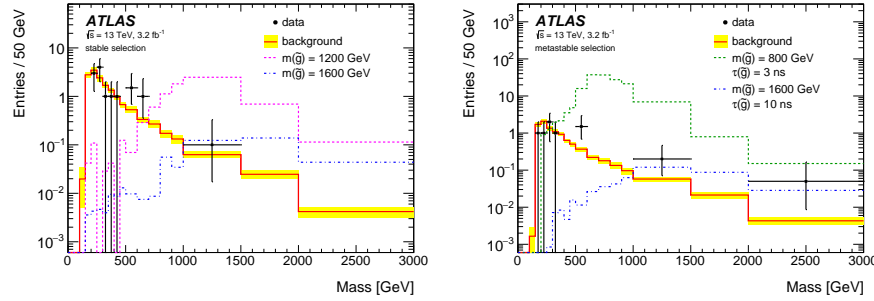


Figure 49: The observed mass distribution of events in data and the generated background distribution in (a) the stable and (b) the metastable signal region. A few example simulated signal distributions are superimposed.

uncertainties on those cross sections are between 14% to 28% for the R-Hadrons in the range of 400 to 1800 GeV [73, 74], where the uncertainty increases with the mass.

13.2 FINAL YIELDS

This full analysis was performed using the 3.2 fb^{-1} from the 2015 data-taking. Using the selections discussed in Chapter 11, sixteen events were observed in the stable signal region and eleven events were observed in the metastable signal region, prior to requirements on the candidate track mass. The background estimate discussed in Chapter 12 predicts $17 \pm 2.6(\text{stat}) \pm 1.2(\text{syst})$ events for the stable region and $11.1 \pm 1.7(\text{stat}) \pm 0.7(\text{syst})$ events for the metastable region. These counts are summarized in Table 6.

The mass estimated using dE/dx (Section 11.4.1) provides the final discriminating variable, where the signal would be expected as an excess in the falling exponential tail of the expected background. The observed distribution of masses is shown in Figure 49, along with the predicted distribution from the background estimate for each signal region. Both include a few example simulated signal distributions, which show the scale of an excess were the R-Hadron signals present. There is no statistically significant evidence of an excess in the data over the background estimation. From this distribution it is clearly possible to rule out signals with lower masses, around 1200 GeV, which have larger cross sections.

13.3 CROSS SECTIONAL LIMITS

Because there is no observed significant excess of events in the signal region, this analysis sets upper limits on the allowed cross section for R-Hadron production. These limits are set for each mass point by counting the observed events in data, along with the expected background and simulated signal events, in windows of mass. The mass windows are formed by fitting the distribution of signal events to a Gaussian distribution, and the window is then $\pm 1.4\sigma$ around the center of that Gaussian. Two examples of the windows formed by this procedure are shown in Tables 7–8, for the stable and 10 ns working points. The corresponding counts of observed data, expected background, and simulated signal for those same working points are shown in Tables 9–10. Appendix B includes the mass windows and counts for all of the considered signal points.

$m(\tilde{g})$ [GeV]	Left Extremum [GeV]	Right Extremum [GeV]
1000	655	1349
1100	734	1455
1200	712	1631
1300	792	1737
1400	717	1926
1500	815	2117
1600	824	2122
1700	900	2274
1800	919	2344

Table 7: The left and right extremum of the mass window for each generated mass point with a 10 ns lifetime.

$m(\tilde{g})$ [GeV]	Left Extremum [GeV]	Right Extremum [GeV]
800	627	1053
1000	726	1277
1200	857	1584
1400	924	1937
1600	993	2308
1800	1004	2554

Table 8: The left and right extremum of the mass window used for each generated stable mass point.

The 95% confidence level upper limits on the cross sections for a large grid of masses (between 800 and 1800 GeV) and lifetimes (between 0.4 and stable) are extracted from these counts with the CL_S method using the profile likelihood

$m(\tilde{g})$ [GeV]	Expected Signal	Expected Background	Observed Data
800	462.83 ± 14.86	1.764 ± 0.080	2.0
1000	108.73 ± 3.38	1.458 ± 0.070	1.0
1200	31.74 ± 0.95	1.137 ± 0.060	1.0
1400	10.22 ± 0.29	1.058 ± 0.058	1.0
1600	3.07 ± 0.09	0.947 ± 0.054	1.0
1800	1.08 ± 0.05	0.940 ± 0.054	1.0

Table 9: The expected number of signal events, the expected number of background events, and the observed number of events in data with their respective statistical errors within the respective mass window for each generated stable mass point

$m(\tilde{g})$ [GeV]	Expected Signal	Expected Background	Observed Data
1000	144.48 ± 5.14	1.499 ± 0.069	2.0
1100	73.19 ± 2.61	1.260 ± 0.060	2.0
1200	41.54 ± 1.41	1.456 ± 0.067	2.0
1300	22.58 ± 0.77	1.201 ± 0.058	2.0
1400	12.70 ± 0.42	1.558 ± 0.071	2.0
1500	6.73 ± 0.24	1.237 ± 0.060	2.0
1600	3.90 ± 0.13	1.201 ± 0.058	2.0
1700	2.27 ± 0.07	1.027 ± 0.052	2.0
1800	1.34 ± 0.04	1.019 ± 0.052	2.0

Table 10: The expected number of signal events, the expected number of background events, and the observed number of events in data with their respective statistical errors within the respective mass window for each generated mass point with a lifetime of 10 ns.

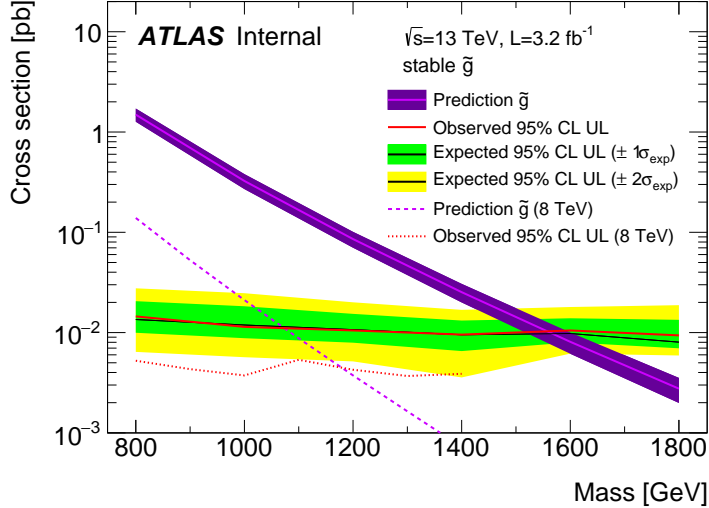


Figure 50: The observed and expected cross section limits as a function of mass for the stable simulated signal. The predicted cross section values for the corresponding signals are included.

ratio as a test statistic [78]. For this procedure, the systematic uncertainties estimated for the signal and background yields are treated as Gaussian-distributed nuisance parameters. The uncertainty on the normalization of the expected background distribution is included in the expected background events. At this point the expected cross section limit is calculated for both the metastable and stable signal region for each lifetime point, and the region with the best expected limit is selected for each lifetime. Using that procedure, the metastable region is used for lifetimes up to and including 30 ns, and the stable region for lifetimes above it.

The resulting cross-sectional upper limits are shown as a function of mass in Figure 50 and Figure 51 for each lifetime considered. The limits are interpolated linearly between each mass point, and the dependence of the limit on the mass is small as the efficiency is relatively constant for large R-Hadron masses. There is however a strong dependence on lifetime, as discussed in Section 11.5, where the probability to form a fully reconstructed track and the kinematic freedom to produce E_T^{miss} result in a local maximum in the limit at 10–30 ns. The figures also include the expected cross section for pair-produced gluino R-Hadrons for reference. For the 10 ns and stable cross section limits, both the observed limit and expected cross section for the Run 1, 8 TeV version of this analysis are included. There the cross sectional limits are lower because of the increased available luminosity, while the signal cross sections were also much lower because of the lower collision energy.

13.4 MASS LIMITS

The cross-sectional limits can then be used to derive a lower mass limit for gluino R-Hadrons by comparing them to the theoretically predicted production cross

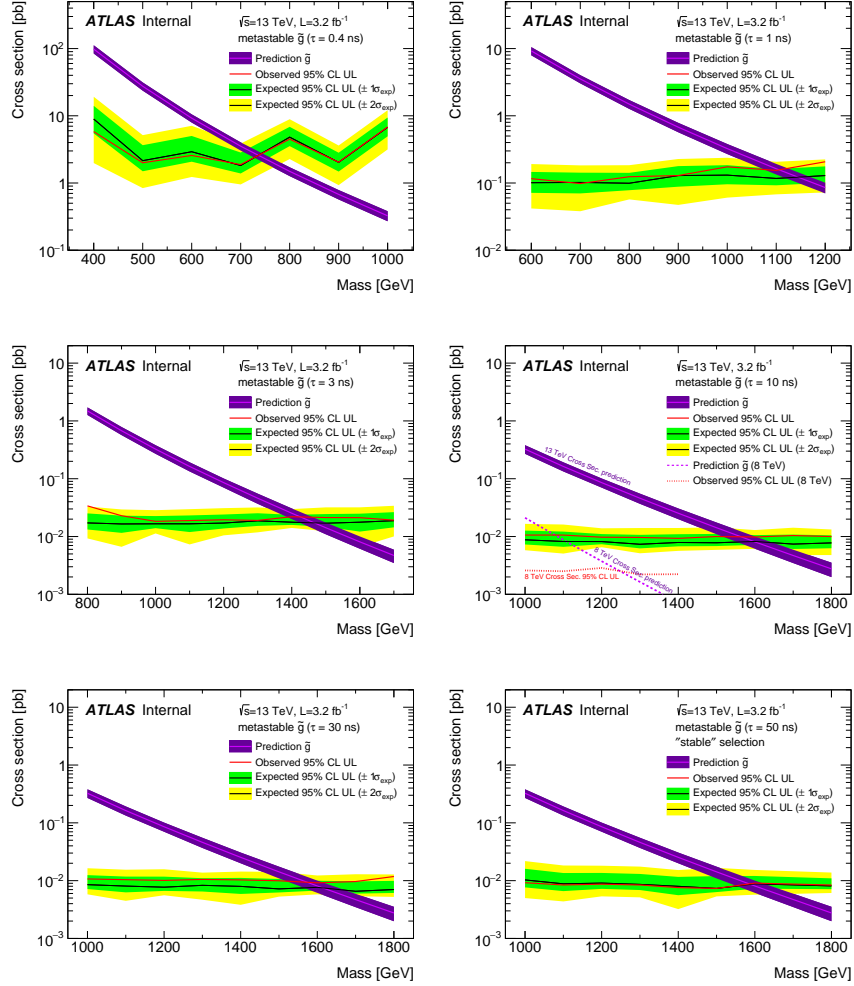


Figure 51: The observed and expected cross section limits as a function of mass for each generated lifetime. The predicted cross section values for the corresponding signals are included.

sections. These mass limits range from only 740 GeV at the lowest lifetimes considered, where the selection efficiency is very low, to up to 1580 GeV at 30 ns where the selection efficiency is maximized. The observed and expected mass limits for each lifetime point are detailed in Table 11, which also lists which selection region was used for each lifetime. These excluded range of masses as a function of lifetime is also shown in Figure 52. The Run 1 limits are included for comparison; the limits have increased by about 200 GeV on average. The search has also improved since the previous incarnation from Run 1 in optimizing the region between 30 GeV and detector-stable lifetimes by introducing the second signal region. The definition of the stable region prevents the significant drop in mass limit that occurred above 30 GeV in the Run 1 analysis.

Selection	τ [ns]	$M_{\text{obs}} > [\text{GeV}]$	$M_{\text{exp}} > [\text{GeV}]$
Metastable	0.4	740	730
"	1.0	1110	1150
"	3.0	1430	1470
"	10	1570	1600
"	30	1580	1620
Stable	50	1590	1590
"	stable	1570	1580

Table 11: The observed and expected 95% CL lower limit on mass for gluino R-Hadrons for each considered lifetime.

13.5 CONTEXT FOR LONG-LIVED SEARCHES

This search plays an important role in the current, combined ATLAS search for long lived particles. The mass limits provided by various ATLAS searches for long-lived gluino R-Hadrons can be seen in Figure 53. This search provides the most competitive limit for lifetimes between 3 ns up through very long lifetimes, where it is still competitive with dedicated searches for stable particles. The limits placed on gluino production are very similar to the limits on promptly decaying models.

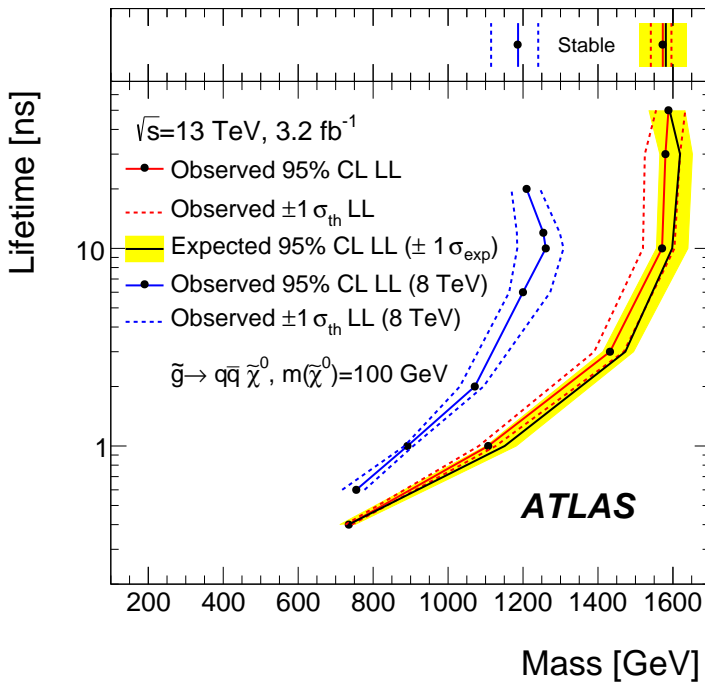


Figure 52: The excluded range of masses as a function of gluino lifetime. The expected lower limit (LL), with its experimental $\pm 1\sigma$ band, is given with respect to the nominal theoretical cross-section. The observed 95% LL obtained at $\sqrt{s} = 8 \text{ TeV}$ [61] is also shown for comparison.

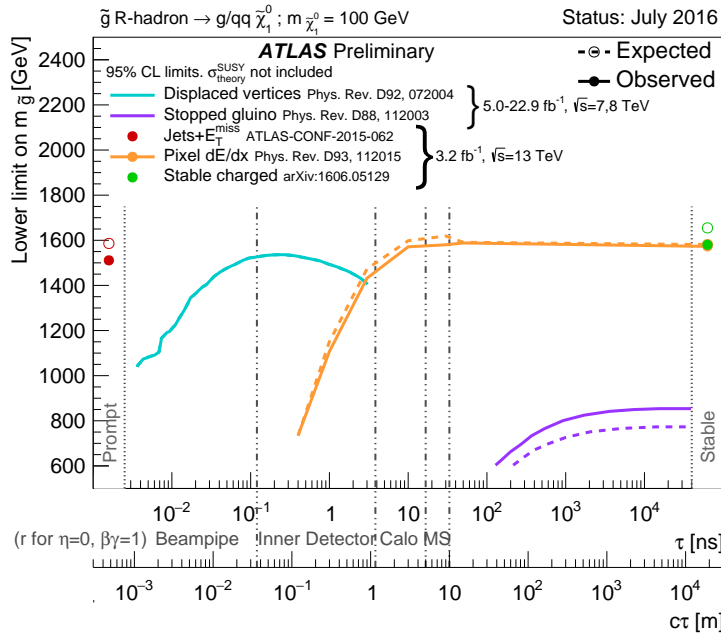


Figure 53: The constraints on the gluino mass as a function of lifetime for a split-supersymmetry model with the gluino R-Hadrons decaying into a gluon or light quarks and a neutralino with mass of 100 GeV. The solid lines indicate the observed limits, while the dashed lines indicate the expected limits. The area below the curves is excluded. The dots represent results for which the particle is assumed to be prompt or stable.

2083

PART VI

2084

CONCLUSIONS

2085

You can put some informational part preamble text here.

14

2086

2087 SUMMARY AND OUTLOOK

2088 14.1 SUMMARY

2089 14.2 OUTLOOK

2090

PART VII

2091

APPENDIX

2092

A

2093

2094 INELASTIC CROSS SECTION

B

2095

2096 EXPANDED R-HADRON YIELDS AND LIMITS

$m(\tilde{g})$ [GeV]	Left Extremum [GeV]	Right Extremum [GeV]
1000	682	1387
1100	763	1478
1200	801	1606
1300	809	1841
1400	861	2011
1500	920	2032
1600	952	2173
1800	1017	2422

Table 12: The left and right extremum of the mass window for each generated mass point with a 50 ns lifetime.

$m(\tilde{g})$ [GeV]	Left Extremum [GeV]	Right Extremum [GeV]
1000	689	1321
1100	746	1513
1200	788	1670
1300	860	1734
1400	833	1925
1500	852	2048
1600	833	2283
1700	946	2379
1800	869	2505

Table 13: The left and right extremum of the mass window for each generated mass point with a 30 ns lifetime.

$m(\tilde{g})$ [GeV]	Left Extremum [GeV]	Right Extremum [GeV]
1000	655	1349
1100	734	1455
1200	712	1631
1300	792	1737
1400	717	1926
1500	815	2117
1600	824	2122
1700	900	2274
1800	919	2344

Table 14: The left and right extremum of the mass window for each generated mass point with a 10 ns lifetime.

$m(\tilde{g})$ [GeV]	Left Extremum [GeV]	Right Extremum [GeV]
800	531	1065
900	576	1165
1000	610	1345
1100	635	1432
1200	663	1563
1300	620	1667
1400	742	1727
1500	761	1937
1600	573	2000
1700	621	2182

Table 15: The left and right extremum of the mass window used for each generated mass point with a lifetime of 3 ns.

$m(\tilde{g})$ [GeV]	Left Extremum [GeV]	Right Extremum [GeV]
600	411	758
700	385	876
800	486	970
900	406	987
1000	408	1136
1100	555	1196
1200	516	1378

Table 16: The left and right extremum of the mass window used for each mass point with a lifetime of 1 ns.

$m(\tilde{g})$ [GeV]	Left Extremum [GeV]	Right Extremum [GeV]
400	204	510
500	295	639
600	288	702
700	323	701
800	190	771
900	277	677
1000	249	688

Table 17: The left and right extremum of the mass window for each generated mass point with a lifetime of 0.4 ns.

$m(\tilde{g})$ [GeV]	Left Extremum [GeV]	Right Extremum [GeV]
800	627	1053
1000	726	1277
1200	857	1584
1400	924	1937
1600	993	2308
1800	1004	2554

Table 18: The left and right extremum of the mass window used for each generated stable mass point.

$m(\tilde{g})$ [GeV]	Expected Signal	Expected Background	Observed Data
1000	131.18 ± 6.35	1.803 ± 0.081	1.0 ± 1.0
1100	71.11 ± 3.35	1.409 ± 0.069	1.0 ± 1.0
1200	37.18 ± 1.75	1.310 ± 0.066	1.0 ± 1.0
1300	20.76 ± 0.95	1.431 ± 0.069	1.0 ± 1.0
1400	12.63 ± 0.57	1.273 ± 0.065	1.0 ± 1.0
1500	6.57 ± 0.29	1.115 ± 0.059	1.0 ± 1.0
1600	3.56 ± 0.16	1.041 ± 0.057	1.0 ± 1.0
1800	1.27 ± 0.05	0.918 ± 0.053	1.0 ± 1.0

Table 19: The expected number of signal events, the expected number of background events, and the observed number of events in data with their respective statistical errors within the respective mass window for each generated mass point with a lifetime of 50 ns.

$m(\tilde{g})$ [GeV]	Expected Signal	Expected Background	Observed Data
1000	144.65 ± 6.34	1.328 ± 0.063	2.0 ± 1.4
1100	75.28 ± 3.27	1.255 ± 0.060	2.0 ± 1.4
1200	40.51 ± 1.75	1.193 ± 0.058	2.0 ± 1.4
1300	20.91 ± 0.93	0.997 ± 0.051	2.0 ± 1.4
1400	11.97 ± 0.51	1.131 ± 0.056	2.0 ± 1.4
1500	6.81 ± 0.28	1.111 ± 0.055	2.0 ± 1.4
1600	4.19 ± 0.16	1.193 ± 0.058	2.0 ± 1.4
1700	2.42 ± 0.09	0.963 ± 0.050	2.0 ± 1.4
1800	1.46 ± 0.05	1.138 ± 0.056	3.0 ± 1.7

Table 20: The expected number of signal events, the expected number of background events, and the observed number of events in data with their respective statistical errors within the respective mass window for each generated mass point with a lifetime of 30 ns.

$m(\tilde{g})$ [GeV]	Expected Signal	Expected Background	Observed Data
1000	144.48 ± 5.14	1.499 ± 0.069	2.0 ± 1.4
1100	73.19 ± 2.61	1.260 ± 0.060	2.0 ± 1.4
1200	41.54 ± 1.41	1.456 ± 0.067	2.0 ± 1.4
1300	22.58 ± 0.77	1.201 ± 0.058	2.0 ± 1.4
1400	12.70 ± 0.42	1.558 ± 0.071	2.0 ± 1.4
1500	6.73 ± 0.24	1.237 ± 0.060	2.0 ± 1.4
1600	3.90 ± 0.13	1.201 ± 0.058	2.0 ± 1.4
1700	2.27 ± 0.07	1.027 ± 0.052	2.0 ± 1.4
1800	1.34 ± 0.04	1.019 ± 0.052	2.0 ± 1.4

Table 21: The expected number of signal events, the expected number of background events, and the observed number of events in data with their respective statistical errors within the respective mass window for each generated mass point with a lifetime of 10 ns.

$m(\tilde{g})$ [GeV]	Expected Signal	Expected Background	Observed Data
800	362.97 ± 14.68	1.841 ± 0.080	5.0 ± 2.2
900	169.20 ± 6.69	1.710 ± 0.076	3.0 ± 1.7
1000	84.78 ± 3.23	1.727 ± 0.076	2.0 ± 1.4
1100	40.06 ± 1.60	1.679 ± 0.075	2.0 ± 1.4
1200	20.06 ± 0.81	1.598 ± 0.072	2.0 ± 1.4
1300	10.76 ± 0.43	1.851 ± 0.080	2.0 ± 1.4
1400	5.52 ± 0.22	1.374 ± 0.064	2.0 ± 1.4
1500	3.16 ± 0.13	1.355 ± 0.064	2.0 ± 1.4
1600	2.13 ± 0.11	2.235 ± 0.093	3.0 ± 1.7
1700	1.10 ± 0.06	1.995 ± 0.085	2.0 ± 1.4

Table 22: The expected number of signal events, the expected number of background events, and the observed number of events in data with their respective statistical errors within the respective mass window for each generated mass point with a lifetime of 3 ns.

$m(\tilde{g})$ [GeV]	Expected Signal	Expected Background	Observed Data
600	431.80 ± 36.60	2.418 ± 0.099	3.0 ± 1.7
700	192.77 ± 15.28	3.267 ± 0.126	3.0 ± 1.7
800	69.63 ± 5.90	2.125 ± 0.089	3.0 ± 1.7
900	28.91 ± 2.59	3.114 ± 0.121	3.0 ± 1.7
1000	13.64 ± 1.22	3.359 ± 0.129	5.0 ± 2.2
1100	6.13 ± 0.57	1.879 ± 0.081	3.0 ± 1.7
1200	3.24 ± 0.30	2.387 ± 0.098	5.0 ± 2.2

Table 23: The expected number of signal events, the expected number of background events, and the observed number of events in data with their respective statistical errors within the respective mass window for each generated mass point with a lifetime of 1 ns.

$m(\tilde{g})$ [GeV]	Expected Signal	Expected Background	Observed Data
400	181.71 ± 75.59	6.780 ± 0.238	4.0 ± 2.0
500	103.88 ± 30.05	4.310 ± 0.160	4.0 ± 2.0
600	28.34 ± 9.34	4.868 ± 0.177	4.0 ± 2.0
700	13.62 ± 4.00	3.908 ± 0.147	4.0 ± 2.0
800	2.75 ± 1.15	9.001 ± 0.308	8.0 ± 2.8
900	2.25 ± 0.71	5.045 ± 0.183	5.0 ± 2.2
1000	0.34 ± 0.19	6.026 ± 0.214	6.0 ± 2.4

Table 24: The expected number of signal events, the expected number of background events, and the observed number of events in data with their respective statistical errors within the respective mass window for each generated mass point with a lifetime of p4 ns.

$m(\tilde{g})$ [GeV]	Expected Signal	Expected Background	Observed Data
800	462.83 ± 14.86	1.764 ± 0.080	2.0 ± 1.4
1000	108.73 ± 3.38	1.458 ± 0.070	1.0 ± 1.0
1200	31.74 ± 0.95	1.137 ± 0.060	1.0 ± 1.0
1400	10.22 ± 0.29	1.058 ± 0.058	1.0 ± 1.0
1600	3.07 ± 0.09	0.947 ± 0.054	1.0 ± 1.0
1800	1.08 ± 0.05	0.940 ± 0.054	1.0 ± 1.0

Table 25: The expected number of signal events, the expected number of background events, and the observed number of events in data with their respective statistical errors within the respective mass window for each generated stable mass point

2097 BIBLIOGRAPHY

- 2098 [1] Lyndon Evans and Philip Bryant. "LHC Machine". In: *JINST* 3 (2008), S08001.
2099 doi: [10.1088/1748-0221/3/08/S08001](https://doi.org/10.1088/1748-0221/3/08/S08001).
- 2100 [2] C Lefevre. "LHC: the guide (English version). Guide du LHC (version anglaise)".
2101 2009. URL: <https://cds.cern.ch/record/1165534>.
- 2102 [3] ATLAS Collaboration. "The ATLAS Experiment at the CERN Large Hadron
2103 Collider". In: *JINST* 3 (2008), S08003. doi: [10.1088/1748-0221/3/08/S08003](https://doi.org/10.1088/1748-0221/3/08/S08003).
- 2105 [4] S. Chatrchyan et al. "The CMS experiment at the CERN LHC". In: *JINST*
2106 3 (2008), S08004. doi: [10.1088/1748-0221/3/08/S08004](https://doi.org/10.1088/1748-0221/3/08/S08004).
- 2107 [5] A. Augusto Alves Jr. et al. "The LHCb Detector at the LHC". In: *JINST* 3
2108 (2008), S08005. doi: [10.1088/1748-0221/3/08/S08005](https://doi.org/10.1088/1748-0221/3/08/S08005).
- 2109 [6] K. Aamodt et al. "The ALICE experiment at the CERN LHC". In: *JINST* 3
2110 (2008), S08002. doi: [10.1088/1748-0221/3/08/S08002](https://doi.org/10.1088/1748-0221/3/08/S08002).
- 2111 [7] S. Agostinelli et al. "GEANT4: A simulation toolkit". In: *Nucl. Instrum. Meth.*
2112 A 506 (2003), pp. 250–303. doi: [10.1016/S0168-9002\(03\)01368-8](https://doi.org/10.1016/S0168-9002(03)01368-8).
- 2113 [8] ATLAS Collaboration. "A study of the material in the ATLAS inner de-
2114 tector using secondary hadronic interactions". In: *JINST* 7 (2012), P01013.
2115 doi: [10.1088/1748-0221/7/01/P01013](https://doi.org/10.1088/1748-0221/7/01/P01013). arXiv: [1110.6191 \[hep-ex\]](https://arxiv.org/abs/1110.6191).
2116 PERF-2011-08.
- 2117 [9] ATLAS Collaboration. "Electron and photon energy calibration with the
2118 ATLAS detector using LHC Run 1 data". In: *Eur. Phys. J. C* 74 (2014), p. 3071.
2119 doi: [10.1140/epjc/s10052-014-3071-4](https://doi.org/10.1140/epjc/s10052-014-3071-4). arXiv: [1407.5063](https://arxiv.org/abs/1407.5063)
2120 [hep-ex]. PERF-2013-05.
- 2121 [10] ATLAS Collaboration. "A measurement of the calorimeter response to sin-
2122 ggle hadrons and determination of the jet energy scale uncertainty using
2123 LHC Run-1 pp -collision data with the ATLAS detector". In: (2016). arXiv:
2124 [1607.08842 \[hep-ex\]](https://arxiv.org/abs/1607.08842). PERF-2015-05.
- 2125 [11] ATLAS Collaboration. "Single hadron response measurement and calorime-
2126 ter jet energy scale uncertainty with the ATLAS detector at the LHC". In:
2127 *Eur. Phys. J. C* 73 (2013), p. 2305. doi: [10.1140/epjc/s10052-013-2305-1](https://doi.org/10.1140/epjc/s10052-013-2305-1). arXiv: [1203.1302 \[hep-ex\]](https://arxiv.org/abs/1203.1302). PERF-2011-05.
- 2129 [12] ATLAS Collaboration. "The ATLAS Simulation Infrastructure". In: *Eur.*
2130 *Phys. J. C* 70 (2010), p. 823. doi: [10.1140/epjc/s10052-010-1429-9](https://doi.org/10.1140/epjc/s10052-010-1429-9).
2131 arXiv: [1005.4568 \[hep-ex\]](https://arxiv.org/abs/1005.4568). SOFT-2010-01.
- 2132 [13] T. Sjöstrand, S. Mrenna, and P. Skands. "A Brief Introduction to PYTHIA
2133 8.1". In: *Comput. Phys. Commun.* 178 (2008), pp. 852–867. doi: [10.1016/j.cpc.2008.01.036](https://doi.org/10.1016/j.cpc.2008.01.036). arXiv: [0710.3820](https://arxiv.org/abs/0710.3820).

- 2135 [14] ATLAS Collaboration. *Summary of ATLAS Pythia 8 tunes*. ATL-PHYS-PUB-
 2136 2012-003. 2012. URL: <http://cds.cern.ch/record/1474107>.
- 2137 [15] A.D. Martin, W.J. Stirling, R.S. Thorne, and G. Watt. “Parton distributions
 2138 for the LHC”. In: *Eur. Phys. J. C* 63 (2009). Figures from the MSTW Website,
 2139 pp. 189–285. doi: [10.1140/epjc/s10052-009-1072-5](https://doi.org/10.1140/epjc/s10052-009-1072-5). arXiv: [0901.0002](https://arxiv.org/abs/0901.0002).
- 2140
- 2141 [16] A. Sherstnev and R.S. Thorne. “Parton Distributions for LO Generators”.
 2142 In: *Eur. Phys. J. C* 55 (2008), pp. 553–575. doi: [10.1140/epjc/s10052-008-0610-x](https://doi.org/10.1140/epjc/s10052-008-0610-x). arXiv: [0711.2473](https://arxiv.org/abs/0711.2473).
- 2143
- 2144 [17] A. Ribon et al. *Status of Geant4 hadronic physics for the simulation of LHC*
 2145 *experiments at the start of LHC physics program*. CERN-LCGAPP-2010-02.
 2146 2010. URL: <http://lcgapp.cern.ch/project/docs/noteStatusHadronic2010.pdf>.
- 2147
- 2148 [18] M. P. Guthrie, R. G. Alsmiller, and H. W. Bertini. “Calculation of the cap-
 2149 ture of negative pions in light elements and comparison with experiments
 2150 pertaining to cancer radiotherapy”. In: *Nucl. Instrum. Meth.* 66 (1968), pp. 29–
 2151 36. doi: [10.1016/0029-554X\(68\)90054-2](https://doi.org/10.1016/0029-554X(68)90054-2).
- 2152 [19] H. W. Bertini and P. Guthrie. “News item results from medium-energy
 2153 intranuclear-cascade calculation”. In: *Nucl. Instr. and Meth. A* 169 (1971),
 2154 p. 670. doi: [10.1016/0375-9474\(71\)90710-X](https://doi.org/10.1016/0375-9474(71)90710-X).
- 2155 [20] V.A. Karmanov. “Light Front Wave Function of Relativistic Composite
 2156 System in Explicitly Solvable Model”. In: *Nucl. Phys. B* 166 (1980), p. 378.
 2157 doi: [10.1016/0550-3213\(80\)90204-7](https://doi.org/10.1016/0550-3213(80)90204-7).
- 2158 [21] H. S. Fesefeldt. *GHEISHA program*. Pitha-85-02, Aachen. 1985.
- 2159 [22] G. Folger and J.P. Wellisch. “String parton models in Geant4”. In: (2003).
 2160 arXiv: [nucl-th/0306007](https://arxiv.org/abs/nucl-th/0306007).
- 2161 [23] N. S. Amelin et al. “Transverse flow and collectivity in ultrarelativistic
 2162 heavy-ion collisions”. In: *Phys. Rev. Lett.* 67 (1991), p. 1523. doi: [10.1103/PhysRevLett.67.1523](https://doi.org/10.1103/PhysRevLett.67.1523).
- 2163
- 2164 [24] N. S. Amelin et al. “Collectivity in ultrarelativistic heavy ion collisions”. In:
 2165 *Nucl. Phys. A* 544 (1992), p. 463. doi: [10.1016/0375-9474\(92\)90598-E](https://doi.org/10.1016/0375-9474(92)90598-E).
- 2166
- 2167 [25] L. V. Bravina et al. “Fluid dynamics and Quark Gluon string model - What
 2168 we can expect for Au+Au collisions at 11.6 AGeV/c”. In: *Nucl. Phys. A* 566
 2169 (1994), p. 461. doi: [10.1016/0375-9474\(94\)90669-6](https://doi.org/10.1016/0375-9474(94)90669-6).
- 2170 [26] L. V. Bravin et al. “Scaling violation of transverse flow in heavy ion colli-
 2171 sions at AGS energies”. In: *Phys. Lett. B* 344 (1995), p. 49. doi: [10.1016/0370-2693\(94\)01560-Y](https://doi.org/10.1016/0370-2693(94)01560-Y).
- 2172
- 2173 [27] B. Andersson et al. “A model for low-pT hadronic reactions with general-
 2174 izations to hadron-nucleus and nucleus-nucleus collisions”. In: *Nucl. Phys.*
 2175 *B* 281 (1987), p. 289. doi: [10.1016/0550-3213\(87\)90257-4](https://doi.org/10.1016/0550-3213(87)90257-4).

- 2176 [28] B. Andersson, A. Tai, and B.-H. Sa. “Final state interactions in the (nuclear)
 2177 FRITIOF string interaction scenario”. In: *Z. Phys. C* 70 (1996), pp. 499–
 2178 506. doi: [10.1007/s002880050127](https://doi.org/10.1007/s002880050127).
- 2179 [29] B. Nilsson-Almqvist and E. Stenlund. “Interactions Between Hadrons and
 2180 Nuclei: The Lund Monte Carlo, Fritiof Version 1.6”. In: *Comput. Phys. Com-*
 2181 *mun.* 43 (1987), p. 387. doi: [10.1016/0010-4655\(87\)90056-7](https://doi.org/10.1016/0010-4655(87)90056-7).
- 2182 [30] B. Ganhuyag and V. Uzhinsky. “Modified FRITIOF code: Negative charged
 2183 particle production in high energy nucleus nucleus interactions”. In: *Czech.
 2184 J. Phys.* 47 (1997), pp. 913–918. doi: [10.1023/A:1021296114786](https://doi.org/10.1023/A:1021296114786).
- 2185 [31] ATLAS Collaboration. “Topological cell clustering in the ATLAS calorime-
 2186 ters and its performance in LHC Run 1”. In: (2016). arXiv: [1603.02934](https://arxiv.org/abs/1603.02934)
 2187 [[hep-ex](#)].
- 2188 [32] Peter Speckmayer. “Energy Measurement of Hadrons with the CERN AT-
 2189 LAS Calorimeter”. Presented on 18 Jun 2008. PhD thesis. Vienna: Vienna,
 2190 Tech. U., 2008. URL: <http://cds.cern.ch/record/1112036>.
- 2191 [33] CMS Collaboration. “The CMS barrel calorimeter response to particle
 2192 beams from 2 to 350 GeV/c”. In: *Eur. Phys. J. C* 60.3 (2009). doi: [10.1140/epjc/s10052-009-0959-5](https://doi.org/10.1140/epjc/s10052-009-0959-5).
- 2193 [34] J. Beringer et al. (Particle Data Group). “Review of Particle Physics”. In:
 2194 *Chin. Phys. C* 38 (2014), p. 090001. URL: <http://pdg.lbl.gov>.
- 2195 [35] P. Adragna et al. “Measurement of Pion and Proton Response and Lon-
 2196 gitudinal Shower Profiles up to 20 Nuclear Interaction Lengths with the
 2197 ATLAS Tile Calorimeter”. In: *Nucl. Instrum. Meth. A* 615 (2010), pp. 158–
 2198 181. doi: [10.1016/j.nima.2010.01.037](https://doi.org/10.1016/j.nima.2010.01.037).
- 2199 [36] ATLAS Collaboration. “Jet energy measurement and its systematic uncer-
 2200 tainty in proton–proton collisions at $\sqrt{s} = 7$ TeV with the ATLAS detec-
 2201 tor”. In: *Eur. Phys. J. C* 75 (2015), p. 17. doi: [10.1140/epjc/s10052-014-3190-y](https://doi.org/10.1140/epjc/s10052-014-3190-y). arXiv: [1406.0076](https://arxiv.org/abs/1406.0076) [[hep-ex](#)]. PERF-2012-01.
- 2202 [37] Hung-Liang Lai, Marco Guzzi, Joey Huston, Zhao Li, Pavel M. Nadolsky,
 2203 et al. “New parton distributions for collider physics”. In: *Phys. Rev. D* 82
 2204 (2010), p. 074024. doi: [10.1103/PhysRevD.82.074024](https://doi.org/10.1103/PhysRevD.82.074024). arXiv: [1007.2241](https://arxiv.org/abs/1007.2241) [[hep-ph](#)].
- 2205 [38] E. Abat et al. “Study of energy response and resolution of the ATLAS barrel
 2206 calorimeter to hadrons of energies from 20 to 350 GeV”. In: *Nucl. Instrum.
 2207 Meth. A* 621.1-3 (2010), pp. 134 –150. doi: <http://dx.doi.org/10.1016/j.nima.2010.04.054>.
- 2208 [39] ATLAS Collaboration. “Jet energy measurement with the ATLAS detector
 2209 in proton–proton collisions at $\sqrt{s} = 7$ TeV”. In: *Eur. Phys. J. C* 73 (2013),
 2210 p. 2304. doi: [10.1140/epjc/s10052-013-2304-2](https://doi.org/10.1140/epjc/s10052-013-2304-2). arXiv: [1112.6426](https://arxiv.org/abs/1112.6426) [[hep-ex](#)]. PERF-2011-03.
- 2211 [40] Nausheen R. Shah and Carlos E. M. Wagner. “Gravitons and dark matter in
 2212 universal extra dimensions”. In: *Phys. Rev. D* 74 (2006), p. 104008. doi: [10.1103/PhysRevD.74.104008](https://doi.org/10.1103/PhysRevD.74.104008). arXiv: [hep-ph/0608140](https://arxiv.org/abs/hep-ph/0608140) [[hep-ph](#)].

- 2219 [41] Jonathan L. Feng, Arvind Rajaraman, and Fumihiro Takayama. “Graviton
 2220 cosmology in universal extra dimensions”. In: *Phys. Rev.* D68 (2003), p. 085018.
 2221 doi: [10.1103/PhysRevD.68.085018](https://doi.org/10.1103/PhysRevD.68.085018). arXiv: [hep-ph/0307375](https://arxiv.org/abs/hep-ph/0307375)
 2222 [[hep-ph](#)].
- 2223 [42] Paul H. Frampton and Pham Quang Hung. “Long-lived quarks?” In: *Phys.
 2224 Rev. D* 58 (5 1998), p. 057704. doi: [10.1103/PhysRevD.58.057704](https://doi.org/10.1103/PhysRevD.58.057704).
 2225 url: [http://link.aps.org/doi/10.1103/PhysRevD.58.
 2226 057704](http://link.aps.org/doi/10.1103/PhysRevD.58.057704).
- 2227 [43] C. Friberg, E. Norrbin, and T. Sjostrand. “QCD aspects of leptoquark pro-
 2228 duction at HERA”. In: *Phys. Lett.* B403 (1997), pp. 329–334. doi: [10.1016/S0370-2693\(97\)00543-1](https://doi.org/10.1016/S0370-2693(97)00543-1). arXiv: [hep-ph/9704214](https://arxiv.org/abs/hep-ph/9704214) [[hep-ph](#)].
- 2229 [44] Herbert K. Dreiner. “An introduction to explicit R-parity violation”. In:
 2230 (1997). arXiv: [hep-ph/9707435](https://arxiv.org/abs/hep-ph/9707435).
- 2232 [45] Edmond L. Berger and Zack Sullivan. “Lower limits on R-parity-violating
 2233 couplings in supersymmetry”. In: *Phys. Rev. Lett.* 92 (2004), p. 201801. doi:
 2234 [10.1103/PhysRevLett.92.201801](https://doi.org/10.1103/PhysRevLett.92.201801). arXiv: [hep-ph/0310001](https://arxiv.org/abs/hep-ph/0310001).
- 2235 [46] R. Barbieri, C. Berat, M. Besancon, M. Chemtob, A. Deandrea, et al. “R-
 2236 parity violating supersymmetry”. In: *Phys. Rept.* 420 (2005), p. 1. doi: [10.1016/j.physrep.2005.08.006](https://doi.org/10.1016/j.physrep.2005.08.006). arXiv: [hep-ph/0406039](https://arxiv.org/abs/hep-ph/0406039).
- 2238 [47] M. Fairbairn et al. “Stable massive particles at colliders”. In: *Phys. Rept.* 438
 2239 (2007), p. 1. doi: [10.1016/j.physrep.2006.10.002](https://doi.org/10.1016/j.physrep.2006.10.002). arXiv: [hep-ph/0611040](https://arxiv.org/abs/hep-ph/0611040).
- 2241 [48] Christopher F. Kolda. “Gauge-mediated supersymmetry breaking: Intro-
 2242 duction, review and update”. In: *Nucl. Phys. Proc. Suppl.* 62 (1998), p. 266.
 2243 doi: [10.1016/S0920-5632\(97\)00667-1](https://doi.org/10.1016/S0920-5632(97)00667-1). arXiv: [hep-ph/9707450](https://arxiv.org/abs/hep-ph/9707450).
- 2244 [49] Howard Baer, Kingman Cheung, and John F. Gunion. “A Heavy gluino as
 2245 the lightest supersymmetric particle”. In: *Phys. Rev. D* 59 (1999), p. 075002.
 2246 doi: [10.1103/PhysRevD.59.075002](https://doi.org/10.1103/PhysRevD.59.075002). arXiv: [hep-ph/9806361](https://arxiv.org/abs/hep-ph/9806361).
- 2247 [50] S. James Gates Jr. and Oleg Lebedev. “Searching for supersymmetry in
 2248 hadrons”. In: *Phys. Lett. B* 477 (2000), p. 216. doi: [10.1016/S0370-2693\(00\)00172-6](https://doi.org/10.1016/S0370-2693(00)00172-6). arXiv: [hep-ph/9912362](https://arxiv.org/abs/hep-ph/9912362).
- 2250 [51] G. F. Giudice and A. Romanino. “Split supersymmetry”. In: *Nucl. Phys. B*
 2251 699 (2004), p. 65. doi: [10.1016/j.nuclphysb.2004.11.048](https://doi.org/10.1016/j.nuclphysb.2004.11.048). arXiv:
 2252 [hep-ph/0406088](https://arxiv.org/abs/hep-ph/0406088).
- 2253 [52] N. Arkani-Hamed, S. Dimopoulos, G. F. Giudice, and A. Romanino. “As-
 2254 pects of split supersymmetry”. In: *Nucl. Phys. B* 709 (2005), p. 3. doi: [10.1016/j.nuclphysb.2004.12.026](https://doi.org/10.1016/j.nuclphysb.2004.12.026). arXiv: [hep-ph/0409232](https://arxiv.org/abs/hep-ph/0409232).
- 2256 [53] Glennys R. Farrar and Pierre Fayet. “Phenomenology of the Production,
 2257 Decay, and Detection of New Hadronic States Associated with Supersym-
 2258 metry”. In: *Phys. Lett.* B76 (1978), pp. 575–579. doi: [10.1016/0370-2693\(78\)90858-4](https://doi.org/10.1016/0370-2693(78)90858-4).

- 2260 [54] A. C. Kraan, J. B. Hansen, and P. Nevski. “Discovery potential of R-hadrons
 2261 with the ATLAS detector”. In: *Eur. Phys. J.* C49 (2007), pp. 623–640. doi:
 2262 [10.1140/epjc/s10052-006-0162-x](https://doi.org/10.1140/epjc/s10052-006-0162-x). arXiv: [hep-ex/0511014](https://arxiv.org/abs/hep-ex/0511014)
 2263 [[hep-ex](#)].
- 2264 [55] K. A. Olive et al. “Review of Particle Physics”. In: *Chin. Phys.* C38 (2014),
 2265 p. 090001. doi: [10.1088/1674-1137/38/9/090001](https://doi.org/10.1088/1674-1137/38/9/090001).
- 2266 [56] Rasmus Mackeprang and David Milstead. “An Updated Description of
 2267 Heavy-Hadron Interactions in GEANT-4”. In: *Eur. Phys. J.* C66 (2010), pp. 493–
 2268 501. doi: [10.1140/epjc/s10052-010-1262-1](https://doi.org/10.1140/epjc/s10052-010-1262-1). arXiv: [0908.1868](https://arxiv.org/abs/0908.1868)
 2269 [[hep-ph](#)].
- 2270 [57] ATLAS Collaboration. “Search for massive, long-lived particles using mul-
 2271 titrack displaced vertices or displaced lepton pairs in pp collisions at $\sqrt{s} =$
 2272 8 TeV with the ATLAS detector”. In: *Phys. Rev. D* 92 (2015), p. 072004.
 2273 doi: [10.1103/PhysRevD.92.072004](https://doi.org/10.1103/PhysRevD.92.072004). arXiv: [1504.05162](https://arxiv.org/abs/1504.05162) [[hep-ex](#)].
 2274 SUSY-2014-02.
- 2275 [58] ATLAS Collaboration. “Search for charginos nearly mass degenerate with
 2276 the lightest neutralino based on a disappearing-track signature in pp col-
 2277 lisions at $\sqrt{s} = 8$ TeV with the ATLAS detector”. In: *Phys. Rev. D* 88 (2013),
 2278 p. 112006. doi: [10.1103/PhysRevD.88.112006](https://doi.org/10.1103/PhysRevD.88.112006). arXiv: [1310.3675](https://arxiv.org/abs/1310.3675)
 2279 [[hep-ex](#)]. SUSY-2013-01.
- 2280 [59] ATLAS Collaboration. “Searches for heavy long-lived sleptons and R-Hadrons
 2281 with the ATLAS detector in pp collisions at $\sqrt{s} = 7$ TeV”. In: *Phys. Lett. B*
 2282 720 (2013), p. 277. doi: [10.1016/j.physletb.2013.02.015](https://doi.org/10.1016/j.physletb.2013.02.015). arXiv:
 2283 [1211.1597](https://arxiv.org/abs/1211.1597) [[hep-ex](#)]. SUSY-2012-01.
- 2284 [60] ATLAS Collaboration. “Searches for heavy long-lived charged particles
 2285 with the ATLAS detector in proton–proton collisions at $\sqrt{s} = 8$ TeV”. In: *JHEP* 01 (2015), p. 068. doi: [10.1007/JHEP01\(2015\)068](https://doi.org/10.1007/JHEP01(2015)068). arXiv:
 2286 [1411.6795](https://arxiv.org/abs/1411.6795) [[hep-ex](#)]. SUSY-2013-22.
- 2288 [61] ATLAS Collaboration. “Search for metastable heavy charged particles with
 2289 large ionisation energy loss in pp collisions at $\sqrt{s} = 8$ TeV using the AT-
 2290 LAS experiment”. In: *Eur. Phys. J.* C 75 (2015), p. 407. doi: [10.1140/epjc/s10052-015-3609-0](https://doi.org/10.1140/epjc/s10052-015-3609-0). arXiv: [1506.05332](https://arxiv.org/abs/1506.05332) [[hep-ex](#)]. SUSY-
 2292 2014-09.
- 2293 [62] ATLAS Collaboration. “Search for heavy long-lived charged R -hadrons
 2294 with the ATLAS detector in 3.2 fb^{-1} of proton–proton collision data at
 2295 $\sqrt{s} = 13$ TeV”. In: *Phys. Lett.* B760 (2016), pp. 647–665. doi: [10.1016/j.physletb.2016.07.042](https://doi.org/10.1016/j.physletb.2016.07.042). arXiv: [1606.05129](https://arxiv.org/abs/1606.05129) [[hep-ex](#)].
- 2297 [63] Torbjorn Sjöstrand, Stephen Mrenna, and Peter Skands. “PYTHIA 6.4 Physics
 2298 and Manual”. In: *JHEP* 0605 (2006), p. 026. doi: [10.1088/1126-6708/2006/05/026](https://doi.org/10.1088/1126-6708/2006/05/026). arXiv: [hep-ph/0603175](https://arxiv.org/abs/hep-ph/0603175).
- 2300 [64] *Further ATLAS tunes of PYTHIA6 and Pythia 8*. Tech. rep. ATL-PHYS-PUB-
 2301 2011-014. Geneva: CERN, 2011. URL: <https://cds.cern.ch/record/1400677>.

- 2303 [65] Aafke Christine Kraan. “Interactions of heavy stable hadronizing parti-
 2304 cles”. In: *Eur. Phys. J.* C37 (2004), pp. 91–104. doi: [10.1140/epjc/s2004-01946-6](https://doi.org/10.1140/epjc/s2004-01946-6). arXiv: [hep-ex/0404001](https://arxiv.org/abs/hep-ex/0404001) [hep-ex].
- 2306 [66] M. Fairbairn et al. “Stable massive particles at colliders”. In: *Phys. Rept.* 438
 2307 (2007), p. 1. doi: [10.1016/j.physrep.2006.10.002](https://doi.org/10.1016/j.physrep.2006.10.002). arXiv: [hep-ph/0611040](https://arxiv.org/abs/hep-ph/0611040).
- 2309 [67] W. Beenakker, R. Hopker, M. Spira, and P. M. Zerwas. “Squark and gluino
 2310 production at hadron colliders”. In: *Nucl. Phys. B* 492 (1997), p. 51. doi:
 2311 [10.1016/S0550-3213\(97\)00084-9](https://doi.org/10.1016/S0550-3213(97)00084-9). arXiv: [hep-ph/9610490](https://arxiv.org/abs/hep-ph/9610490).
- 2312 [68] A. Kulesza and L. Motyka. “Threshold resummation for squark-antisquark
 2313 and gluino-pair production at the LHC”. In: *Phys. Rev. Lett.* 102 (2009),
 2314 p. 111802. doi: [10.1103/PhysRevLett.102.111802](https://doi.org/10.1103/PhysRevLett.102.111802). arXiv: [0807.2405](https://arxiv.org/abs/0807.2405) [hep-ph].
- 2316 [69] A. Kulesza and L. Motyka. “Soft gluon resummation for the production
 2317 of gluino-gluino and squark-antisquark pairs at the LHC”. In: *Phys. Rev.*
 2318 D 80 (2009), p. 095004. doi: [10.1103/PhysRevD.80.095004](https://doi.org/10.1103/PhysRevD.80.095004). arXiv:
 2319 [0905.4749](https://arxiv.org/abs/0905.4749) [hep-ph].
- 2320 [70] Wim Beenakker, Silja Brensing, Michael Kramer, Anna Kulesza, Eric Lae-
 2321 nen, et al. “Soft-gluon resummation for squark and gluino hadroproduc-
 2322 tion”. In: *JHEP* 0912 (2009), p. 041. doi: [10.1088/1126-6708/2009/12/041](https://doi.org/10.1088/1126-6708/2009/12/041). arXiv: [0909.4418](https://arxiv.org/abs/0909.4418) [hep-ph].
- 2324 [71] W. Beenakker, S. Brensing, M.n Kramer, A. Kulesza, E. Laenen, et al. “Squark
 2325 and Gluino Hadroproduction”. In: *Int. J. Mod. Phys. A* 26 (2011), p. 2637.
 2326 doi: [10.1142/S0217751X11053560](https://doi.org/10.1142/S0217751X11053560). arXiv: [1105.1110](https://arxiv.org/abs/1105.1110) [hep-ph].
- 2327 [72] Michael Krämer et al. *Supersymmetry production cross sections in pp collisions
 2328 at $\sqrt{s} = 7 \text{ TeV}$* . 2012. arXiv: [1206.2892](https://arxiv.org/abs/1206.2892) [hep-ph].
- 2329 [73] Rasmus Mackeprang and Andrea Rizzi. “Interactions of Coloured Heavy
 2330 Stable Particles in Matter”. In: *Eur. Phys. J.* C50 (2007), pp. 353–362. doi:
 2331 [10.1140/epjc/s10052-007-0252-4](https://doi.org/10.1140/epjc/s10052-007-0252-4). arXiv: [hep-ph/0612161](https://arxiv.org/abs/hep-ph/0612161)
 2332 [hep-ph].
- 2333 [74] Rasmus Mackeprang and David Milstead. “An Updated Description of
 2334 Heavy-Hadron Interactions in GEANT-4”. In: *Eur. Phys. J.* C66 (2010), pp. 493–
 2335 501. doi: [10.1140/epjc/s10052-010-1262-1](https://doi.org/10.1140/epjc/s10052-010-1262-1). arXiv: [0908.1868](https://arxiv.org/abs/0908.1868)
 2336 [hep-ph].
- 2337 [75] J. Alwall, R. Frederix, S. Frixione, V. Hirschi, F. Maltoni, O. Mattelaer, H. S.
 2338 Shao, T. Stelzer, P. Torrielli, and M. Zaro. “The automated computation of
 2339 tree-level and next-to-leading order differential cross sections, and their
 2340 matching to parton shower simulations”. In: *JHEP* 07 (2014), p. 079. doi:
 2341 [10.1007/JHEP07\(2014\)079](https://doi.org/10.1007/JHEP07(2014)079). arXiv: [1405.0301](https://arxiv.org/abs/1405.0301) [hep-ph].
- 2342 [76] “dE/dx measurement in the ATLAS Pixel Detector and its use for particle
 2343 identification”. In: (2011).

- 2344 [77] ATLAS Collaboration. “The ATLAS Simulation Infrastructure”. In: *Eur.*
2345 *Phys. J.* C70 (2010), pp. 823–874. doi: [10.1140/epjc/s10052-010-1429-9](https://doi.org/10.1140/epjc/s10052-010-1429-9). arXiv: [1005.4568 \[physics.ins-det\]](https://arxiv.org/abs/1005.4568).
- 2347 [78] Alexander L. Read. “Presentation of search results: The CL(s) technique”.
2348 In: *J. Phys.* G28 (2002). [,11(2002)], pp. 2693–2704. doi: [10.1088/0954-3899/28/10/313](https://doi.org/10.1088/0954-3899/28/10/313).
- 2349

2350 DECLARATION

2351 Put your declaration here.

2352 *Berkeley, CA, September 2016*

2353

Bradley Axen

2354

2355 COLOPHON

2356

Not sure that this is necessary.